SPECTRODIRECTIONAL INVESTIGATION OF A GEOMETRIC-OPTICAL CANOPY REFLECTANCE MODEL BY LABORATORY SIMULATION

Adam Christopher Stanford
B.Sc. University of Lethbridge, 2012

A Thesis
Submitted to the School of Graduate Studies
of the University of Lethbridge
in Partial Fulfilment of the
Requirements for the Degree

MASTER OF SCIENCE

Department of Geography
University of Lethbridge
LETHBRIDGE, ALBERTA, CANADA

SPECTRODIRECTIONAL INVESTIGATION OF A GEOMETRIC-OPTICAL CANOPY REFLECTANCE MODEL BY LABORATORY SIMULATION

ADAM STANFORD

Date of Defense: April 28, 2017

Dr. Craig Coburn Co-Supervisor	Associate Professor	Ph.D.
Dr. Derek Peddle Co-Supervisor	Professor	Ph.D.
Dr. Chris Hopkinson Thesis Examination Committee Member	Associate Professor	Ph.D.
Dr. Nadia Rochdi Thesis Examination Committee Member	Adjunct Professor	Ph.D.
Dr. Kevin McGeough Thesis Examination Committee Chair	Professor	Ph.D.

DEDICATION

I dedicate this thesis to my family.

To my parents, Gary and Diane Stanford, whose constant love, support, and encouragement to follow my passion throughout my life has made this all possible. Thank you for believing in me.

To my grandparents, Mike and Margaret Schneyder, for their love and support, and for introducing me to the books which instilled within me an interest in science when I was young.

To my siblings Matthew, Sean, and Megan, and their families.

ABSTRACT

Canopy reflectance models (CRMs) can accurately estimate vegetation canopy biophysical-structural information such as Leaf Area Index (LAI) inexpensively using satellite imagery. The strict physical basis which geometric-optical CRMs employ to mathematically link canopy bidirectional reflectance and structure allows for the tangible replication of a CRM's geometric abstraction of a canopy in the laboratory, enabling robust CRM validation studies. To this end, the ULGS-2 goniometer was used to obtain multiangle, hyperspectral (Spectrodirectional) measurements of a specially-designed tangible physical model forest, developed based upon the Geometric-Optical Mutual Shadowing (GOMS) CRM, at three different canopy cover densities. GOMS forward-modelled reflectance values had high levels of agreement with ULGS-2 measurements, with obtained reflectance RMSE values ranging from 0.03% to 0.1%. Canopy structure modelled via GOMS Multiple-Forward-Mode (MFM) inversion had varying levels of success. The methods developed in this thesis can potentially be extended to more complex CRMs through the implementation of 3D printing.

ACKNOWLEDGEMENTS

I would like to thank my supervisor Dr. Craig Coburn for his constant patience, guidance, and swift assistance with the myriad of technical and logistical details involved in the development of this research, without which this thesis would not have been possible. I would also like to thank my supervisor Dr. Derek Peddle for his mentorship and for encouraging me to pursue graduate studies, as well as for his guidance and support with the modelling component of this research.

I thank my thesis committee member Dr. Nadia Rochdi for her discussions and insight related to my research. I would also like to thank Ray Soffer of the National Research Council (NRC Flight Research Laboratory – Ottawa) for meeting with me and discussing my research during a visit from Ontario, and providing valuable insight into my work. I am grateful for the funding provided to perform this research from the NSERC CREATE Advanced Methods, Education and Training in Hyperspectral Science and Technology (AMETHYST) program, as well as the support from the Alberta Terrestrial Imaging Center (ATIC), and the University of Lethbridge School of Graduate Studies. Also, I acknowledge my thesis committee member, Dr. Chris Hopkinson, who very recently joined the committee.

TABLE OF CONTENTS

LIST OF ACRONYMS

ASD – Analytical Spectral Devices
BOREAS – Boreal Ecosystem-Atmosphere Study
BRDF – Bidirectional Reflectance Distribution Function
BRF – Bidirectional Reflectance Factor
CCD – Charge-Coupled Detector
CHRIS – Compact High Resolution Imaging Spectrometer
CRM – Canopy Reflectance Model
DC – Digital Count
DW –Downwelling
ECV – Essential Climate Variable
EE – Electromagnetic Energy
EMR – Electromagnetic Radiation
EMS – Electromagnetic Spectrum
FBM – Full Blind Mode
FOV – Field of View
FPD – Fast Poisson-Disc
FSF – Field Spectroscopy Facility
FWHM – Full-Width at Half-Maximum
GOMS – Geometric-Optical Mutual Shadowing
HCRF – Hemispherical-Conical Reflectance Factor
IAA – Illumination Azimuth Angle
IZA – Illumination Zenith Angle
LAI – Leaf Area Index
MFM – Multiple-Forward-Mode
MISR – Multi-Angle Imaging Spectroradiometer
MODIS – Moderate resolution Imaging Spectroradiometer
NDVI – Normalized Difference Vegetation Index
NERC – Natural Environment Research Council
NIR – Near-Infrared
NOAA – National Oceanic and Atmospheric Administration
OJP – Old Jack Pine
ORNL DAAC - Oak Ridge National Laboratory Distributed Active Archive Center
PAR– Photosynthetically Available Radiation
PARABOLA - Portable Apparatus for Rapid Acquisitions of Bidirectional Observations of Land and Atmosphere
PP – Perpendicular Plane
RS – Remote Sensing
RTLSR – RossThick LiSparse Reciprocal
SAZ – Solar Azimuth
SNR – Signal to Noise Ratio
SPP – Solar Principal Plane
SSA – Southern Study Area
SZA – Solar Zenith Angle
ULGS-1 – University of Lethbridge Goniometer System 1
ULGS-2 – University of Lethbridge Goniometer System 2
UW – Upwelling

VAA – Viewing Azimuth Angle
VI – Vegetation Index
VIS – Visible
VZA – Viewing Zenith angle

LIST OF EQUATIONS

LIST OF FIGURES

LIST OF TABLES

1 INTRODUCTION

1.1 Background

Global climate change in the form of increasing atmospheric temperatures can have far-reaching economic, societal, and environmental implications; ranging from food shortages caused by an increased incidence of droughts in crucial food-producing regions to the total loss of large cities due to rising ocean levels. Decision-makers, at the governmental level, require sound, science-based information in order to make properly informed decisions in the process of policy development in these matters, as well as to effectively prescribe appropriate action to be taken in response to climate change-related threats (Purkis & Klemas, 2011). A key variable in the current climate change models which drive policy-making is biophysical-structural information about Earth's vegetated land cover. Of particular interest are forests, due to their ability to sequester large amounts of carbon dioxide, which is a primary contributor to increased global atmospheric temperatures (IPCC, 2015).

While biophysical-structural forest data collected using field-based techniques can be useful in understanding the processes involved in climate change at local scales, in order to properly identify and monitor changes to the climate and its effects on the environment at regional or global scales, information derived from remote sensing (RS) data collected at moderate-to-large scales via spaceborne and airborne platforms is a necessity (Franklin & Wulder, 2002; Purkis & Klemas, 2011). In addition to its importance in predictive and prescriptive climate change models, large-scale derivation of forest biophysical-structural data can aid in identifying areas where carbon sink potential is not fully utilized; a primary consideration in climate change mitigation efforts (IPCC,

2015). Current predictive climate change models project an increase in Earth's surface temperature in all emissions-related scenarios, emphasizing the importance of optimizing the efficacy of mitigation factors such as vegetative carbon sinks.

In the four decades since the launch of the first RS Earth observation systems, optical RS has become recognized as an invaluable toolset for providing dependable, high-quality data in many fields of science, largely due to its unique and desirable ability to allow a vast range of Earth surface properties to be studied indirectly and inexpensively through investigation of their spectral features (Mack, 1990). Increased global demand and inexpensive access to RS data has fueled dramatic recent growth in developing RS products aimed at the end-consumer, with the RS industry's value projected to grow at a 9.3% compound annual growth rate from a projected $8.9 billion value in 2016 to a projected $13.8 billion value in 2021 worldwide (Research, 2016).

Satellite and airborne remote sensing systems are routinely used to collect vital data used in a wide number of broad applications; including, but not limited to: climate change modelling and monitoring, increasing agricultural productivity, and forest management (Sellers et al., 1995; Franklin & Wulder, 2002; Thenkabail et al., 2010). The advent of Earth observation systems has greatly aided researchers in understanding the way our planet and its natural processes are changing over time in relation to increasing average global temperatures, notably in the research performed by members of the Intergovernmental Panel on Climate Change (IPCC).

In 2007, a report by the IPCC stated that a scientific consensus had been reached that, with a 90% level of certainty, the warming of the Earth's climate is primarily caused by an increase of anthropogenic greenhouse gases (Christensen et al., 2007). It has been calculated that 78% of the greenhouse gases released into the atmosphere over the past

century are directly caused by the anthropogenic combustion of fossil fuels (IPCC, 2015). This anthropogenically-driven increase in greenhouse gas emissions, and subsequent increase in the atmosphere's heat carrying capacity, is the primary driving cause of the increased frequency and severity of climate-related natural disasters which can be economically and societally crippling (Griggs & Noguer, 2002).

One of the major contributing factors in this increased greenhouse effect is carbon dioxide (IPCC, 2015). The Earth's forests are a vital part in the carbon cycle due to their ability to act as a carbon sink and remove carbon from the atmosphere, which has prompted substantial investigation into the Earth's forest stocks in order to develop models simulating the magnitude and effects of increased average atmospheric temperatures (Birdsey, 1992; Brown, 2002).

The Canadian boreal forest is the most extensive type of land cover and the largest contiguous ecosystem on Earth, covering over 300 million hectares of land within Canadian borders and extending across the country from the Yukon Territory to the coast of Newfoundland (McCullough et al., 1998). The Boreal Ecosystem-Atmosphere Study (BOREAS) was a large-scale research study developed to attempt to better understand the natural processes existing in Canada's boreal forest, including its interaction with Earth's atmosphere (Sellers et al., 1995). The interactions between Canada's boreal forest and the atmosphere have been extensively studied due to efforts such as the BOREAS project, and boreal forests are a significant contribution to global-scale biogeochemical processes that have a direct impact on the effects of climate change in Earth's atmosphere, such as the carbon and nitrogen cycles (Hall, 1999; Peddle et al., 1999; Liang et al., 2000; Brown, 2002; Morison et al., 2014). Canada's forest stocks have been subject to significant disturbances in recent years, notably through the loss of millions of hectares of British

Columbia's mature coniferous forests due to an infestation of the Mountain Pine Beetle (Walton, 2013). As one of Canada's most important economic resources, identification of structural changes in Canadian forests is of primary concern to both the public and private sectors (Sellers et al., 1995).

Remote sensing is widely recognized as the only practical set of technologies currently available for monitoring the inventory and health of Canada's boreal forests at larger than local scales, and is a useful tool for estimating structural forest stand characteristics such as stand density (trees per unit of area) and canopy dimensions such as tree height and crown radii; which in turn can be used to derive important biophysical measures for forest stands such as above-ground biomass and leaf area (Hall, 1999; Patenaude et al., 2005).

These measures are critical for forest carbon estimates, which are extensively used in studies related to climate change (Brown, 2002; Fournier et al., 2003; Peddle et al., 2004). In the context of global policy, remote sensing is considered to be an imperative method for deriving several types of terrestrial "Essential Climate Variables" (ECVs) (UNFCCC, 2004; Patenaude et al., 2005). Accurately deriving and reporting ECVs such as leaf area index (LAI) is a fundamental requirement for countries reporting on global climate change agreements such as the 2005 Kyoto Protocol, under which participating countries have agreed to lower their carbon emission levels based on the premise that anthropogenic atmospheric carbon is, in fact, causing an increase in Earth's temperature (UNFCCC, 2004; Patenaude et al., 2005).

Therefore, it is of vital importance to have a thorough understanding of the structural and biophysical charateristics of Earth's forests in order to properly understand the potential these forests have for carbon sequestration, and in turn their potential to

mitigate the negative effects of climate change. However, the impracticality of measuring these variables directly in ground campaigns has compelled researchers to make attempts to accurately estimate these characteristics using available remote sensing data through the use of a Canopy Reflectance Model (CRM).

Of particular interest in the context of the Canadian boreal forest are geometric-optical CRMs. Geometric-optical CRMs have been designed to, upon a strictly physical basis, create a link between a pixel-level reflectance value and the structure of the forest canopy contained within the pixel's footprint by taking into account the location of the Sun and the sensor in relation to the forest target. This principle of bidirectional dependence of a scene's pixel reflectance upon Sun-sensor geometry provides the mathematical foundation for these geometric-optical models. A prominent example of a CRM of interest to researchers is the Geometric Optical Mutual Shadowing (GOMS) model (Li & Strahler, 1992).

Conceptually, the GOMS canopy reflectance model considers a forest canopy to be a 3-dimensional assemblage of opaque, discrete, simple geometric shapes above a contrasting background in order to model pixel values based upon the physical processes that drive bidirectional reflectance (Strahler & Jupp, 1990). Assessment of the ability of these geometric-optical methods to estimate canopy reflectance and structure through rigorous validation studies is an important task to undertake prior to widespread implementation of the model. Due to the strict physical basis behind GOMS, as well as its sufficiently conceptually simple representation of a canopy, it follows that a physical forest simulation created for the purpose of model validation can be developed which closely mimics the geometric-optical conditions present in this computational model.

Spectrodirectional investigation of the effects of illumination-sensor geometry and its influence on measured hemispherical-conical reflectance factors at varying angles will provide significant insight into possible strengths and shortcomings in the computational methods utilized in the GOMS Model, and can allow for robust validation of many subtle aspects contained within the computational model.

1.2 Research Objectives

Based on the theory that sufficiently simple physically-based CRMs can be physically simulated with tangible materials, the aim of this thesis is to develop techniques to aid in the validation and refinement of CRMs and enhance the characterisation of pixel-level open forest scenes through comparison of BRDF surfaces derived through laboratory measurements of such a simulated forest and modelled reflectance. This includes the following:

- Assess GOMS' ability to simulate reflectance measurements through its use of probabilistic and geometric-optical models by performing statistical comparisons between data produced by the GOMS computational model and produced through spectrodirectional measurements of the physical forest simulation.
- Assess GOMS' ability to estimate forest canopy structure via the use of the Multiple-Forward-Mode inversion technique.
- Assess GOMS' ability to simulate scene-level fractional abundances of scene components
- Assess agreement and fit between BRDF surfaces obtained via various spectrodirectional platforms (ULGS-2, PARABOLA-2) and CRMs (GOMS, RTLSR) for both a laboratory-simulated and *in situ* open forest site.

1.3 Thesis Structure

Chapter 2 – Literature Review begins with a detailed review of spectrodirectional RS, followed by a review of goniometer systems capable of sampling spectrodirectional data for a target. Later in the chapter is an overview of the role modelling plays in remote sensing, followed by a detailed description of the Li & Strahler Geometric Optical Mutual Shadowing (GOMS) model and a contextual overview of the concept of laboratory validation of a model.

Chapter 3 – Methods provides an extensive overview of the equipment and procedures used in this laboratory experiment. A general overview of the design of the laboratory experiment is discussed, including a review of the methods and materials utilized in order to develop the physical model forest simulation. Later, data collection methods and forward-mode BRDF surface and MFM structure inversion processing procedures are discussed. Finally, methods used to obtain BRDF surfaces from MODIS and PARABOLA instruments are discussed.

Chapter 4 – Results provides the results gathered through the use of a laboratory goniometer to assess the implications of the GOMS model's assumptions through the construction of the physical model forest simulation. The results gathered from the derivation of BRDF surfaces from *in situ* PARABOLA data and the MODIS BRDF product are also detailed.

Chapter 5 – Discussion and Conclusions is primarily concerned with the discussion of the implications of the results outlined in Chapter 4, including an overall assessment of the agreement between results obtained from the laboratory simulation and those obtained from the true boreal open forest location. Future work and improvements that can be used

to build on the knowledge provided by the investigations in this thesis are also considered.

2 LITERATURE REVIEW

2.1 Remote Sensing of Vegetation

Remote sensing (RS) systems allow Earth science researchers attain otherwise unavailable information about the processes related to vegetation canopies at various scales through their ability to perform indirect measurement of electromagnetic radiation (EMR) propagated through processes driven by a canopy surface (Grum & Becherer, 1979; Suits, 1983; Jensen, 2009; Prasad et al., 2011). Optical RS systems utilize a technique known as radiometry to measure the intensity of optical EMR interacting with the system's sensor throughout the optical region of the electromagnetic spectrum, the wavelength range of which extends from ultraviolet (250nm) to short-wave infrared (2500nm) (Jensen, 2009; Palmer & Grant, 2010).

The flow rate of EMR energy passing or interacting with a given area over a specific amount of time is termed radiant flux (Nicodemus et al., 1977). Radiant flux (Φ) is measured in watts, and is defined as:

$$\Phi = \frac{dQ}{dt}\,[J/s] \tag{2.1}$$

where dQ refers to the radiant energy provided by the energy source in Joules at a particular location, and dt is the time over which the radiant energy passed the location (Elachi & Van Zyl, 2006). The energy flow of incoming radiant flux upon a target of

interest, known as irradiance (E), is driven by the intensity of the incoming radiant flux and the spatial area of the target and is defined as

$$E = \frac{\Phi}{A} \ [W \ m^{-2}], \tag{2.2}$$

where d is the radiant flux and A is the area of the target (Nicodemus et al., 1977; Elachi & Van Zyl, 2006). As EMR emitted from a source interacts with a surface, the properties of the material dictate its response to the incoming energy. Whether the energy is absorbed, transmitted or reflected is a fundamental property of the material and its physical state. This pattern of energy interaction for all wavelengths in the EMS is known as the material's spectral properties (Suits, 1983).

The spectral properties of vegetation are influenced by the biochemical makeup of the plant material and the properties of the incoming EMR (Suits, 1983). This connection between vegetative spectral properties and emitted radiant flux facilitates the use of remote sensing for differentiation between vegetation and other surface types, as well as differentiation between different vegetation types based on the identification of biochemical characteristics of the plant or canopy being measured (Asner, 1998). However, because the properties of EMR emitted from the Sun vary depending on time and the location of observations, the concept of spectral reflectance was developed to allow for comparison of optical measurements of surfaces independent of incident illumination (Robinson & Biehl, 1979; Kumar et al., 2001; Peddle et al., 2001a). In its most basic form, reflectance (ρ) can be represented as:

$$\rho = \frac{L}{E} [W \ m^{-2}] \tag{2.3}$$

Where L is the radiant flux reflected by the target (termed radiance) and E is the total incident radiant flux (termed irradiance) (Grum & Becherer, 1979; Schott & Schott,

2009). In terms of remotely sensed data collected via field or laboratory campaign, calculation of spectral reflectance as a function of wavelength (λ) is defined as:

$$p(\lambda) = \frac{\phi\lambda L}{\phi\lambda E} \tag{2.4}$$

Where $\phi\lambda L$ is the radiance reflected from a target surface and $\phi\lambda E$ is the radiance reflected from a Lambertian surface (Grum & Becherer, 1979; Peddle et al., 2001a).

In terms of spectral resolution, there are two broad categories of Earth Observation (EO) spaceborne and airborne optical sensor systems currently in deployment: multispectral broadband sensors and hyperspectral narrowband sensors. The oldest and historically the most widely utilized category is multispectral sensors. Broadband sensors collect data in a small number (typically less than 15) of spectral bands, each spanning a wide spectral range (typically 100 nm) (Kumar et al., 2001). The intensity of the signal collected in each band is a function of the sensor's optical system, as well as the characteristics of the bandpass filter applied to a given sensor element, characterized by the bandpass filter's full width at half maximum (FWHM) value.(Kumar et al., 2001; Kavzoglu, 2004).

Hyperspectral RS systems are differentiated from multispectral RS systems by their designed ability to collect of data over a large number of contiguous bands over a small wavelength range. For example, the Airborne Visible/Infrared Imaging Spectrometer (AVIRIS) system collects data over 224 contagious spectral bands with a nominal resolution of 10 nm FWHM, whereas Landsat 8's OLI sensor collects data in nine discrete bands; each with a much more coarse spectral resolution compared to AVIRIS bands (Green et al., 1991; Roy et al., 2014). This increase in the spectral resolution of hyperspectral RS data over broadband data directly translates into an

increase in the amount of information provided by this data in comparison to that of multispectral RS (Kumar et al., 2001). The highly detailed spectral information provided by imaging spectroscopy allows for diagnostic investigation of the molecular properties of materials (Grum & Becherer, 1979). A spectral signature corresponding to healthy, green conifer needles is shown in Figure 2.1, and was derived using data provided by the ASTER spectral library 2 (Baldridge et al., 2009). This spectra was collected at a nadir view angle, and therefore does not indicate the spectral variability expected from a natural target surface when viewed at an off-nadir view angle.

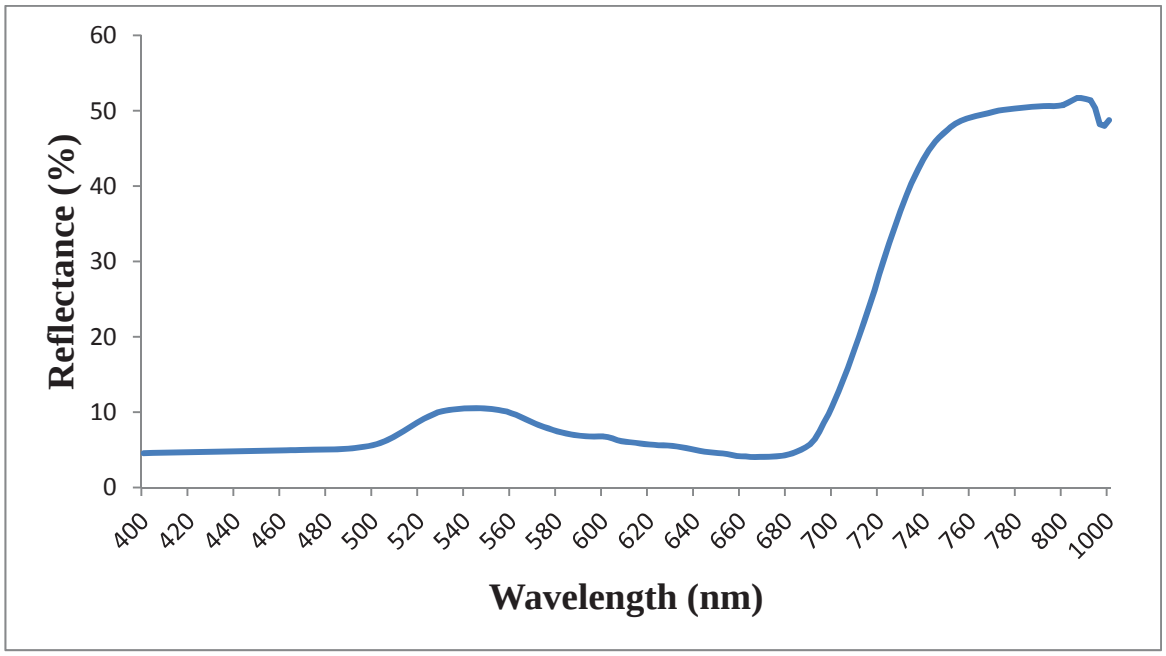

Figure 2.1: Spectral reflectance profile of healthy, green conifer needles sampled at a nadir look angle. Data source: ASTER spectral library 2 (Baldridge et al., 2009).

The reflectance features of green, healthy vegetation are primarily influenced by the healthy vegetation's biochemical components (Asner, 1998). General reflectance patterns are consistent in healthy green vegetation regardless of species due to their dependence upon common vegetative characteristics and compounds, such as cellular structure and leaf pigments (Vane & Goetz, 1993; Pu & Gong, 2011). For example,

characteristic low reflectance levels in the visible region of the EMS (400 nm – 700 nm) are caused by high levels of absorption by foliar pigments, primarily chlorophyll, carotene, and xanthophyll (Myneni et al., 1989).

A characteristic sharp increase in the reflectance curve at the 690 nm – 720 nm region in healthy vegetation spectra is referred to as the reflectance red edge (RRE). The spectral reflectance features of the RRE of healthy vegetation have been extensively studied, and have been found to be highly correlated with vegetative chlorophyll content, water content, and internal leaf structure. Therefore, the RRE is sensitive to changes in important derived quantities such as leaf area index (LAI), which allows for it to be used as a powerful diagnostic tool in ecological studies (Asner, 1998). Because the reflectance properties of healthy green vegetation are linked to the biochemical compounds in the leaf structure, it follows that changes in the abundance of these compounds due to plant senescence or environmental disturbances will cause a representative change in the vegetation's spectral reflectance features (Pu & Gong, 2011). Identification of this link between reflectance and vegetation's chemical makeup and water content has facilitated the development of many empirical models which are useful in crucial ecological studies such as the identification of vegetation disturbances (Kumar et al., 2001).

2.2 Multi-Angular Remote Sensing

Nadir-looking remote sensing instruments are useful for identifying and monitoring certain vegetation characteristics; however, multi-angular remote sensing better facilitates the accurate retrieval of important biophysical-structural variables (BSVs), including ones considered to be ECVs, such as fraction of absorbed photosynthetically active radiation (FAPAR) and Leaf Area Index (LAI) (Asner, 1998).

The primary reason for this increased ability to accurately quantify BSVs is based upon the inherent link between canopy reflectance anisotropy and the physical structure of the canopy (Li & Strahler, 1986; Asner et al., 1998). The anisotropic behavior of reflectance is also highly dependent on illumination and sensor geometry; therefore, data collected at multiple angles contains a higher level of biophysical information which cannot be derived using nadir-looking data alone (Li & Strahler, 1986; Asner et al., 1998). This Sun-sensor geometry dependent phenomenon is termed bidirectional reflectance. The distribution of a target's bidirectional reflectance in relation to the illumination geometry, when taken into account at all possible angles, is referred to as the Bidirectional Reflectance Distribution Function (BRDF) (Nicodemus, 1965).

2.3 Bidirectional Reflectance Distribution Function (BRDF)

The BRDF is defined by equation 2.5:

$$\rho BRDF = \frac{L(\theta_v, \phi_{v,}\lambda)}{E(\theta_i \phi_i \lambda)} [sr^{-1}] \tag{2.5}$$

where L is the radiance that is reflected from a specific land cover at infinitesimally small zenith (θ_v) and azimuth (ϕ_v) angles, and E refers to the amount of incoming radiation at infinitesimally small zenith (θ_i) and azimuth (ϕ_i) angles (Nicodemus et al., 1977). Both the incoming irradiance and reflected radiance are a function of the wavelength being sampled (λ). Single measurements of bidirectional reflectance, referred to as bidirectional reflectance factors (BRFs), are defined as the ratio of exitance to irradiance, scattered over an infinitesimally small angle (Nicodemus et al., 1977; Sandmeier, 2000; Schaepman-Strub et al., 2006). A diagram outlining the BRDF concept can be seen in Figure 2.2.

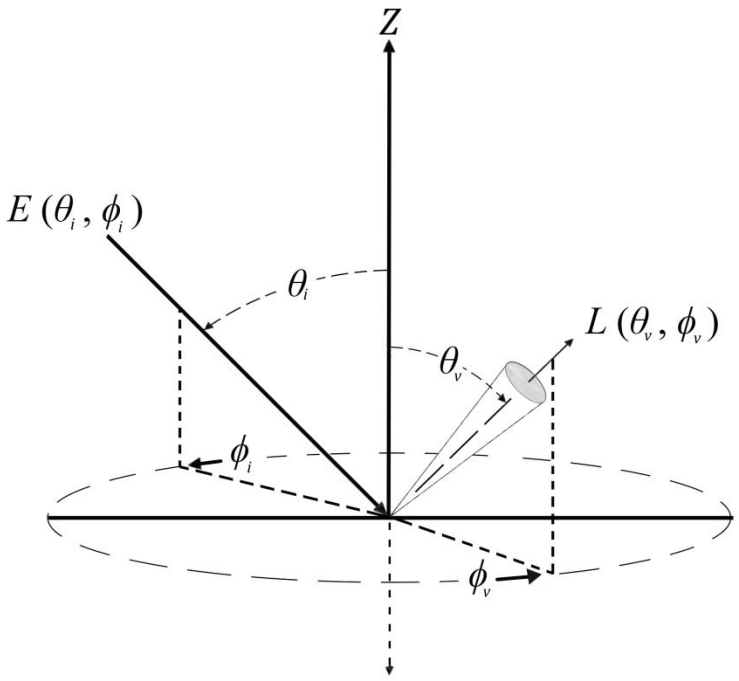

Figure 2.2 : Bidirectional reflectance concept. Ratio of upwelling radiance (L) scattered over a solid angle (θ_v, ϕ_v) to downwelling irradiance (E) incoming from direction (θ_i, ϕ_i)

Understanding of the effects of the BRDF based on Sun-sensor geometry in relation to surface targets is important for proper interpretation of all remotely sensed data, including that collected onboard airborne and satellite remote sensing platforms, due to the inherent bidirectional nature of all reflectance data (Koechler et al., 1994). This process of collecting spectral data for a single target at multiple angles is referred to as spectrodirectional RS (Schaepman, 2007). There are currently several satellite and airborne-based systems able to collect multi-angular data, such as the Multi-angle Imaging Spectroradiometer (MISR), the Moderate Resolution Imaging Spectroradiometer (MODIS), the Compact High Resolution Imaging Spectrometer (CHRIS), among others (Strahler & Jupp, 1990; Martonchik et al., 1998; Sugianto & Laffan, 2004). The first systems capable of collecting data at multiple view angles were originally designed with

the intention of reducing satellite revisit time at a given location, but noticeable differences in the reflectance signatures collected by the sensor systems at differing view angles led to the introduction of research into the anisotropic nature of natural surfaces found on Earth, and subsequently into the effects of the BRDF (Coburn & Noble, 2009).

While the BRDF is the most widely used term to refer to the anisotropic reflectance properties of a surface, it is considered to be a conceptual quantity that can never be directly measured due to the fact that it is a function consisting of infinitesimally small view and illumination angles (Nicodemus et al., 1977). The BRDF is one of several conceptual quantities that cannot be measured (Schaepman-Strub et al., 2006). Measurements of bidirectional reflectance are, in reality, measuring a target illuminated by incident radiation incoming from a hemispherical source due to photon interaction with the atmosphere. The upwelling radiation reflected from the target and detected by the sensor is scattered over a solid angle; these two quantities define a case which is referred to as "hemispherical-conical" reflectance, the concept of which has been visualized in Figure 2.3 (Schaepman-Strub et al., 2006). Milton, Schaepman, and Anderson (2009) have stated that, although there are multiple theoretically measurable reflectance quantities, all spectroscopic measurements in a strict physical sense should be categorized in the hemispherical-conical case due to the inherent hemispherical nature of incident irradiance and conical nature of upwelling radiance as it disperses over a solid angle.

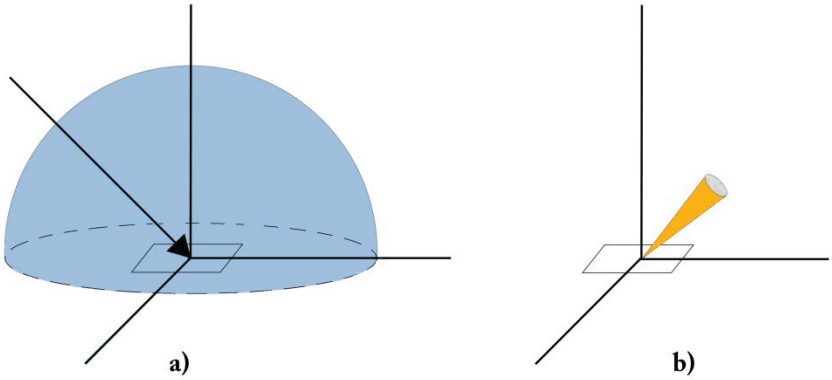

Figure 2.3: Visual representations of the hemispherical-conical quantities of bidirectional reflectance, the case within which all true spectral measurements are collected. In a), it can be seen that there is both a directional and a hemispherical component involved in the irradiance incident upon a target. In b), it can be seen that the upwelling radiance reflected from a target is spread over a solid angle.

The BRDF of an open forest canopy has a number of characteristic features which are driven by the nature of the interaction of illumination incident on the scene and the sensor. The feature with the most influence on the shape of the BRDF of an open canopy is a location of reflectance maxima in the backscatter direction known as the hot spot (Kuusk, 1991). The hot spot phenomenon has been observed and understood for many years, and was first identified in aerial remote sensing photography in the form of a bright region surrounding the aircraft's shadow when imagery was collected with the Sun directly behind the aircraft (Suits, 1973, 1983). This dramatic increase in the backscatter brightness of an open vegetative canopy is primarily caused by a mechanism known as shadow-hiding, wherein individual forest components tend to visually obscure their own shadows as the angle at which observations take place approach the location of illumination (Kuusk, 1991; Hapke et al., 1996).

Realistically, in spectrodirectional RS data collection campaigns, HCRF measurements taken directly at the location of the hot spot are not possible due to the

influence of shadows cast by the sensor system upon the target. However, provided that measurements are sampled with a sufficiently high angular sampling resolution, the effects of the hot spot can be studied using measurements collected near the source of illumination (Coburn & Noble, 2016). Another characteristic feature of the BRDF of open canopies exists opposite the location of the hotspot in the solar principle plane (SPP) in the forward scatter direction. This feature is known as the dark spot or dark area, a location at which measured reflectance values reach a minimum (Lacaze et al., 2002). A geometrically-based rationale of the reflectance minima at the dark spot in the case of an open canopy is due to the largest proportion of shadows being viewed in this direction; however, other contributing causes of the dark spot in vegetation canopies have also been identified, such as the backshadow and gap effects (Kimes, 1983; Lacaze et al., 2002). Backshadow effects refer to an increase in the amount of viewed shadow when the view angle is opposite the solar angle, and gap effects refer to a decreased amount of viewed shadow at high viewing zenith angles.

In order for robust and high-quality BRDF modelling of an open canopy to be achieved, both the hot spot and the dark spot must be accounted for in model development. Figure 2.4 features a schematic illustration of the concept of the hot spot and dark spot in terms of a BRDF surface. The displayed reflectance curve corresponds to the Solar Principal Plane (SPP), which refers to the plane which aligns directly with the illumination source. The half of the principal plane located is on the same side of nadir as the Sun is referred to as the Solar Principal Plane (SPP). The plane which runs perpendicular to the SPP is known as the Perpendicular Plane (PP), and crosses the SPP at the nadir location.

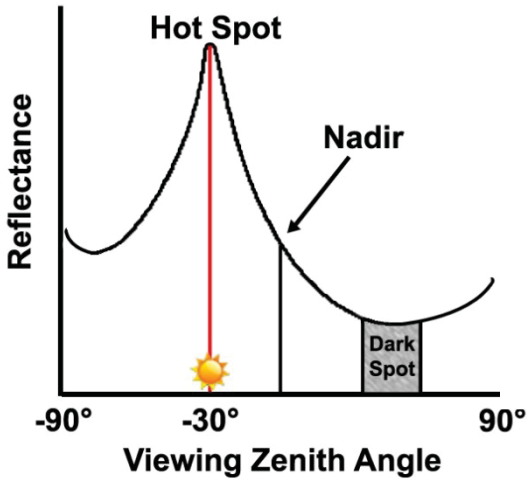

Figure 2.4: Effect of viewing zenith angle upon reflectance in the Solar Principal Plane illuminated at a 30° zenith angle. The hot spot is centered at the illumination zenith angle. The backscatter direction corresponds to the area between -90° and nadir, and the forward-scatter direction corresponds to the area between 90° and nadir. (Adapted from Lacaze, 2002)

2.4 Laboratory HCRF Sampling

The impossibility of directly measuring the BRDF directly has led to the development of methods allowing for sampling HCRF values at varying viewing zenith and azimuth angles. This multi-angular remote sensing data collected under controlled laboratory settings has been an important factor in helping researchers to understand the effects of the BRDF on different surface types (Hosgood et al., 2000; Sandmeier & Strahler, 2000). Some advantages of laboratory BRDF experiments over those performed in the field were outlined by Sandmeier & Strahler (2000). Advantages of laboratory-based experiments include the fact that there is a negligible amount of atmospheric influence on illumination conditions between the illumination source, target, and sensor; as well as the elimination of unwanted environmental conditions such as wind, and the ability to utilize an illumination source whose location remains stable regardless of the time elapsed during data collection.

However, measurement of HCRF in the laboratory suffers from numerous disadvantages as well. While acquisition of a high signal-to-noise ratio in ideal outdoor illumination conditions is not an issue, an illumination source used in a laboratory setting must be suitably intense to achieve a high SNR. Further, simulating the hemispherical component of outdoor lighting using a secondary, indirect lamp is a requirement in laboratory areas which are not completely black in order to mute the directionality of light reflected from objects in the laboratory upon the target surface. Additionally, the inherent inability to collect measurements of natural surfaces *in situ* and *in vivo* may also be considered a disadvantage of laboratory-based HCRF sampling (Hosgood et al., 2000).

It is useful to describe HCRF reflectance values in the form of anisotropy factors (ANIF) in order to allow for comparison between surfaces (Sandmeier & Deering, 1999; Sandmeier, 2000; Schaepman-Strub et al., 2006). Calculation of the ANIF allows researchers to study the directional distribution of the light reflected from a surface by showing its magnitude in relation to the reflectance viewed at nadir, and is accomplished through the normalization of HCRF values to nadir reflectance:

$$ANIF(\lambda, \theta_i, \phi_i, \theta_v, \phi_v) = \frac{R(\lambda,\theta_i,\phi_i,\theta_v,\phi_v)}{R_v(\lambda,\theta_i,\phi_i)}. \tag{2.6}$$

A similar, but subtly different technique of data normalization which allows for visual investigation and comparison of differences in the BRDF when utilized with data visualization normalizes the measured HCRF values as *percent* differences, as

$$D_{norm} = \frac{\rho(\theta_v \Phi_v) - \rho_{nadir}}{\rho_{nadir}} \times 100\% \tag{2.7}$$

Where D_{norm} is the normalized percent difference, $\rho(\theta_v \Phi_v)$ is the HCRF value at viewing zenith angle (VZA) θ_v and viewing azimuth angle (VAA) Φ_v, and ρ_{nadir} is the HCRF value at nadir.

In order to accurately collect these highly valuable scientific measurements for investigation into the effects and implications of the BRDF, highly specialized remote sensing instruments, known as goniometers, have been developed to accomplish this task.

2.5 Spectrogoniometer Remote Sensing Systems

With the advent of multi-angular remotely sensed data available via spaceborne and airborne platforms, scientific interest in sampling HCRF values for known targets in a controlled laboratory setting has increased significantly (Asner et al., 1998; Jensen, 2007). This has led to the development of instruments capable of sampling HCRF measurements in a controlled manner, referred to as laboratory or field goniometers. There have been numerous studies in the past two decades wherein laboratory goniometer systems were utilized to explore the BRDF effects of the different components found in forested areas, such as soils, mosses, grasses, and the forest canopies themselves (Gibbs et al., 1993; Liang et al., 2000).

Goniometry refers to the science of measuring angles. The instruments used to perform this task are known as goniometers. Goniometers are one of the oldest extant scientific measurement instruments, and have been in use since the time of the ancient Greeks in the form of navigational tools which employ angular measurements; such tools include astrolabes, sextants, octants, quadrants (Hosgood et al., 2000). Modern goniometers utilized in the field of remote sensing are not used to collect angular measurements directly, but rather are designed to position the foreoptics of a remote sensing system such as a spectrometer at precise azimuth and zenith angles in a hemisphere (Coburn & Peddle, 2006; Buchhorn et al., 2013). The target-sensor geometry in remote sensing data collection campaigns utilizing goniometers of the variety utilized

in this study is such that the target remains at a fixed location while the sensor is moved to different angular positions; with the sensor FOV remaining focused at a precise location directly at the center of the base plane of the goniometer's hemisphere (Hosgood et al., 2000; Coburn & Peddle, 2006). This location is referred to as the goniometer's focal point.

2.5.1 Overview of Selected Goniometer Systems

An example of a remote sensing goniometer system designed specifically for use as a laboratory goniometer is the European Goniometric Facility (EGO). The EGO is a specialized laboratory goniometer system located at the Institute for Remote Sensing Applications of the Joint Research Centre in Ispra, Italy (Koechler et al., 1994). The facility has been specifically designed to reduce light scattering though the use of a goniometer system that is painted black, as well as a completely black laboratory area featuring a specialized light-absorbing rubber material covering the floor (Hosgood et al., 2000). The goniometer design, as seen in Figure 2.5, includes two vertical arches supporting computer-controlled motorized sleds, one of which is used to house the illumination source while the other houses the detector.

The two goniometer arches EGO utilizes, each mounted on computer-controlled motorized platforms on separate horizontal circular rails, allow for the independent positioning of the illumination source and detector anywhere on a hemisphere with a 2m radius focused on the target in order to sample BRDF data. The precision stepper motors used to control the movement of the illumination source and sensor in the azimuth and zenith directions allow for movement at a resolution of 0.01^{o}. An advantage of the EGO is its ability to utilize a variety of sensor systems, including the Geophysical

Environmental Research Inc. IRIS, Spectron Engineering SE590, and ASD FieldSpec-FR Spectroradiometer systems. The EGO is extremely versatile in its utility, and experiments are planned to use the goniometer in natural light conditions in order to advance the system's potential (Hosgood et al., 2000).

Figure 2.5: The EGO Goniometer (Hosgood, 1999)

The University of Lethbridge has been involved in the development of state-of-the-art remote sensing goniometer systems since the mid-2000s. The first goniometer developed was the University of Lethbridge Goniometer System (ULGS-1) (Coburn & Peddle, 2006). The ULGS-1 was developed to meet the need for a robust, low-cost goniometer system capable of sampling BRF measurements in various laboratory and field situations. In order to minimize the cost and maximize the simplicity and portability of the goniometer, all movement of the goniometer is performed directly by the operator rather than relying on a computer controlled mechanical positioning system.

The design of the goniometer consists of a sensor sled mounted on a single vertical zenith arch, which rides in a track on a horizontal azimuth ring. The zenith arch

and azimuth ring have marks at 10^{o} increments in which the sled and arch can be positioned in order to ensure consistency in the positional accuracy of repeated measurements. The goniometer design also includes optional extendable legs in order to collect measurements on sloped surfaces and for tall plant canopies. The ULGS-1 goniometer is effective in both laboratory and field bidirectional reflectance studies (Coburn & Peddle, 2006; Coburn et al., 2010).

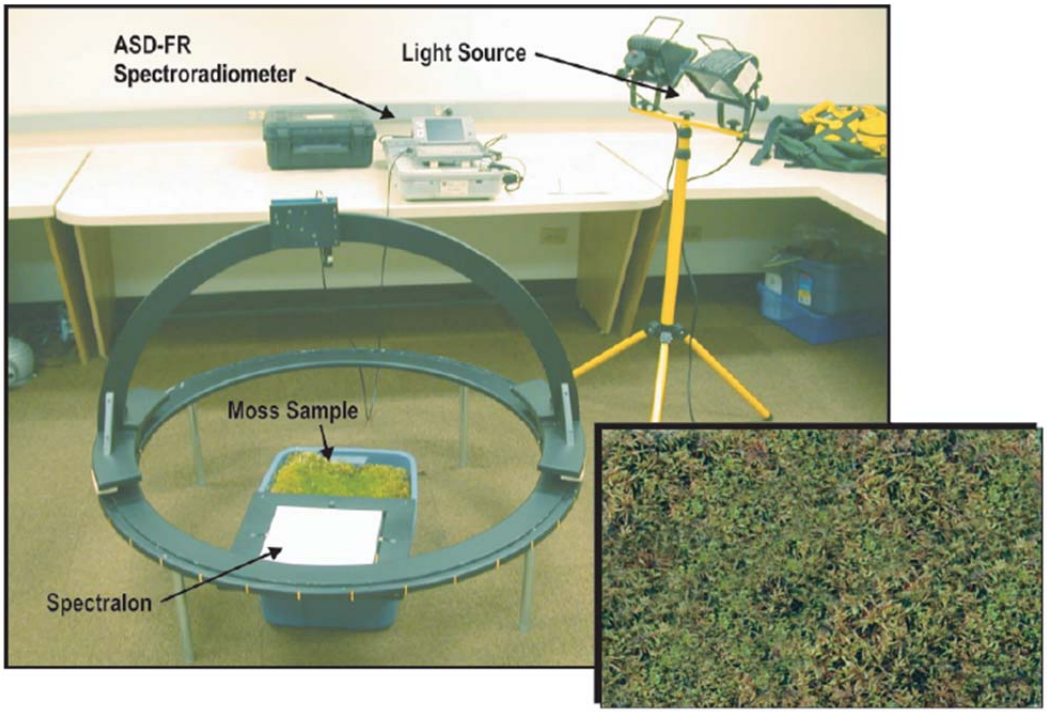

Figure 2.6: The ULGS-1 goniometer in a laboratory setting (Coburn & Peddle, 2006)

2.5.1.1 University of Lethbridge Goniometer System-2 (ULGS-2)

The second generation of ULGS instrument, the ULGS-2, was developed at the University of Lethbridge by Coburn and Noble (2016). The ULGS-2 system was developed with the intention of addressing several common design flaws present in existing goniometer systems, focusing on the existing weaknesses in flexibility allowing for both laboratory-based and field-based measurements, such as weight and portability. The ULGS-2 substantially differs from previous goniometer systems in its incorporation

of a portable base structure supporting a quarter circle positioning arc upon which the sensor sled rests. This quarter arc design eliminates the common circular base structure included in most existing fixed position goniometers, such as that at the EGO, reducing the damage caused to the area surrounding the target if the system is utilized *in situ*. The quarter arc design also reduces the weight of the instrument in relation to previous goniometer systems with a large arc (2m radius) to 150kg through its removal of half of the 180° arc. A graphical representation of the concept behind the ULGS-2's operation can be seen in Figure 2.7.

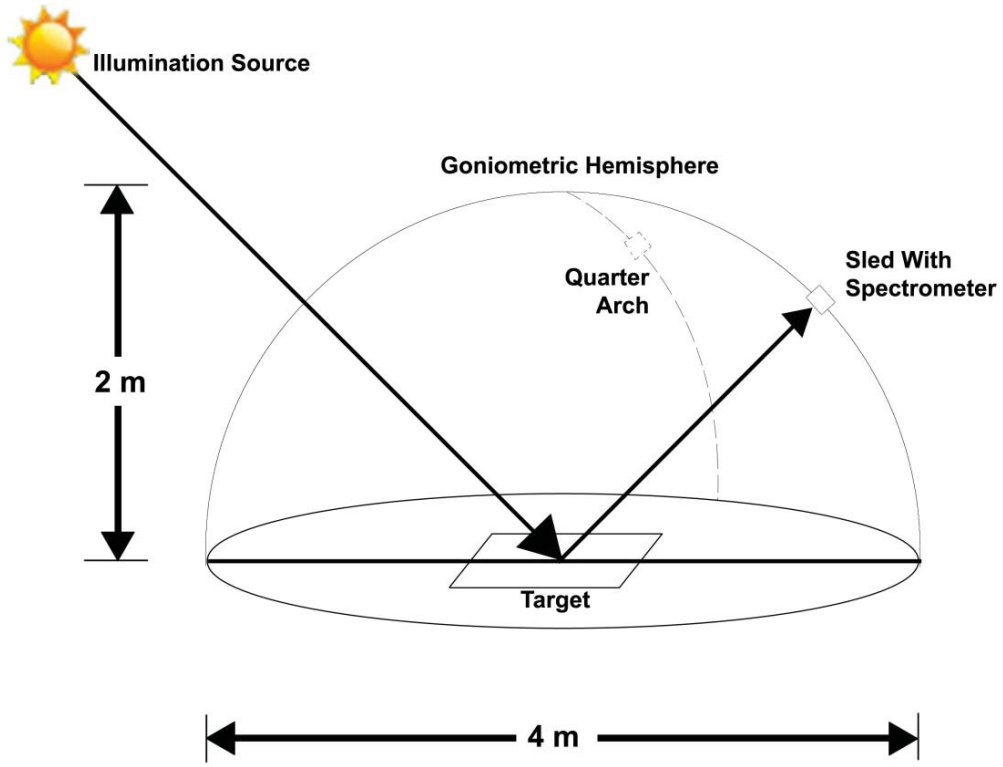

Figure 2.7: Conceptual representation of a goniometer with a 2m quarter-arc design. Target surface is centered on the base plane of the goniometric hemisphere. (Adapted from Sandmeier & Itten, 1999)

The goniometer has been designed to allow for adjustment of the height of the arc in order to facilitate its positioning above targets up to 2m in height (Coburn & Noble, 2016). Azimuthal movement of the ULGS-2's quarter arc is driven by a computer-

operated stepper motor coupled with a 1:100 gear reduction gearbox, and movement of the sensor sled in the zenith direction is driven by a computer-controlled stepper motor. This configuration reduces the probability of operator error and allows for positioning of the sensor within very close tolerances (Coburn & Noble, 2016).

Other advancements over existing goniometer systems include adjustable feet on the support structure, allowing for measurements to be collected on uneven surfaces; as well as the inclusion of a downwelling spectrometer equipped with a cosine-corrected head which can be utilized to derive real-time reflectance measurements in outdoor light conditions for data collected with the upwelling spectrometer mounted upon the sensor sled (Coburn & Noble, 2016). A diagram illustrating the ULGS-2 goniometer setup can be found in Figure 2.8. Figure 2.9 shows the ULGS-2 goniometer itself deployed in the Remote Sensing Laboratory at the University of Lethbridge. It should be noted that in laboratory situations, the downwelling spectrometer is not utilized, and reflectance is derived using a near-Lambertian surface, such as a Spectralon™ polytetrafluoroethylene (PTFE) calibration panel.

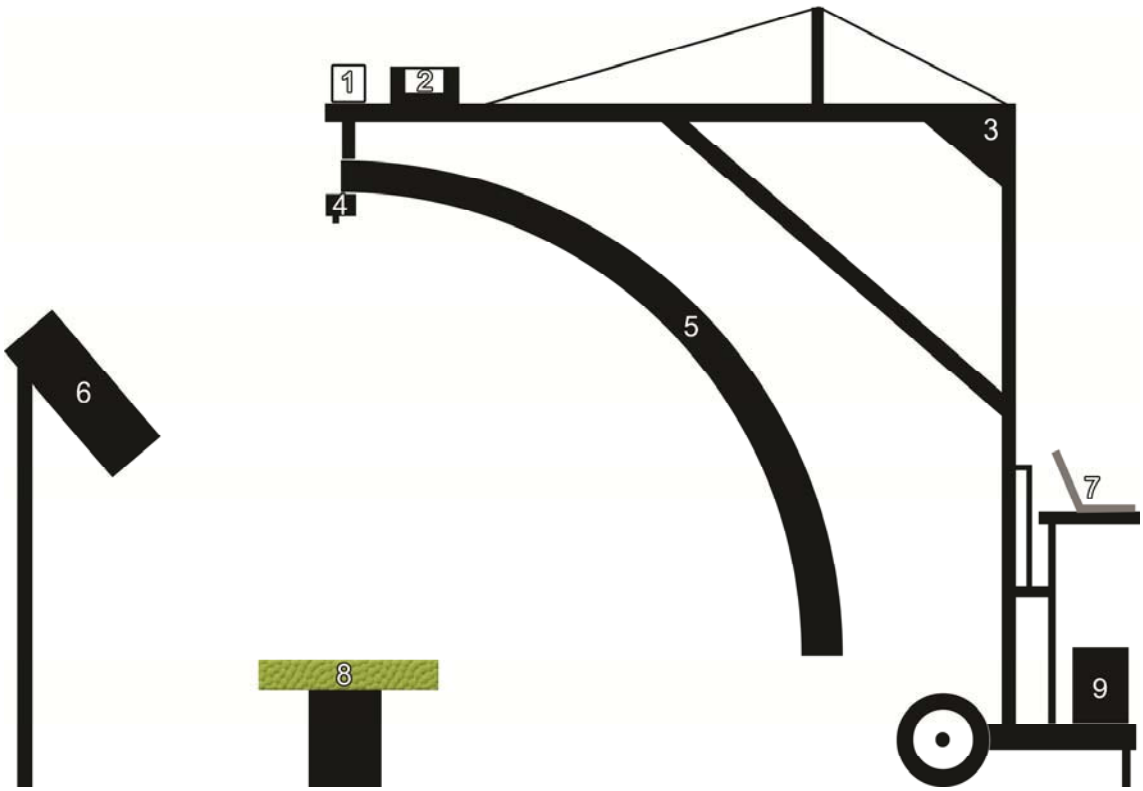

Figure 2.8: University Lethbridge Remote Sensing Laboratory schematic. (1) Azimuth motor (2) Downwelling spectrometer and power distribution system (3) Goniometer support structure (4) Sensor sled with upwelling spectrometer (5) 2m radius quarter arc (6) Altman Shakespeare™ ellipsoidal reflector spotlight (7) Control computer (8) Target panel centered at nadir (9) Battery and inverter.

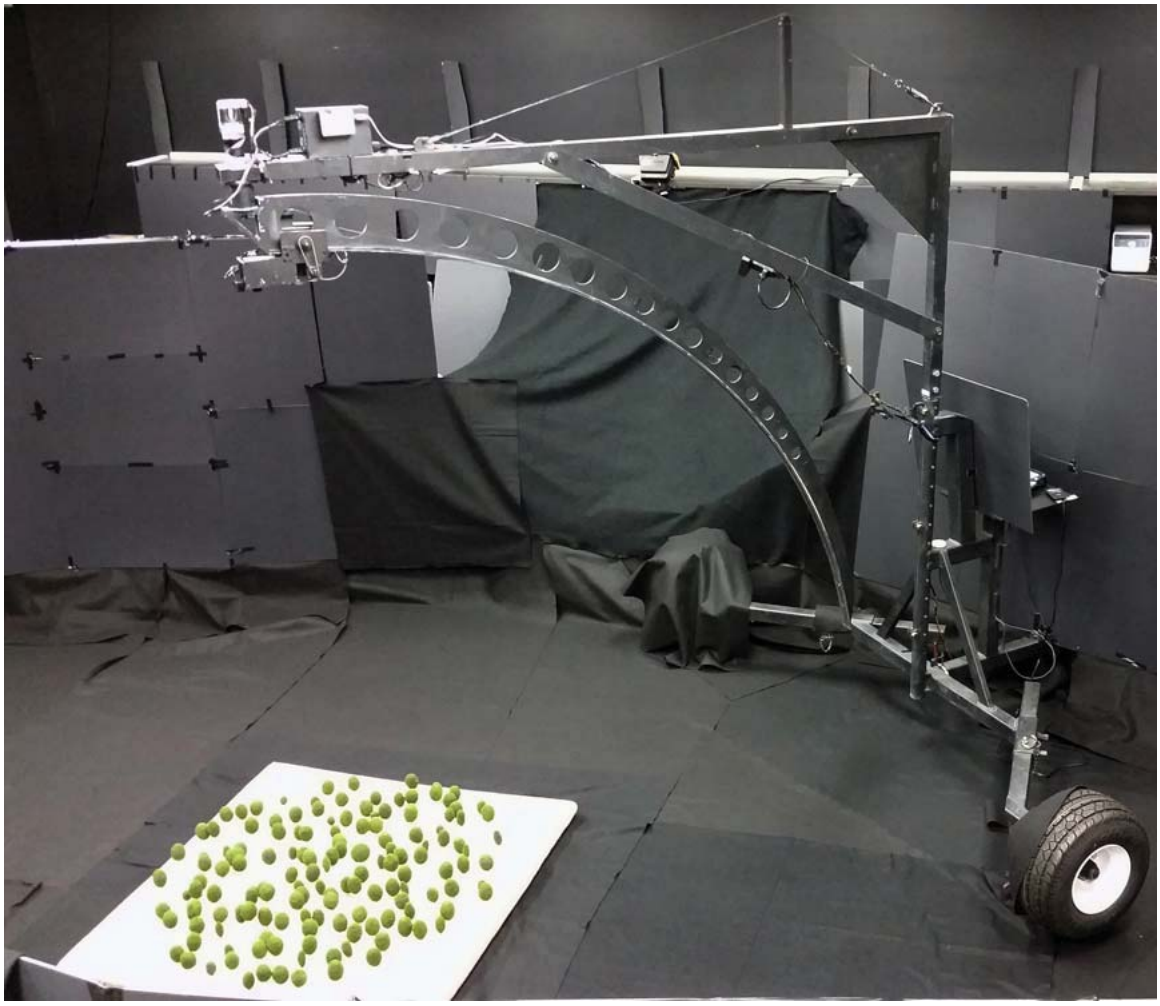

Figure 2.9: University of Lethbridge Remote Sensing Laboratory area and ULGS-2 goniometer system. Light-absorbing materials have been placed in the area surrounding the goniometer system and target.

An important feature of the goniometer system which facilitates the collection of data collection over a short period of time is its ability to utilize an Ocean Optics USB-4000 spectrometer (Coburn & Noble, 2016). The USB-4000 has several advantages over sensor systems utilized in previous goniometers. A first major advantage of the USB-4000 is the extremely lightweight nature of the spectrometer, which was crucial to the design of the ULGS-2 and the ability of the system's sensor sled to move quickly and efficiently. A second major advantage is the USB-4000's adjustable sensor integration time. The integration time of the system can be set for fast data acquisition in the field (up

to 10 spectral samples in under 0.5s) under natural sunlight conditions, facilitating data collection with minimal solar movement; this capability is further enhanced by the ability to capture direct reflectance values in real-time with the pairing of the downwelling and upwelling spectrometers. Due to the spectrometer's ability to collect data at such a rapid rate of speed, the total time required for sampling HCRF values over an entire hemisphere is primarily limited by the speed of the movement of the mechanical systems driving movement in the azimuth and zenith directions. A schematic of the USB-4000 spectrometer can be seen in Figure 2.10.

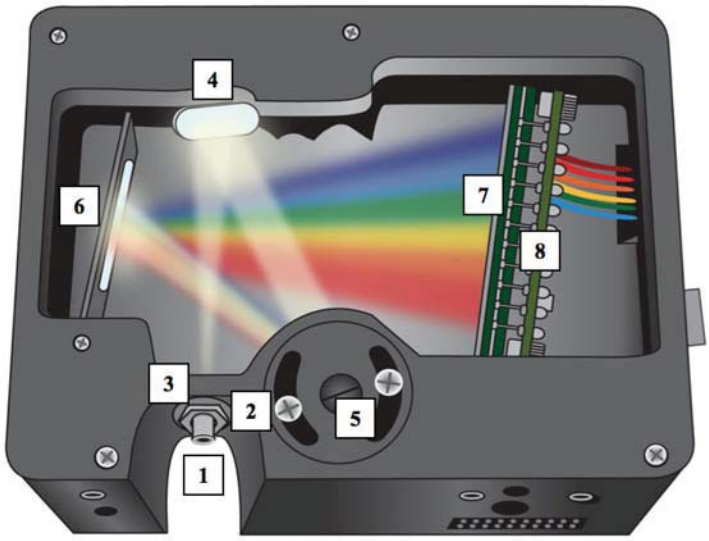

Figure 2.10: Ocean Optics USB4000 Spectrometer. Light enters the optical bench via a fiber optic cable connected to SMA 905 connector (1). An adjustable rectangular aperture directly behind the SMA connector (2) regulates the amount of radiation entering the optical bench. A filter directly behind the aperture (3) restricts incoming radiation to a predetermined range of wavelengths. The radiation is then focused onto a diffraction grating (5) using a collimating mirror (4). The grating diffracts the incoming light into a focusing mirror (6) which reflects the scattered light onto an L4 detector collection lens (7) which focuses the light onto a detector (8). The detector then converts the analog optical signal to a digital signal (Ocean Optics, 2008)

While these advantages are crucial for successful collection of high-quality HCRF data in field studies under outdoor light conditions, the stationary nature of illumination conditions in a laboratory setting reduce the importance of the requirement to collect data

in as short a time span as possible. Conversely, in fact, higher sensor integration times are often desirable in laboratory HCRF sampling campaigns, as they allow for a higher signal-to-noise ratio to be obtained.

The upwelling USB-4000 spectrometer has an aperture which is able to be combined with a variety of foreoptics and barrels that can be used to constrain the sensor's FOV (e.g. 1°, 5°, 8°, 10°, 18°; or 25°) and control the width of the area detected by the sensor at a given height above a target (Coburn & Noble, 2016). The size and shape of the field of view (FOV) of a sensor in a remote sensing goniometer system is a function of the geometry of the sensor's optics, namely the angular location of the optics in relation to surface normal of the target being sensed, and the size of the arc used for controlling the motion of the sensor. Specifications of the USB-4000 spectrometer can be found in Table 2.1.

Table 2.1: Ocean Optics USB-4000 spectrometer technical specifications(Ocean Optics, 2008)

Parameter	Specification
Detector Type	Toshiba TCD1304AP Linear CCD Array
Dark Noise Resolution	50 counts RMS (FWHM)
Pixels (CCD detector elements)	3648
Spectral Range	200 - 1100 nm
SNR	300:1 (at full signal)
Focal length (input)	42mm
Focal length (output)	68mm
Sensitivity at 400nm	130 photons/count
Sensitivity at 600nm	60 photons/count
Integration time range	3.8ms to 10s

2.5.1.2 PARABOLA Goniometer Systems

The Portable Apparatus for Rapid Acquisition of Bidirectional Observation of the Land and Atmosphere (PARABOLA) series of goniometer systems differ from the

previously discussed goniometer systems in both design and measurement capabilities. While the aforementioned goniometer systems measure a single target at a fixed focal point, the PARABOLA-1, PARABOLA-2, and PARABOLA-3 goniometers feature a rotating-head radiometer, the design of which samples multiangular observations in the area surrounding the system in a helical pattern (Deering & Leone, 1986; Bruegge et al., 2000). The system can be mounted for data collection upon a moving vehicle, as in Figure 2.11, or upon any properly equipped moving platform. This design allows it to be useful in collecting multiangle reflectance measurements for the entire hemisphere over a target, provided the target is homogenous in nature. This configuration makes it ideal for collecting multiangle reflectance data over locations where traditional single-focus goniometer systems may be unable to be deployed, such as over a forested tree canopy. However, PARABOLA goniometers are unable to sample the BRDF for a single target, making them difficult to link directly to pixel reflectance.

Figure 2.11: The PARABOLA-2 goniometer instrument (NASA, 2000)

2.6 Models in Remote Sensing

2.6.1 Mixed Pixels

One of the fundamental challenges in satellite remote sensing is the identification of what exists within a pixel (Cracknell, 1998). The pixel, the smallest addressable image element, is a model created through the collection and subsequent processing of an analog signal obtained within the instantaneous field of view (IFOV) an optical sensor system (Desai, 2008). The difficulty in identifying what exists within a satellite sensor's IFOV is due to the fact that the Earth's surface is generally not homogenous over large areas, such as the 30m spatial resolution of the imaging scanners onboard the LANDSAT satellites. This heterogeneity of the landscape causes what is known as the 'mixed pixel problem' wherein the area within the sensor's IFOV is composed of multiple, spectrally distinct surface types (Fisher, 1997; Cracknell, 1998).

Mixed pixels are caused by the presence of features which are small in scale compared to the size of the FOV, and can include various situations, including scenes containing of assemblages of sub-pixel sized objects, boundaries between different continuous scene elements within the area covered by the pixel, features existing within a gradient, and by linear features which do not fill the entire area of a pixel (Fisher, 1997). Visual representations of these various scenarios can be seen in Figure 2.12.

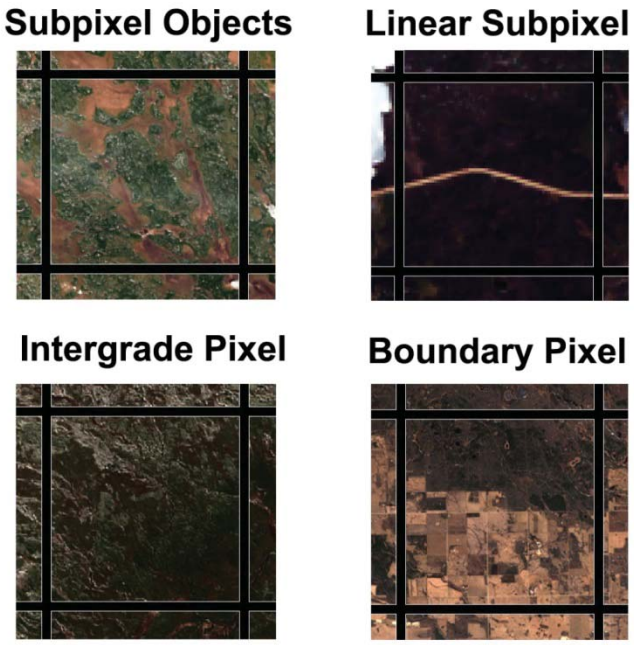

Figure 2.12: Cases of mixed pixels with four different causes (Image Source: USGS Products)

One of the most widely utilized methods for attempting to address the mixed pixel problem is referred to spectral unmixing, which is primarily accomplished using Spectral Mixture Analysis (SMA) (Adams et al., 1993). SMA allows researchers to model the spectra and composition of a mixed pixel as a weighted combination of representative spectral profiles for pure samples of each of the surface cover types visible in the scene. These theoretical 'pure' spectral samples of each surface type are known as endmembers, each having a specific fractional abundance in the area covered by the pixel (Keshava & Mustard, 2002). SMA in vegetation RS has been utilized at many scales in order to determine subpixel components of natural surfaces, ranging from landscape-scale determination of land cover to determination of the vegetative characteristics individual plant canopies (Roberts et al., 1992; Roberts et al., 2004; Peddle & Smith, 2005).

While work in SMA has provided some headway in addressing mixed pixels, the problem is further complicated by the complex issue of equifinality. This refers to the fact

that a single pixel reflectance value can be derived through any number of widely differing causative situations. As a result, there is no single, transportable solution to solving the problem of determining what's in a pixel.

2.6.2 Endmember Spectra

In the case where a solution to the mixed pixel problem is required for data collected via an aerial or satellite imaging platform, the processes used in spectral unmixing can vary in methodology and effectiveness. The most rigorous, as well as accurate, methodology researchers can employ involves the use of field-based ground truth samples of the different types of land surface types existing within the scene (Abuelgasim & Strahler, 1994; Keshava & Mustard, 2002). When this approach is utilized, researchers may use a spectroradiometric measurement device to attempt to collect a pure representative spectral measurement for each of the separate land cover types, generally through the use of optically thick stacks of the materials found in the scene (Goward et al., 1994; Peddle & Smith, 2005).

A spectrally pure sample of a specific ground cover type is referred to as an endmember. If endmember spectra for each land cover type cannot be obtained, reflectance libraries generated in previous studies can be utilized in order to obtain spectral data for a specific land cover type assumed to exist within a pixel's area (Dennison & Roberts, 2003). However, it should be noted that endmembers are fundamentally a theoretical construct; no spectral sample can be a truly pure representation of a species or ground cover type due to imperfect sensor abilities, and this fact is compounded due to effects such as intra-species variation which make it impossible for any given spectral sample to be pure and perfectly representative.

This intra-surface and intra-species spectral variance can be a result of a multitude of factors, and in fact, in vegetation can be constantly in flux due to seasonality and senescence (Miller et al., 1991). However, laboratory experiments utilizing man-made targets have the distinct advantage of providing endmember data that is highly stable and uniform, aiding in collecting spectral samples with a high level of representativeness and spectral purity. Spectrally stable materials that are not subject to changes in spectral reflectance due to factors such as seasonal variation or the effects of senescence allow for the development of laboratory experiments that are easily repeatable over indefinite time periods.

2.6.3 Empirical Vegetation Models

The use of remote sensing reflectance data to derive information related to vegetation biophysical variables inherently implies the use of a model. There are two basic classes of models used in this task: empirical models such as vegetation indices (VIs), and physically-based models capable of being inverted to derive biophysical information (Huete et al., 2014).

Empirically-based VIs have been developed based on the principle of utilizing an spectral absorption feature, such as that caused by chlorophyll absorption in the red (670 nm) region of the EMS, and a non-absorbing spectral feature, such as that found in the near-infrared (NIR) (800nm), in order to provide a robust measure of vegetative greenness or moisture content on a pixel-by-pixel basis (Gao et al., 2000; Huete et al., 2014). This combination of wavelengths is useful for this purpose because the amount of red light absorbed by healthy green vegetation is greater than that absorbed by unhealthy vegetation, while the inverse is true for NIR light.

A wide variety of VIs have been developed with the intention of modelling a range of biophysical variables based on the comparison of reflectance characteristics in two or more spectral bands or wavelengths in the VIS-NIR portion of the EMS (Agapiou et al., 2012). A comprehensive evaluation of a collection of 71 popular VIs was performed by Agapiou et al. (2012), which are divided into two categories, broadband VIs and narrowband VIs. The primary difference between the two main categories of VI is the spectral resolution of the data utilized in the model.

One of the most widely studied VIs, the Normalized Difference Vegetation Index (NDVI), was introduced following the discovery of a correlation between aboveground green biomass and values calculated via computing ratios of bands 5 and 7 from the Multispectral Scanner (MSS) onboard the first Landsat satellite (Rouse et al., 1974). The NDVI value of a pixel containing vegetation is driven by the spectral properties of the targets in the scene, and is therefore controlled by the vegetation's foliage density, chlorophyll content, and the effects of non-photosynthetic vegetation components, such as senescent vegetation and stems (Asner, 1998). While the NDVI itself is not considered itself be an ECV, there is a theoretical basis for relationships between NDVI and these fundamental variables, such as FAPAR and LAI (Tucker & Sellers, 1986; Myneni & Williams, 1994; Wang et al., 2005).

The NDVI has been proven as a useful diagnostic tool, and has been used in ecological studies involving forest management and agriculture, among others (Running & Nemani, 1988; Maselli, 2004; Mkhabela et al., 2011). While these empirical models have been shown to be moderately accurate and robust, and have seen extensive use in ecological studies, they are limited by their lack of a physical link to the real-world. Additionally, vegetation indices have been shown to have a high degree of variability for

a single target based on changes in viewing and illumination angles, functionally limiting their utility in many applications (Coburn et al., 2010; Coburn & Noble, 2016). These significant drawbacks emphasize the requirement for the implementation of non-empirically based models which are able to take into account the effects of Sun-sensor-target geometry and surface structure in order to more accurately model vegetation characteristics.

2.6.4 Canopy Reflectance Modelling

There have been many attempts in recent decades to develop mathematical models for the purpose of simulating bidirectional reflectance for vegetative land cover, which at its core attempts to model electromagnetic radiation's interaction with vegetative canopy surfaces based on certain assumptions made about the structure of the vegetation canopy being studied (Suits, 1973, 1983; Li & Strahler, 1985). These Canopy Reflectance Models (CRMs) provide improved accuracy in estimation of biophysical-structural information compared to traditional empirical methods such as vegetation indices, which exist exclusively within a statistical domain; and are useful in their ability to be used in areas without *a priori* knowledge of the structural parameters of the area being modelled (Hall et al., 1997; Peddle et al., 2010). These proven advantages of canopy reflectance modelling have been a primary driving factor behind increased research interest in the field.

The field of canopy reflectance modelling has branched in several directions since the first implementation of a vegetative canopy reflectance model by Suits (1973). All canopy reflectance models in use fall within four major categories: turbid medium models, hybrid models, computer simulation models, and geometric optical models (Goel,

1988). While all of these types of canopy reflectance models have their own advantages and disadvantages, this study will focus primarily on the field of geometric optical canopy reflectance modelling. Geometric optical canopy reflectance models represent individual trees within a scene as simple geometric shapes (often referred to as protrusions) with known dimensions, existing above a uniform ground surface that has known reflective properties (Goel, 1988). Geometric optical models have been developed with several types of 3-dimensional geometric shapes used to represent the individual trees in the scene, such as cylinders, spheres, cones, flat disks, among others (Hall et al., 1997; Strahler, 1997; Peddle et al., 2001b; Peddle et al., 2010).

Canopy reflectance models are capable of being run in two distinct modes, referred to as forward mode and inverse mode. When a canopy reflectance model is run in forward mode, it uses structural, geometric, and spectral inputs in order to model pixel-level BRF values for a scene (Li & Strahler, 1986; Asner et al., 1998). When a model is run in inverse mode, the opposite process occurs; a pixel-level BRF value is used as an input, and the modelling output consists of structural and geometric information about the scene being modelled. Model inversion for the purpose of estimating canopy structure in pursuit of large-scale forest biophysical-structural monitoring is the main thrust for development of these models.

2.6.4.1 Geometric Optical Canopy Reflectance Modelling

Geometric optical canopy reflectance modelling is primarily based on the aerial-proportion spectral mixing model, wherein the pixel-level reflectance for a given area of open forest canopy is considered to be composed of varying sub-pixel proportions of four distinct components: the area of the forest canopy that is illuminated (Sunlit Canopy), the

area of the background that is illuminated (Sunlit Background), the area of the canopy that is not illuminated (Shadowed Canopy), and the area of the background that is not illuminated (Shadowed Background) (Strahler & Jupp, 1990). This modelling technique relies upon the further assumption that the amount of variation in spectral reflectance between the four different types of pixel components is greater than the amount of spectral variation within each of these types of forest components; therefore each component may be assigned a single representative spectral reflectance per wavelength (Li & Strahler, 1986; Asner et al., 1998).

In many geometric optical modelling studies, a three-component model rather than a four component model is used for simplicity. In a three component model, the two shadowed components are assumed to have a singular representative reflectance value, based on the assumption that the reflectance values of the two shadowed components are both extremely similar to one another, while also having miniscule values, rendering the two components to be functionally the same in terms of spectral reflectance (Schaaf & Strahler, 1993). Based on this concept, the geometrical-optical modelling software used in this project utilizes a three component model. The endmember data collection techniques employed in this laboratory experiment were able to test the validity of this assumption, which will be explored later in this thesis.

2.7 Li & Strahler Geometric Optical Mutual Shadowing (GOMS) Model

This section provides a detailed overview of the GOMS canopy reflectance model, as implemented in Li and Strahler (1992). While the majority of the equations and definitions reviewed in this section are from that paper, several derivations of the same model described in Strahler and Jupp (1990), Soffer (1995), and Schaaf et al. (1994) are

included for clarity. The majority of this overview will focus on the calculation of the abundances of the two sunlit forest components, the sunlit canopy (K_c) and the sunlit understory (K_g).

In order to model BRF values, GOMS uses a modified version of the BRDF equation introduced by Nicodemus. The implementation of GOMS in Li and Strahler (1992) models the BRDF of a pixel as the limit of its directional reflectance factor $R(i, v)$:

$$R(i,v) = \ K_g G + \frac{C}{A} \iint_{A_c}^{Ag} \frac{< i, s >}{cos\theta_i} \frac{< v, s >}{cos\theta_v} ds \tag{2.8}$$

where ds represents a Lambertian surface over the area A of a pixel, K_g refers to the proportion of sunlit understory over the total pixel area (A_g/A), G refers to the representative reflectance of the understory, C refers to the representative reflectance of the crown's surface, the figures within the angle brackets refer to the cosine of the phase angle between the illumination direction i, the viewing angle v, and the surface normal direction s; θ_i and θ_v represent the zenith angles of illumination and viewing, respectively, and the double integral sign signifies that the signal is integrated over the area of the pixel. Through the use of these variables, the equation is able to create a direct physical link between directional reflectance of a scene and the spatial structure of the scene, as well as the scene's materials' component reflectance characteristics.

GOMS, which is based upon the aerial-proportion model, follows the assumption that pixel-level reflectance can be represented as a weighted linear combination of component reflectance of each ground cover component type allows GOMS to be expressed in a simplified manner as

$$R(i,v) = K_g * R_g + K_c * R_c + K_z * R_z \quad (2.9)$$

where the pixel-level bidirectional reflectance of an open forest canopy $R(i,v)$ is represented as a summation of the Lambertian endmember reflectance values of the three contributing forest components sunlit understory (R_g), sunlit canopy (R_c), and shadowed component (R_z.) weighted by their respective proportions within the area of the sensor's field of view (denoted as K_g, K_c, and K_z) at specified viewing (v) and illumination (i) angles (Schaaf et al., 1994). In order to compute the theoretical link between pixel-level reflectance and canopy structure, GOMS requires the input of several variables, shown in Table 2.2.

Table 2.2: GOMS model inputs.

Symbol	Variable Description	Units
Λ	Forest density	Trees/cm^2
B	Vertical crown radius	cm
R	Horizontal crown radius	cm
H	Height to crown center	cm
Dh	Tree height distribution	Dimensionless
Sc	Sunlit Canopy Endmember Spectra	% Reflectance
Sg	Sunlit Understory Endmember Spectra	% Reflectance
Sz	Shadow Endmember Spectra	% Reflectance
SZA	Illumination zenith angle	Degrees
SAZ	Illumination azimuth angle	Degrees
VZA	Viewing (sensor) zenith angle	Degrees
VAA	Viewing (sensor) azimuth angle	Degrees
SLP	Slope	Degrees
ASP	Aspect	Degrees

2.7.1 GOMS Geometric Canopy Description

The Li & Strahler (1992) model is the result of several years of model development and evaluation. Early versions of the model represented the discrete coniferous canopy elements as cones (Li & Strahler, 1985; Asner et al., 1998). Strahler

and Jupp (1990) first described spheroids-on-sticks (where the 'sticks' refer to theoretical structures that allow the spheroids to be located above the background, but do not cast a shadow) as a more suitable geometric characterization of coniferous canopy elements, while also facilitating the extension of the model for use with other types of trees and shrubs.

The physical descriptors of the individual spheroids-on-sticks most important to the computational model results are two ratios, (h/b) and (b/r), where h is the height to crown center, b is the spheroid's vertical half-axis, and r is the spheroid's horizontal radius. A third geometric parameter of the forest, ($\lambda \times r^2$), links the other two parameters to the overall scale of the pixel being modelled through the stem density of the forest in the scene, λ. These three geometric parameters provide the mathematical basis for a computationally viable three-dimensional geometric-optical canopy reflectance model. A schematic showing the geometry of a spheroid on a stick can be seen in Figure 2.13.

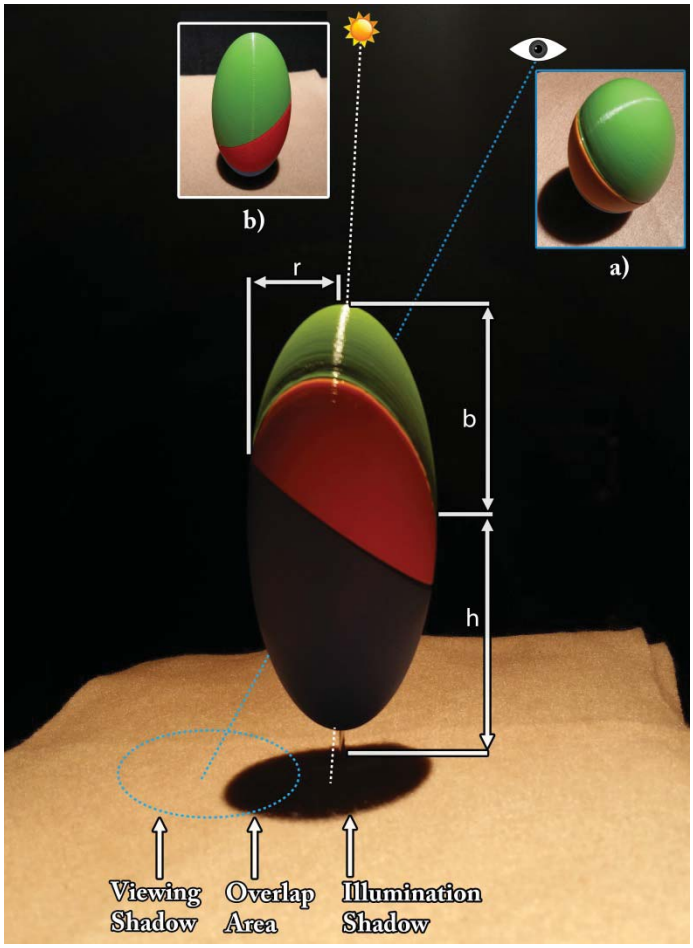

Figure 2.13: Depicts geometry of a 'spheroid-on-a-stick', including descriptions of associated geometric parameters and visual representation of the concepts of illumination shadow and viewing shadow. The inset images a) and b) illustrate the visual representation of the area of the spheroid that is viewed and illuminated, respectively. The green section of the spheroid represents the area that is both illuminated and viewed, the orange section is viewed but not illuminated, the red section is illuminated but not viewed, and the blue section is neither illuminated nor viewed.

.

In order to provide a reasonable amount of tractability for the computational model to determine shadow proportions at varying illumination and viewing angles, a geometric transformation is applied to the spheroids in the Li & Strahler (1992) model. This transformation is described by equation (7.7):

$$\theta' = tan^{-1}[\left(\frac{b}{r}\right) \times \tan(\theta)] \tag{2.10}$$

where it is assumed that the opaque tree crowns have the shape of a spheroid with a vertical half-axis equal to b, and a horizontal radius equal to r. This geometric transformation, denoted by θ', describes the conversion of a given viewing or illumination angle θ to an angle which would cause the spheroid to cast a shadow with a projected area equal to that which would be cast by a sphere, and eliminates the problem of varying apparent vertical axes caused by variation in θ. The scene in any given open forest pixel modelled by GOMS is modelled using the aerial-proportion model, where the scene is considered to be composed of only four types of elements: sunlit and shadowed canopy, and sunlit and shadowed understory. Figure 2.14 illustrates the concept of the aerial-proportion model in the context of a single spheroid on a stick.

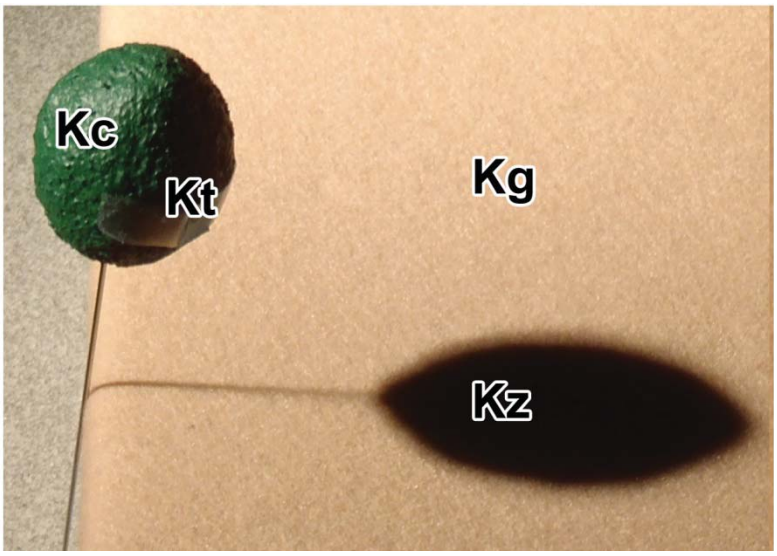

Figure 2.14: Geometry of physical model trees in relation to the aerial-proportion model, illuminated from left. Four-component model scene components sunlit canopy (Kc), shadowed canopy (Kt), sunlit background (Kg), and shadowed background (Kz) are marked. In a three- component model, Kt and Kz are considered to be the same component.

2.7.1.1 The Sunlit Background Component

The proportion of viewed sunlit background (K_g) in the total area of the scene is modelled through the use of Boolean set theory, and employs a version of the fundamental Boolean formula as described in Serra (1982) to determine the probability that a given portion of the background will be both illuminated and viewed by the sensor (Li & Strahler, 1992). The Boolean model depicts the individual tree canopies within the forest as a randomly distributed assemblage of components known as grains, with the gaps in between the grains referred to as pores (Strahler & Jupp, 1990). The following function is employed in the Boolean model in order to simulate the expected reduction in probability of the sensor's ability to see a given portion of the sunlit background as pore density and the average area of the pores increase:

$$K_g = e^{-\lambda \pi R^2 [sec\theta_i' + sec\theta_i' - \overline{O}(\theta_i, \theta_v, \phi)]} \tag{2.11}$$

The existence of the hot spot phenomenon must be accounted for in order to accurately model the BRDF of open tree canopies. The hot spot is primarily driven by the process of objects hiding their own shadows, which can also be described as the overlap of the 'illumination shadow' (area blocked from illumination) and the 'viewing shadow' (area obscured to the observer by an individual tree crown), as depicted in Figure 2.14. In order to account for the effects of this shadow hiding, the calculation of K_g in the GOMS model employs the geometric overlap function $\overline{O}(\theta_i, \theta_v, \phi)$, which directly models the average amount of overlap between the viewing and illumination shadows in the principal plane via geometric optical techniques. Figure 2.15 shows the concept of shadow-hiding which drives the BRDF hot spot.

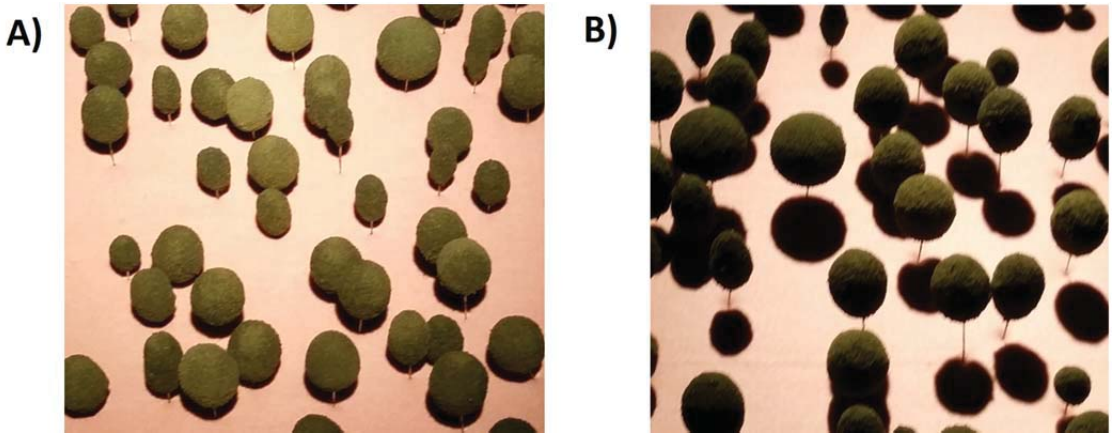

Figure 2.15: Physical model forest canopy components viewed in the backscatter direction near the location of the illumination source (A) showing the shadow hiding driving the hot spot effect, and viewed in the forward-scatter direction (B) where illumination shadows are highly visible. The overlap function models this effect.

The overlap function has been developed to approximate the shape of the hotspot using two situation-dependent cases. The first case considers the effect of overlap in the principal plane, where $\phi = 0$ or $\phi = \pi$, and the viewing and illumination shadows are oriented in the same plane. In this case, the overlap area is approximated as an ellipse with one axis equal to the length of the overlap and the other axis equal to the width of the crown, and is calculated as

$$\overline{O}(\theta_i, \theta_v, \phi) = \frac{1}{2}[sec\theta_i' + sec\theta_i' - \frac{h}{b}|tan\theta_i' - tan\theta_i' cos\phi|] \tag{2.12}$$

This implementation of h and b in the model clearly shows the effect of the shape and height of the spheroids on the calculated overlap, and thus upon the overall shape of the hotspot. In this case, when the overlap area reaches zero, the effects of the overlap function which drive the hotspot disappear.

The second case considers all other possible viewing locations outside of the principal plane. The values in the second case are not calculated directly through geometric optical techniques, but rather through the implementation of a linear response function which approximates the overlap area's diminution as azimuthal distance from the

principal plane increases. The location of the azimuthal boundary of the hotspot, outside of which the linear function is applied, is approximated as:

$$\Phi = \frac{4R}{h(tan\theta_v + tan\theta_i)} \,. \tag{2.13}$$

Through Monte Carlo simulation methods, this approximation has been shown to closely match simulated results for many solar zenith angles and crown shapes, and delineate the edges of the hotspot with reasonable accuracy (Li & Strahler, 1992).

Exact calculations for overlap in the principal plane and the principal cone (PC), which refers to the area covered by the azimuthal movement of the sensor at a zenith angle identical to that of the illumination source, have been calculated as seen in Schaaf and Strahlerl (1994). However, the implementation of the GOMS modelling software used in this study is based on the version of GOMS utilized in Li & Strahler (1992) and does not take these calculations into account; thus these calculations for exact solutions will not be considered in this study.

2.7.1.2 The Sunlit Canopy Component: Mutual Shadowing Effects

An important advance in geometric-optical modelling of forest canopies was the introduction of the concept of mutual shadowing. Mutual shadowing refers to the case where shadows cast by individual trees fall upon one another (Li & Strahler, 1992). The degree of mutual shadowing is dependent upon illumination and viewing locations, as well as the average spheroid size and density (Li & Strahler, 1992). The implementation of GOMS in Li & Strahler (1992) applies one-stage geometric optics to model the effect of the relationship between mutual shadowing in the illumination and viewing domains.

Given that, in the direction of illumination, the total area of the apparent ellipsoid projected by each spheroid is:

$$\pi R^2 \sec\theta_i' \tag{2.14}$$

then the total projected, illuminated canopy area in the scene as a proportion of the scene's total area when no mutual shadowing occurs is:

$$\lambda\pi R^2 \sec\theta_i' \tag{2.15}$$

however, when mutual shadowing is taken into account, the projected area will be:

$$1 - e^{\lambda\pi R^2 sec\theta_i'} \ . \tag{2.16}$$

The degree of mutual shadowing in the illumination direction is represented as an index, with a value of zero representing a total lack of mutual shadowing, and a value of one representing total mutual shadowing. The proportion of the ground-projected area for the total number of spheroids in the scene which are obscured from illumination due to mutual shadowing (M_i) is calculated as:

$$M_i = 1 - \frac{1 - e^{-\lambda\pi R^2 sec\theta_i'}}{\lambda\pi R^2 sec\theta_i'} \tag{2.17}$$

In a similar manner, the degree of mutual shadowing in which the areas projected by the spheroids are obscured from viewing (M_v) is calculated as:

$$M_v = 1 - \frac{1 - e^{-\lambda\pi R^2 sec\theta_v'}}{\lambda\pi R^2 sec\theta_v'} \tag{2.18}$$

It is apparent based on these definitions of mutual shadowing that the amount of sunlit canopy viewed by the sensor is dependent upon the differences between the illumination angle and viewing zenith and azimuth angles. The assumption that both viewing and illumination shadows will be concentrated in the lower portion of the spheroid allows the definition of both a M_i and a M_v boundary, which can be seen in figure 2.16.

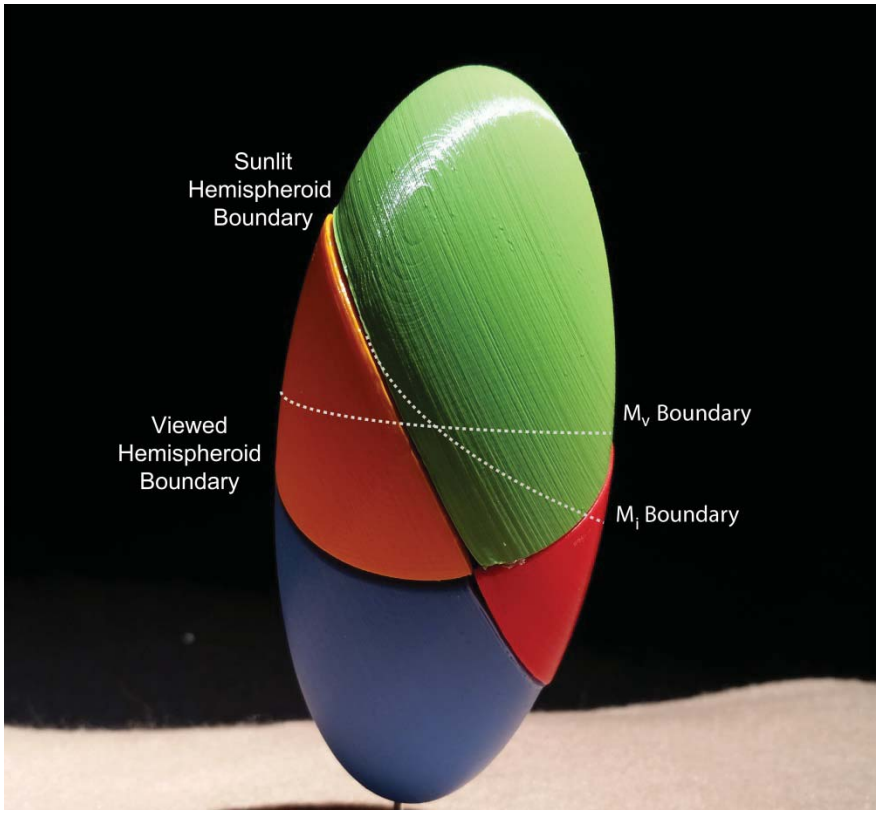

Figure 2.16: Diagram showing the mutual shadowing boundaries

Following the calculation of the abundance of the K_G component in the scene, the proportion of the total area in the scene that is still able to be illuminated (K_C) is defined by the f-ratio,

$$f = \frac{K_C}{1 - K_G} \tag{2.19}$$

In the case where a single spheroid exists within a pixel, its projected area that is able to be viewed is equal to

$$\Gamma_v = \pi R^2 sec\theta'_v \tag{2.20}$$

The portion of this area which is also illuminated is equal to

$$\Gamma_c = \pi R^2 sec\theta'_v \frac{(1+< i', v' >)}{2} \tag{2.21}$$

where <i′,v′> is the cosine of the phase angle between the modified illumination and view angles; calculated as

$$< i', v' >= \cos(\theta'_g) \times \cos(\theta'_v) + \sin(\theta'_g) \times \sin(\theta'_v) \times \cos(\phi) \tag{2.22}$$

The combined area of viewed crown plus illumination shadow projected onto the background is, therefore, the sum of the area of the two projected spheroids, with the overlap area subtracted from the result of that summation:

$$\Gamma = \pi R^2 [sec\theta'_i + sec\theta'_i - O(\theta_i, \theta_v, \phi)] \tag{2.23}$$

Therefore, *F*, the ratio of $\frac{\Gamma_C}{\Gamma}$ in the case of the single spheroidal crown, can be defined as

$$F = \frac{\Gamma_C}{\Gamma} = \frac{\frac{1}{2}(1+< i', v' >)sec\theta'_v}{sec\theta'_i + sec\theta'_v - O(\theta'_i, \theta'_v, \phi)} \tag{2.24}$$

In cases where only one crown is present in a pixel, it can easily be shown that *f* = *F*. When *n* number of crowns (and subsequently, shadows) exist within a pixel, but no mutual shadowing exists, it holds that *f* = *F*. However, as the number of crowns *n* in a pixel increase, mutual shadowing is likely to begin. The mutual shadowing proportion, *M*, which describes the ratio of total shadowing in both the illumination and viewing domains cast by a single crown that falls upon another crown rather than onto the background, is defined as:

$$M = 1 - \frac{1 - K_g}{\lambda \Gamma} \tag{2.25}$$

The effect being modelled in the *f*-ratio involves the reduction of the amount of sunlit and viewed surface of a given crown when hiding from viewing or illumination occurs. In the case where there are multiple crowns able to be viewed and illuminated in the scene, the *f*-ratio can be defined as

$$f = \frac{n\Gamma_c - \sum \Delta_{A_C}}{A(1 - K_g)} \tag{2.26}$$

which can be represented as

$$f = F\frac{1 - - \sum \Delta_{A_C} / (n\Gamma_c)}{1 - M} \tag{2.27}$$

where $\sum \Delta A_C$ is the total amount of decrement from $n\Gamma_c$ to A_C, i.e., the area of the crown surface that is sunlit and viewed, and where *n* is the count of the total number of spheroids in a pixel. $\sum \Delta_{A_C}$ can be expressed as three terms, describing a diminution caused by mutual shadowing in the viewing domain, and a diminution caused by mutual shadowing in the illumination domain, less the values of those mutually shadowed components in both domains:

$$\sum \Delta_{A_C} = n\Gamma_v(P_v M_v + P_i M_i - P_o) \tag{2.28}$$

where P_v and P_i both represent average proportional projected areas based on conditional probabilities; the first term referring to the probability that a crown surface will face the Sun given the condition that it is mutually shadowed in the viewing domain, and the second term referring to the probability that a crown surface will be viewed given the condition that it has been shaded in the illumination domain.

The term P_o contains three components, each based on different cases of surface elements. The first, wherein surface elements intersect other crowns, do not contribute to the hotspot or the shape of the BRDF. The second, wherein surface elements overlap another crown in either the illumination or viewing domain, have a distinct effect on the hotspot due to the spatial overlap of shadows. The third, wherein surface elements fall within one crown's illumination shadow and in another's viewing shadow, contribute to

the phenomenon of preferentially viewing the top of the crown. This definition of $\sum \Delta_{A_C}$ allows for the use of a single expression to define the f-ratio:

$$f = F\frac{1 - \Gamma_v(P_v M_v + P_i M_i - P_o)/\Gamma_c}{1 - M} \tag{2.29}$$

With the terms P_i, P_v, and P_o defined, the methods used to model these three probabilities can be discussed. The implementation of GOMS in Li & Strahler (1992) presents two extreme cases, in each of which the three probabilities are dealt with simultaneously. The first case, known as the "Uniform Height" case, assumes a forest of uniform canopy height, where all illumination and viewing shadows fall under the M_i and M_v boundaries, respectively. In this case, the intersection of these two shadows and their effect on hotspot contribution will be included in the intersection of the boundaries.

In the uniform height case, it is useful to consider the implications of the relationship between the viewing and illumination zenith angles in the SPP, and its effect on the M_v and M_i boundaries. In particular, it is useful to consider the M_v and M_i boundaries, as well as the illumination boundary (as seen in Fig. 2.15), as planes intersecting the spheroid at its center; otherwise known as great ellipses. The angle between the M_i great ellipse and the illumination boundary's great ellipse is calculated as:

$$\theta_{M_i} = cos^{-1}(1 - 2M_i) \tag{2.30}$$

Similarly, the angle between the M_v great ellipse and the viewing boundary's great ellipse is:

$$\theta_{M_v} = cos^{-1}(1 - 2M_v) \tag{2.31}$$

At the location of the hotspot, the M_v and M_i boundaries completely overlap one another, as can be seen in Fig. 2.15(a). This results in the calculations of the three probabilities being represented by the relationships:

$$P_v = P_i = 1, \tag{2.32}$$

$$P_o = M_v = M, \tag{2.33}$$

and

$$f = F = 1. \tag{2.34}$$

The second situation of consideration, as seen in Fig. 2.15(b), occurs in the SPP case where $\theta_v > \theta_i$. In this case, it can be seen that the M_v boundary falls higher on the spheroid than the M_i boundary. In this situation, the P_v term can be calculated as the proportion of the area between the M_v boundary and the illumination boundary out of the entire area falling below the M_v boundary, represented as

$$P_v = \frac{M_v \Gamma_v - (\Gamma_v - \Gamma_c)}{M_v \Gamma_v} \tag{2.35}$$

In this case, the value of P_i is one, and the value of P_o functions to cancel out the M_i term. With these terms defined, the *f*-ratio can be simplified as

$$f = \frac{1 - e^{-\lambda \pi \Gamma_v}}{(1 - K_g)}. \tag{2.36}$$

This result can be used to determine the fact that, as the viewing zenith angle increases beyond the illumination zenith angle, the value of the *f*-ratio will not deviate far from one if coverage is high. This result is conducive with the visual representation in Fig. 2.15(b) showing that the amount of viewed crown that is shadowed from illumination is close to zero.

The third case to consider for the uniform forest in the SPP occurs in the situation when $\theta_i > \theta_v$, but θ_v has not yet reached the nadir position. A visual representation of this case can be seen in Fig. 2.15(c), and as can be seen, the M_i boundary falls above the M_v boundary. As a result, $P_v = 1$, $P_o = M_v$, and

$$P_i = \frac{1 - \cos(\theta_{M_i} - \theta_i' + \theta_v' cos\phi)}{1 - cos\theta_{M_i}} \tag{2.37}$$

however, P_i may also be equal to zero if the M_i boundary is not sufficiently high on the spheroid to be visible in the sensor's field of view.

The fourth, and final, possible situation for the uniform forest case in the SPP occurs when θ_v moves beyond the nadir point to a viewing position opposite the illumination source. The average crown geometry seen by the sensor in this case would look similar to Fig. 2.15(d), which features a projection of an "average crown", where $\phi = \pi/2$ in order to clearly display the boundaries of the four great ellipses. The value of P_i in this case has a value of $\phi = \pi$ due to the azimuthal location of the sensor in relation to the boundaries. The value of P_v in this case is the proportion of M_v over the boundary of illumination:

$$P_v = \begin{cases} \dfrac{1 - \cos(\theta_{M_v} - \theta_v' + \theta_v' \, cos\theta)}{1 - \cos\theta_{M_v}}, & (\theta_{M_v} - \theta_i' + \theta_v' \, cos\theta) \geq 0 \\ 0, & (\theta_{M_v} - \theta_i' + \theta_v' \, cos\theta) < 0 \end{cases} \tag{2.38}$$

In the case where θ_v is located in the SPP between the hot spot and nadir, P_v is equal to one, which causes a discontinuity at nadir due to the assumption that all of the shadows are cast below the $M_v$boundary. When θ_v passes nadir, a situation is created where the viewing shadow falls on the opposite side of the crown in comparison to the

illumination shadow, the sudden change of which is reflected in this discontinuity at nadir. An illustration of the boundary locations as they fall upon a single spheroid can be seen in Figure 2.17.

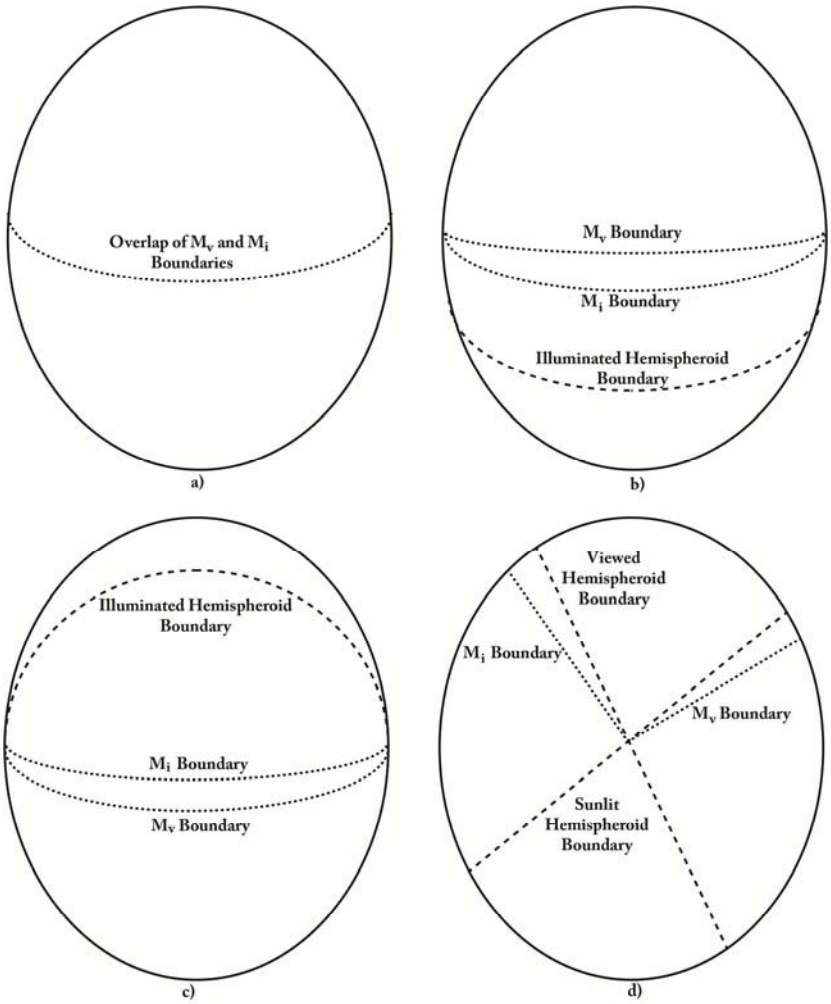

Figure 2.17: Locations of the great ellipse boundaries, illustrating the effects of mutual shadowing in the case where viewing takes place in the SPP, in four different illumination and viewing situations. (a) occurs when measurements are taken at the hot spot, (b) occurs when $\theta_v > \theta_i$ (c) occurs when $\theta_v < \theta_i$, and (d) occurs when θ_v is on the opposite of nadir in comparison to θ_i (Adapted from Soffer, 1995).

With the probability values determined in the "Uniform Forest" case, the conditions upon which the probability values are determined in the "Random" forest case can be approximated. In the random case, the illumination and viewing shadows are

scattered on other crowns independently, and as such, the hotspot contribution of mutual shadowing can be ignored. The independence of the M_v and M_i boundaries yield a value of

$$\sum \frac{\Delta_{A_c}}{n\Gamma_c} = M_i \tag{2.39}$$

which leads to a simplification of the value of F:

$$F = f. \tag{2.40}$$

However, in all realistic scenarios, neither of these two extreme cases are likely to take place. Rather, the true nature of all practical scenarios in which this model is used will correspond to a case in which the uniformity of the forest will fall somewhere in the range between these two extremes. Exactly where a given situation falls along the continuum between these two extremes is determined exclusively by the height distribution of the forest. Investigation of this problem has led to the finding that, in the case where the height distribution of the forest is very large, the trees located in the upper bounds of the distribution will have a much larger effect on the BRF values of the canopy than those trees whose heights fall within the lower bounds of the distribution (Li & Strahler, 1992).

With these quantities known, the f-ratio is able to be determined, allowing for the derivation of the total sunlit canopy component, K_C, with the effects of mutual shadowing taken into account. It should be noted that in Equation (2.8), the term(s) representing the shadow component(s) are absent, as they are not taken into account in this version of the GOMS model. However, in the case of the three-component model such as that utilized in this study, once the contribution of the sunlit background (K_G) and

sunlit canopy (K_C) have been determined, the contribution of the shadowed component to the total overall reflectance can be easily derived using the equation

$$K_G + K_C + K_Z = 1 \tag{2.41}$$

A final representation of the GOMS model which is intended to provide a simple, straightforward overall summary of the above model description by based reducing the model down to its most critical parameters is shown in equation 2.39:

$$R = f(\theta_i, \Phi_i, \theta_v, \Phi_v, \theta_s, \Phi_s, nr^2, \frac{b}{r}, \frac{h}{b}, \frac{\Delta h}{b}, G, C, Z) \tag{2.42}$$

where R is pixel-level bidirectional reflectance; θ_i, Φ_i, θ_v,and Φ_v are the illumination zenith angle, illumination azimuth, viewing zenith angle, and view azimuth, respectively; Φ_s is the ground slope; θ_s is the ground aspect; nr^2 refers to the total nadir ground coverage of the trees and is based on $n * \pi\, r^2$, where n refers to the number of trees per unit area of the scene; b/r, which is the crown shape parameter with the most significant impact on viewed crown coverage density at off-nadir viewing locations; *h*/*b* is the crown shape parameter with the most significant impact on the total width of the hot spot in the azimuthal plain; Δh is the forest parameter showing the variance of the height distribution over the area sensed in a single pixel; and $\Delta h/b$ is the parameter which describes the discrete variance of the forest height distribution, and primarily has a significant impact on the shape of the BRDF (Fu et al., 2011; Ma et al., 2014; Li et al., 2015).

2.8 Physical Modelling in the Natural Sciences

With the GOMS model defined and its geometric-optical basis shown, it is important to provide context within which the utility of tangible models for the purpose of physical model validation can be placed. Natural physical processes often occur at too

large or complex a scale to allow researchers to properly define the driving factors and variables. In these cases, it is often helpful to develop tangible scaled down physical simulations to better understand, and subsequently more accurately model, these complicated physical processes.

A prime example highlighting the benefits of this tangible physically-based method of modelling can be found in the case of the Mississippi River Basin model (MRBM). Developed in response to the massive 1927 flood of the Mississippi River which displaced over half a million people and caused over a trillion dollars in damage (adjusted for inflation), the 220-acre scale model of the entire Mississippi river basin was built in order to recreate and understand the processes leading to floods via simulation in a time before computationally-based hydrological models were available (Torrey, 1948; Mars, 2016). This marvel of modern engineering consisted of a highly accurate scale model of the entire Mississippi River basin, the area of which spans 41% of the contiguous United States, and was used to understand flooding via physical simulation by allowing scientists to repeatedly adjust and subsequently test the effects of flood mitigation measures by releasing thousands of litres of water through its miniature river banks (Torrey, 1948; Mars, 2016). The complexity of the MRBM at multiple scales can be seen in Figure 2.18.

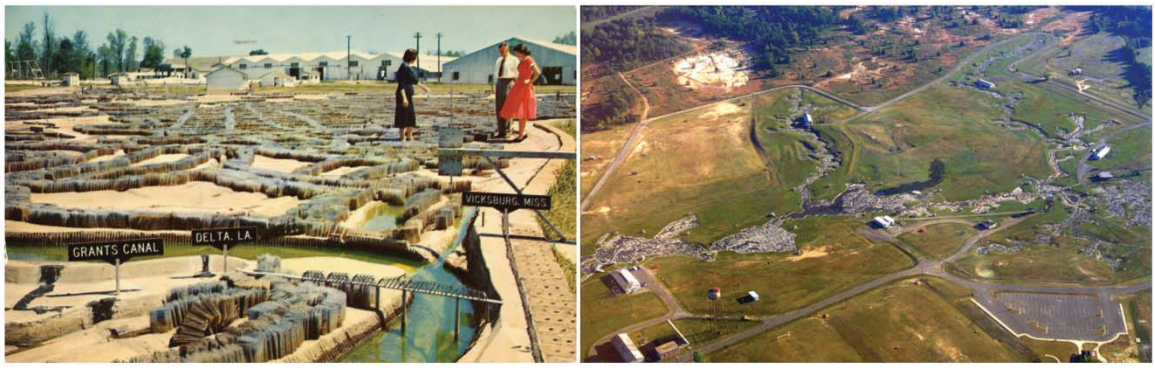

Figure 2.18: The Mississippi River Basin Model. The complexity and level of detail of the MRBM was impressive (left), given its expansive land area (right); the reward for which was high-quality data with a strict physical foundation (USACE, 2006; Malvaney, 2010)

The MRBM was capable of simulating past flood levels, as well as predicting future ones within inches of their true levels; a degree of accuracy which still to this day cannot be reached via computational modelling methods (Mars, 2016). This data was used to validate, and subsequently improve, mathematical flood models. These incredibly accurate results highlight scaled physical models' inherent usefulness in accurately capturing, and subsequently allowing for the better understanding of, the hyper-specific variables driving complex physically-based processes over large areas without requiring any computation whatsoever (Mars, 2016). Their strict physical basis inherent in their tangibility renders this type of simulation an incredibly valuable validation tool for physics-based models; particularly in their ability to allow researchers to refine models and correct for subtleties which otherwise may not be able to be identified.

Pixel radiance is driven by EMR, the behaviour of which is governed by well-understood laws of physics (Grum & Becherer, 1979). While the laws governing light and optics differ from those governing hydrology, our understanding of these processes is such that we know that the properties driving the phenomena being investigated will be sufficiently similar to allow them to be investigated via a downscaled physical simulation.

Thus, the scale-based simulation principles which led to the success of the MRBM are applicable to RS studies of geometric-optically based physical models, which simulate the physical processes governing EMR.

2.9 Laboratory Geometric Optical Model Validation

A crucial aspect of canopy reflectance modelling is model validation, wherein ground truth data collected using *in situ* spectral measurements is compared to modelled values in order to determine how well the model was able to simulate real-world conditions. Model validation studies for GOMS have been undertaken in projects utilizing remote sensing data acquired using satellite and airborne sensors, typically with data collected over forested areas alongside ground truth validation data collected in the field (Brown, 2002; Fournier et al., 2003; Peddle et al., 2004). However, existing goniometer systems are unable to collect multiangle measurements over an area of comparable to the footprint of a moderate-resolution RS pixel such as that acquired by Landsat, making it impossible to investigate whether the BRDF being simulated by the model accurately simulates that of the forest scene. The use of scaled physical simulations allows for transportability of complex, large-scale processes such as those driving the BRDF of an open forest canopy into a laboratory environment for investigation.

While this validation method is powerful, only one geometric-optical model laboratory validation study involving HRCF measurements of a physical forest could be identified (Soffer, 1995). This study utilized a scaled physical simulation where the structure of a real-life tree stand was modelled, a basis upon which provides excellent validation of data obtained via the GOMS model when applied to boreal forest imagery (Soffer, 1995). However, mechanical system used therein was not as advanced as

goniometer systems such as the ULGS-2. Additionally, there are currently no published validation studies of the GOMS computational model *itself* via physical simulation of its geometric-optical assumptions and parameters.

A properly designed laboratory simulation can be utilized to bridge this gap in knowledge between the GOMS model and reality. Physical simulations have been used to identify parameter constraints, or ranges thereof, outside of which the model breaks down. Additionally, the ability to physically view, from any angle, true endmember fractional abundances in a physical simulation will allow for physical validation of the Boolean model's probability-based outcomes, and subsequent model refinement, should it be required. Results may potentially provide a doorway for the identification of yet unidentified variables driving certain physical phenomena related to the BRDF of an open tree canopy, variables which may allow for further model refinement.

2.10 MODIS BRDF Product

MODIS has currently available data which was identified as potentially useful in creating a real-world link to the laboratory spectrodirectional measurements. The MODIS instruments are located onboard NASA's TERRA and AQUA satellites, and were launched with the objective of capturing an image of the entire earth every two days over a wide spectral range. The TERRA satellite with a MODIS sensor onboard can be seen in Figure 2.19. The MODIS instruments feature across-track scanners with wide FOVs which collect multiangle data at scan angles up to +- 55°, which functionally translates into viewing zenith angles as large as 65° when the curvature of the Earth is taken into account (Tan et al., 2006). This multiangle measurement capability has allowed for the development of an "off-the-shelf" BRDF product suite, referred to as the MODIS MCD43

BRDF/Albedo products, to be made available for the entire Earth's surface at an eight day temporal resolution.

Figure 2.19: The TERRA Satellite, upon which the first MODIS instrument was launched. (LMMS, 1999)

The MODIS BRDF/Albedo products are derived using a semi-empirical kernel-based BRDF modelling technique. Kernel-based BRDF models assume that the BRDF of a land surface can be described as a superposition of a number of spatially distinct scattering modes, termed kernels, and BRDF can subsequently be derived as a linear sum of these kernels (Roujean et al., 1992; Strahler et al., 1999). Its general form can be described as in equation 2.43:

$$BRDF = f_{iso} + f_{vol} \times k_{vol}(\theta_i, \theta_v, \Phi) + f_{geo} \times k_{geo}(\theta_i, \theta_v, \Phi) \quad (2.43)$$

where f_{iso} is a constant which corresponds to isotropic reflectance, k_{vol} refers to a kernel describing volumetric reflectance as a function of Sun-sensor geometry, k_{geo} refers to a kernel describing geometric-optical surface scattering, and the f_{vol} and f_{geo} terms refer to weighting coefficients corresponding to the volumetric and geometric scattering kernels, respectively.

These products are derived via the kernel model method by analyzing MODIS surface reflectance values for varying viewing geometries, and subsequently calculating the best-fitting weighting coefficients for the three kernels in the RossThick-LiSparse Reciprocal (RTLSR) semi-empirical BRDF model. In the RTSL model, the volumetric scattering kernel component k_{vol} corresponds to the RossThick kernel, derived by Roujean et al. (1992). The model assumes a dense canopy with a high LAI, from which the term thick is derived. The geometric scattering kernel component k_{geo} corresponds to the LiSparse model, a simplified derivation of the GOMS model.

The MODIS BRDF Parameters product (MCD43A1) provides, on a per-pixel basis at a spatial resolution of 500m, weighting coefficients which best fit to the three major kernel model components (f_{iso}, f_{geo}, f_{vol}) in RTLSR model which best describe a given location's land surface reflectance anisotropy based on multiangle MODIS observations of a single location. These coefficients, while primarily used to calculate MODIS' albedo and BRDF-corrected nadir reflectance products, are also capable of being applied directly to the RTLSR model to forward-model land surface reflectance for any given location at any combination of Sun-sensor geometry. In order to facilitate this functionality, the Algorithm for Modeling [MODIS] Bidirectional Reflectance Anisotropies of the Land Surface algorithm (AMBRALS) framework has been

developed, which allows for forward and inverse modelling using the RTLSR kernel model, amongst others (Wanner et al., 1997).

2.11 Chapter Summary

This chapter has presented a summary of the scientific concepts involved with spectrodirectional sampling, including the BRDF and the measurable quantity from which it is able to be estimated, the HCRF. The concept of goniometric measurement was outlined, along with various goniometer systems used for this purpose. The concept of a CRM was described, followed by a detailed outline of the GOMS CRM. Finally, the rationale for using a scaled forest model for investigating GOMS using a goniometer system was described.

3 METHODS

3.1 Objectives

The objective of this section is to provide a detailed description of the experimental design used in this study. A description of the materials and methods used to develop the model forest are discussed, as well as a description of how the forest was implemented in the laboratory with the ULGS-2. This description is followed by an outline of the methods used to implement GOMS, and the analyses performed upon the data.

3.2 Simulated Study Area

Two primary advantages of laboratory-based remote sensing experiments are their ability to allow researchers to customize illumination systems to simulate virtually any natural geometric illumination conditions, and to collect data unaffected by undesirable effects traditionally associated with data collected outdoors under natural lighting conditions, such as atmospheric attenuation (Sandmeier & Strahler, 2000). A customizable light source provides researchers with the opportunity to create a strict physical link between data collected in the field and laboratory-derived data by positioning the illumination source at an angle which simulates the Sun's location in the sky at any date, time, and location on Earth. This provides ample opportunity for robust laboratory validation of GOMS-derived results.

While the GOMS model laboratory validation can be undertaken at any set of arbitrary illumination angles, a main focus of the thesis based upon developing a meaningful physical basis within which GOMS can be better understood. Therefore, a physical link to real-world solar illumination conditions was implemented by selecting a

physical location upon the Earth, along with corresponding dates and times, at which to simulate the solar angle with the laboratory illumination system. The BOREAS Southern Study Area (SSA) Old Jack Pine (OJP) site, located North of Prince Albert, Saskatchewan, was selected to be the simulated site location. The site features a boreal forest stand of mature Jack Pine (*Pinus banksiana*) with an understory consisting largely of lichen (*Cladina stellaris*), with an average temperature of 1° C and 44 cm of annual precipitation. The BOREAS SSA OJP site The site can be seen in Figure 3.1.

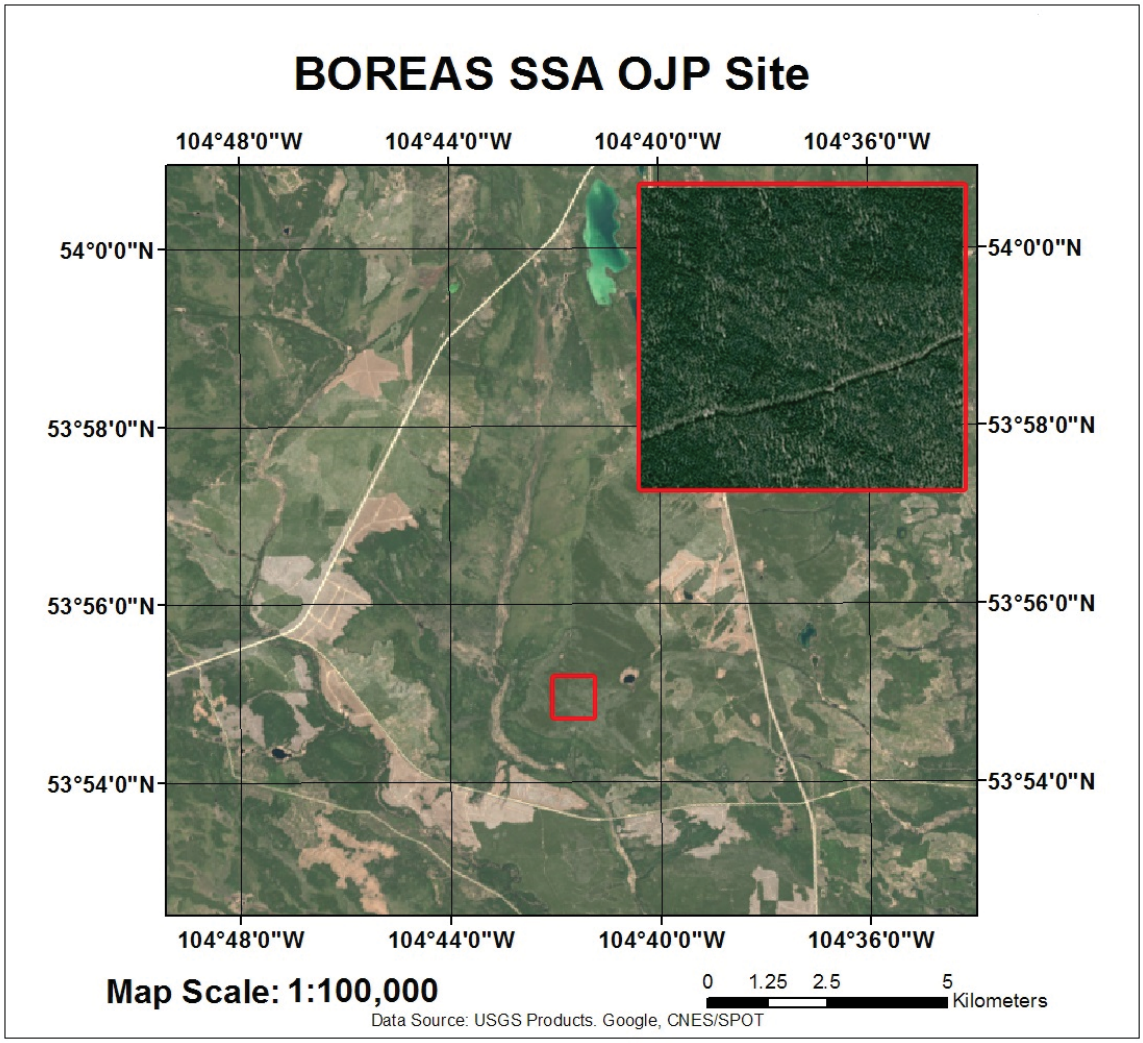

Figure 3.1: Map of BOREAS SSA OJP site area. Inlay shows high-resolution satellite imagery of OJP site area. BOREAS OJP flux tower site located near center of inlay. Understory can be seen, indicating an open forest.

To establish this physical link at the two physical bounds in terms of the annual solar angle cycle at this location on Earth, the solar zenith and azimuth angles at the BOREAS SSA OJP site were calculated for solar noon at the summer and winter solstices using the National Oceanic and Atmospheric Administration (NOAA) Solar Calculator. In the case of the summer and winter solstices, the calculated solar zenith angles were 30.47° and 77.28°, respectively. In both cases, the solar azimuth angle was 180°. Details for the relevant site parameters can be found in Table 3.1.

Table 3.1: BOREAS SSA OJP annual solar angle site parameters. Values correspond to the location of the onsite flux tower.

Site Parameter	Value
Latitude	53.91634° N
Longitude	104.69203° W
Summer solstice solar noon	13:00:36
Winter solstice solar noon	12:56:58
Summer solstice SZA	30.47°
Winter solstice SZA	77.28°

The BOREAS SSA OJP site has numerous features which render it an ideal simulated location for this study. The overall forest structure at the site consists of an open forest of Jack Pine. Being that a major assumption in GOMS is that it is modelling an open forest, the structure of which is outlined in Table 3.2, this site a logical location to select in a physical sense. However, the site canopy structure has further implications, in that the BOREAS SSA OJP site has both field-based and spaceborne multiangle reflectance data publically available. Utilizing these open-source datasets allows for a comparison between field data and laboratory data to be performed. These field and spaceborne datasets were sampled by the PARABOLA-2 instrument and derived from the MODIS MCD43A1 products, respectively.

Table 3.2: BOREAS SSA OJP Site forest canopy structural parameters (Soffer, 1995).

Parameter	
H (Tree height)	13.7 ± 2.5 m
h (Crown center height)	10.2 ± 2.5 m
b (Vertical crown radius)	3.5 ± 1.0 m
r (Horizontal crown radius)	1.2 m ± 25%
# of Trees	72 ± 10%
Superpixel Area	33 m x 33 m = 1089 m^2 ± 12%
Λ (Forest stand density)	0.0661 trees / m^2 ± 22%
λ x r^2	0.095 ± 72%
b/r	2.92 ± 53%
h/b	2.91 ± 53%
(h2-h1)/b	0.714

3.3 Development of Laboratory BRDF Facility

3.3.1 Physical Forest Model

Geometric-optical model validation studies can be performed on an assemblage of opaque simple geometric shapes projected over a contrasting background (Soffer, 1995). The GOMS model itself has a strict physical basis which models pixel reflectance based upon the physical processes which drive it in the real world. The GOMS model itself is ideal for a physical simulation in that it is sufficiently conceptually simple that it can be accurately recreated in the laboratory, while still being sufficiently complex to capture the processes driving pixel reflectance. However, a laboratory simulation where an assemblage of simple geometric objects representing trees as the GOMS computational model does for the purpose of geometric-optical model validation does not currently exist in the literature. The purpose of this section is to outline the development of this physical forest simulation.

3.3.1.1 Model Scale

Different processes drive bidirectional reflectance at different scales; therefore, scale is one of the primary considerations taken into account in the development of empirically-based and physically-based reflectance models (Woodcock & Strahler, 1987). CRMs are designed to simulate light's interaction with a plant canopy at a range of scales from the very fine (i.e. individual leaves) up to very large (i.e. the canopy level).

The GOMS model has been designed to simulate spectral data collected at spatial resolutions approximately the same size as those collected by the various Landsat satellites; ranging from the Multi Spectral Scanner (MSS)'s resolution of 80m x 80m to the 30m x 30m resolution of the more recent Landsat sensor systems, such as Landsat 7's Enhanced Thematic Mapper (ETM+) and Landsat 8's Operational Land Imager (OLI). Data collected and modelled at this scale results in a 'many trees per pixel' case, where multiple trees are viewed by the sensor at all times, and correspondingly, the pixel's signal is primarily driven by the proportions of sunlit and shadowed canopy and background existing within the area being simulated by GOMS or measured via optical equipment.

The design of the physical model forest was a complex process involving considerations related to the goniometer system, the optical system, and the illumination system. The size and quantity of the trees was largely dictated by the optical system's sensor FOV size and shape, as well as the size of the goniometric hemisphere (which dictates sensor height above the target). In order to meet the 'many trees per pixel' requirement, the smallest and largest possible FOV sizes were measured, as described later in the chapter, and used to determine the amount of area the forest was required to

cover. This area was used to determine the size and number of trees required to provide 20%, 40%, and 60% ground cover, viewed at nadir.

A total of 450 model trees were developed for implementation within the forest plot area. The spatial size of the forest plot was designed to extend beyond the spectrogoniometer footprint area sufficiently to avoid adjacency effects, which refers to the effect of the area surrounding the viewed location has upon the sampled signal. Table 3.3 shows information related to the number of trees used for each separate ground cover dataset.

Table 3.3: Viewed forest ground cover density at nadir.

Model Forest Dataset	Number of Trees	Forest Plot Radius (cm)	Total Forest Plot Area (cm^2)	Crown Closure At NADIR (cm^2)	Crown Closure at NADIR (%)
Low Closure	150	55	9505	1901	20
Intermediate Closure	300	55	9505	3802	40
High Closure	450	55	9505	5703	60

3.3.1.2 Model Trees

In the previously mentioned study by Soffer (1995), a physical forest simulation was implemented in a laboratory model validation experiment; however, the modelled trees were designed to mimic real trees as closely as possible in order to investigate the effects of BRDF in the context of a true forest canopy. Contrastingly, the primary goal in development of the physical model forest in this study was to create a canopy that, as closely as possible, matches the mathematical and geometric assumptions described by X. Li and Strahler (1992) in order to perform computational model validation upon GOMS. The first task was to simulate the model's representation of the individual discrete canopy components as 'spheroids-on-sticks'. However, it should be noted that GOMS has never been strictly applied to the case of spheroidal tree crowns, even from its inception (Li &

Strahler, 1992). Therefore, the shapes of the constructed trees were designed to not conform to the strictly spheroidal case, and were rather created in the form of ellipsoids of various sizes. For this reason, the more geometrically accurate term 'ellipsoids-on-sticks' will be used to describe the nature of this simulation in place of the term 'spheroids-on-sticks'.

Polystyrene was selected as a base material for the trees due to its easy workability, low weight, and low cost compared to other materials considered. The polystyrene was carefully hand-shaped to create a collection of 450 ellipsoids with varying degrees of eccentricity. While future studies may implement situations in which the geometric variables of the trees can be fine-tuned and adjusted to identify GOMS' ability to simulate effects caused by subtle variations in canopy structure, this type of analysis is outside the scope of this thesis. The next consideration in the model tree design was the implementation of the so-called 'sticks', which are analogous to tree stems. The 'sticks' described in the GOMS model do not have any actual physical size, and do not cast shadows. This is, of course, an impossibility to recreate in a physical forest simulation, so thin metal rods were selected to represent the tree stems, primarily due to their nature of being nearly perfectly straight, as well as their high level of rigidity, and their small footprint.

The GOMS model assumes that the modelled trees will be opaque and will have Lambertian reflectance properties, with spectral characteristics that allow for sufficient differentiation between the tree material and the background material. While the use of near-perfectly Lambertian surfaces for building this type of physical forest simulation is not realistically feasible, a cellulose-based flocking material was selected as an outer coating to the simulated trees due to its relatively diffuse reflectance characteristics, while

also having the advantage of having a spectral signature similar to that of vegetation. While care was taken to apply multiple layers of the flocking material to each tree, an underlying layer of green latex paint necessary to affix the flocking material can be considered to account for a small amount of the overall reflectance of each tree. Table 3.4 shows a list of the materials used in construction of the materials utilized in this study.

Table 3.4 : Simulated GOMS physical model forest construction materials.

Construction Material	Application	Additional Notes
Durofoam™ Polystyrene Panel	Model Forest base Structure	Panel Thickness: 1/2"
Brown Felt Material	Model background material	N/A
Floracraft™ Polystyrene Shapes	Model tree base structures	N/A
CIL™ Latex Acrylic Paint	Protective layer for polystyrene	Colour: Forest Green
Woodland Scenics™ Blended Turf	Model tree flocking to diffuse reflectance	Colour: Green Blend
Elmer's™ Spray Adhesive	Adhesion of Woodland Scenics™ turf	Transparent
PowerWeld™ Stainless Steel Wire	Model tree stems	Diameter: 1/16"

In the GOMS model, the tree heights in a given forest are assumed to be randomly distributed between the top and bottom bounds of the forest height distribution. Randomness of tree heights was achieved through the coupling of randomly-designed trees with stems inserted an arbitrary amount into the tree, and the depth at which each tree should be planted marked at an arbitrary location on the stem. Based upon an established heuristic, the goniometer's focus point was positioned at 1/3 the height of the canopy (Coburn & Noble, 2016).

Another design parameter to be taken into account in the vertical domain in the physical forest simulation's design was the constraint that the vertical axis length of the largest ellipsoid must not exceed 4 times the vertical axis radius of the smallest ellipsoid, the rationale for which is described in section 3.2. With the aforementioned parameters accounted for, the issue of scale can be addressed

This physical model forest has not been designed to strictly model a particular forest canopy, or indeed a true tree canopy at all; the focus of this thesis is to perform a straightforward validation of the model assumptions themselves. Therefore, as long as none of the previously stated constraints are met, GOMS should be capable of simulating the bidirectional reflectance and structural parameters of any modelled forest. However, it may be conceptually helpful compare this model forest to a real forest. The trees at the BOREAS SSA OJP site have been measured to average 13.7 m in height. The average height of the model trees in this forest is 9cm, resulting in an effective scale factor of 1:152. With these considerations taken into account, the simulated trees were able to be finalized and inventoried. The structural details were collected in order to reduce the uncertainty in the MFM inversion process (Li et al., 1998). The inventoried values for each tree included the vertical crown radius, the horizontal crown radius, and the stick height between the bottom of the tree canopy and the background material. The measured structural values for the 20% canopy cover, 40% canopy cover, and 60% canopy cover forests can be seen in Table 3.5, Table 3.6, and Table 3.7, respectively.

Table 3.5 : 20% Crown closure Forest Model Forest Statistics

	Stick Height (mm)	Vertical Canopy Radius (mm)	Horizontal Canopy Radius (mm)	Tree Height (mm)	Height to Canopy Centre (mm)
Maximum	55	32.5	23.5	110	82.5
Minimum	6	17.5	11.5	44	25
Mean	31	29.4	19.8	89.9	60.5
Standard Dev.	13.3	2.6	3.3	15.7	14.4

Table 3.6: 40% Crown closure Forest Model Forest Statistics

	Stick Height (mm)	Vertical Canopy Radius (mm)	Horizontal Canopy Radius (mm)	Tree Height (mm)	Height to Canopy Centre (mm)
Maximum	55	32.5	31.5	111	82.5
Minimum	6	17.5	9.5	41	23.5
Mean	30.5	29.1	19.7	88.8	59.7
Standard Dev.	12.3	3.2	3.8	16.2	14

Table 3.7: 60% Crown closure Forest Model Forest Statistics

	Stick Height (mm)	Vertical Canopy Radius (mm)	Horizontal Canopy Radius (mm)	Tree Height (mm)	Height to Canopy Centre (mm)
Maximum	55	33	31.5	111	82.5
Minimum	6	17.5	9.5	41	23.5
Mean	30.3	29.4	19.7	89.2	59.8
Standard Dev.	12.2	3	4	15.4	13.6

3.3.1.3 Model Background

Typical Boreal forest understories are highly heterogeneous in nature, consisting primarily of varying amounts of live and dead vegetative materials, as well as varying amounts of soil and rock (Hall et al., 1997). Seasonality also plays a large factor in the forest background, as snow can dramatically change the spectral reflectance properties of a background. However, the GOMS model only makes two major assumptions for an background: that the modelled background has a single, Lambertian characteristic reflectance signature that allows it to be differentiated from the canopy material, and that the background is a flat surface (Li & Strahler, 1992).

While this model forest features a level, flat background, the GOMS model is capable of being used in areas of high relief, such as mountainous areas. While this could be easily implemented in this simulated forest by simply positioning the base at an angle and bending the tree stems at an angle wherein the trees would simulate the process of

growing perpendicular to the Earth's geoid, this is outside the scope of this study; therefore the background was designed with a 0° slope.

In the same manner that the specific colour of the model trees' flocking material was selected to add a degree of realism to the model forest, a digitized photograph of the boreal forest understory at the BOREAS SSA OJP site were studied in order to determine the most suitable available coloured material to accomplish the same task. The understory is dominated by plant litter and various types of mosses and lichens, with a yellow-brown colour dominating the landscape of the understory. In order to visually assess the average overall colour of the scene, a low-pass filter with a kernel size of 32 was applied to a sunlit subset of this photo in ENVI. A felt material coloured similarly to the output of the filtering process was selected as the simulated forest's background material. Felt material was selected due to its expected diffuse reflectance properties. Figure 3.2 shows the OJP site image, as well as the filtered image and selected material.

The background material was affixed to a 1.2m x 1.2m sheet of polystyrene insulation material 1/2" in thickness, which was selected as a backing material upon which the forest model could be built. Two layers of background material were used in the simulated forest in order to block out any possible signal from the underlying backing material.

Figure 3.2: Photograph showing typical boreal forest understory components, primarily tree litter and various lichens (A). A subset of a sunlit portion of the photo (marked with a red border) was selected and a low pass filter was applied (B). A sample of the selected model background material is shown in (C). (Photo courtesy of ORNL DAAC, 1999)

3.4 Canopy Stem Map Generation and Canopy Model Implementation

3.4.1 Stem Map Generation

The spatial distribution of the individual trees in the x,y plane in the GOMS model is assumed to be random, the nature of which is fundamental to the application of Boolean models (Strahler & Jupp, 1990). This type of distribution is a valid assumption for tree distribution in natural forest settings, provided that a sufficient number of trees exist within the pixel area (Franklin et al., 1985). However, classical random distributions, such as the Poisson distribution, were found to suffer from one insurmountable drawback in regard to use in the design of this laboratory experiment; the solid, simple geometric nature of the model trees dictates that no two tree canopies can overlap. As a result, the center x,y locations of any pair of trees cannot be closer to one another than the sum of the *r* values for those two trees.

An ideal solution was identified in the Fast Poisson-Disc (FPD) Sampling Algorithm (Bridson, 2007). The FPD algorithm is able to create a random point distribution with a user-defined minimum distance between points, as well as allowing a user-defined maximum distance between existing points and newly created points. The model's implementation of distance-specifying annuli created about each point provides the basis for an ideal distribution for this application, wherein the randomly distributed

points can be tightly packed together while also maintaining the spacing required for successful implementation with this physical forest simulation. The FPD algorithm was implemented in a manner that allowed for generation of a stem map on a circular background grid in keeping with the circular nature of the ULGS-2's total FOV footprint, avoiding the generation of unnecessary corner points, the removal of which could affect the characteristics of the distribution. Following creation of the plot map, using a random number generator, each point was assigned a number belonging to a corresponding physical model tree.

3.4.2 Canopy Model Implementation

In order for the random nature of the trees' locations to hold true in the physical model, it was important to precisely position each tree upon the background panel. This was accomplished by first importing the X,Y coordinates of the points in the FPD-produced stem map into ArcMap and plotting the distribution in two-dimensional Cartesian space. The point distribution was printed onto a sheet of clear acetate and placed onto an overhead projector, and the projection was focused and centered on the background panel. This facilitated placement of the model trees in the correct locations in the background with minimal effort and maximum accuracy. While the exact distances specified when running the FPD algorithm do not hold true when the distribution is enlarged via projection, the random nature of the distribution does, and its ability to avoid close point proximity was found to allow for successful implementation of the simulated forest. Figure 3.3 shows the development of the model forest using this method.

Figure 3.3: Computer-generated stem map projected onto model forest plot area.

Although the values of the canopy structural variables were distributed randomly in keeping with the GOMS model's assumptions, the selection of the trees included in each distribution was such that the average horizontal canopy radii for the individual trees was kept constant for each of the three forest densities. This was done to allow for the ability to remove or add an equal number of trees each time the crown closure of the forest was adjusted, simplifying design and maintaining consistency.

The forest distribution with 20% crown closure coverage at nadir consisted of 150 trees, with the 40% and 60% crown closure forest distributions containing 300 and 450 trees, respectively. Spectrodirectional measurements of the simulated forests were collected in increasing order of crown closure in order to avoid damage to the background material, which could have the potential to affect the resultant spectral measurements. Figure 3.4 shows the three fully developed forest distributions alongside their respective FPD point distributions.

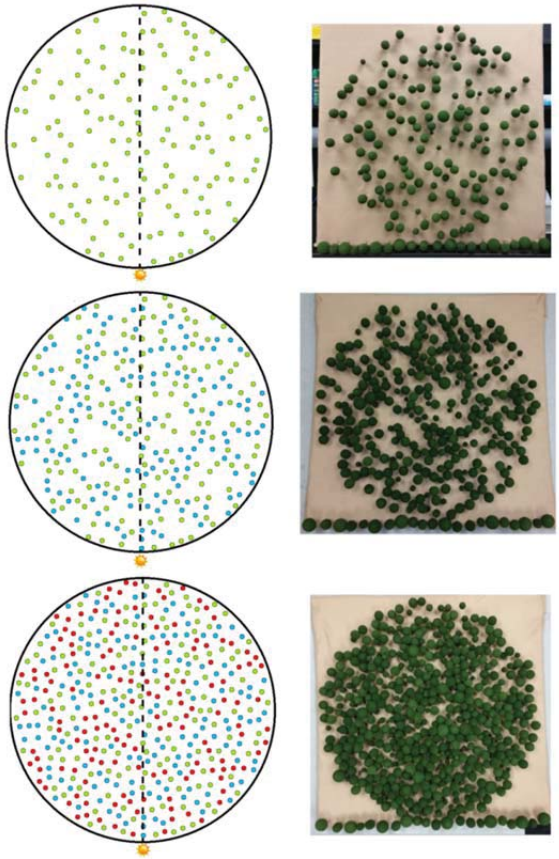

Figure 3.4: Side-by-side comparison of computer-generated Poisson-disc forest distributions (left) and photos of the associated physical forests model canopies (right). The green points in the plot maps represent the trees in the 20% crown closure forest, and the blue and red points represent the trees added for the 40% and 60% crown closure forests, respectively.

One final assumption of the GOMS model which was accounted for in the physical forest model relates to the shadows cast from the trees at the back of the scene. GOMS assumes the shadows cast behind the scene in the forward-scatter direction are projected onto the trees located in the backscatter direction in order to assure mutual shadowing occurs evenly across the canopy. In order to account for this, an extra section of model trees were developed and put into a distribution matching those in the location furthest away from the light source, and were positioned in a location where they could cast shadows onto the trees nearest the light source. An implementation of this method

can be seen in Figure 3.5, where the forest with 60% canopy coverage is being illuminated at the winter illumination angle.

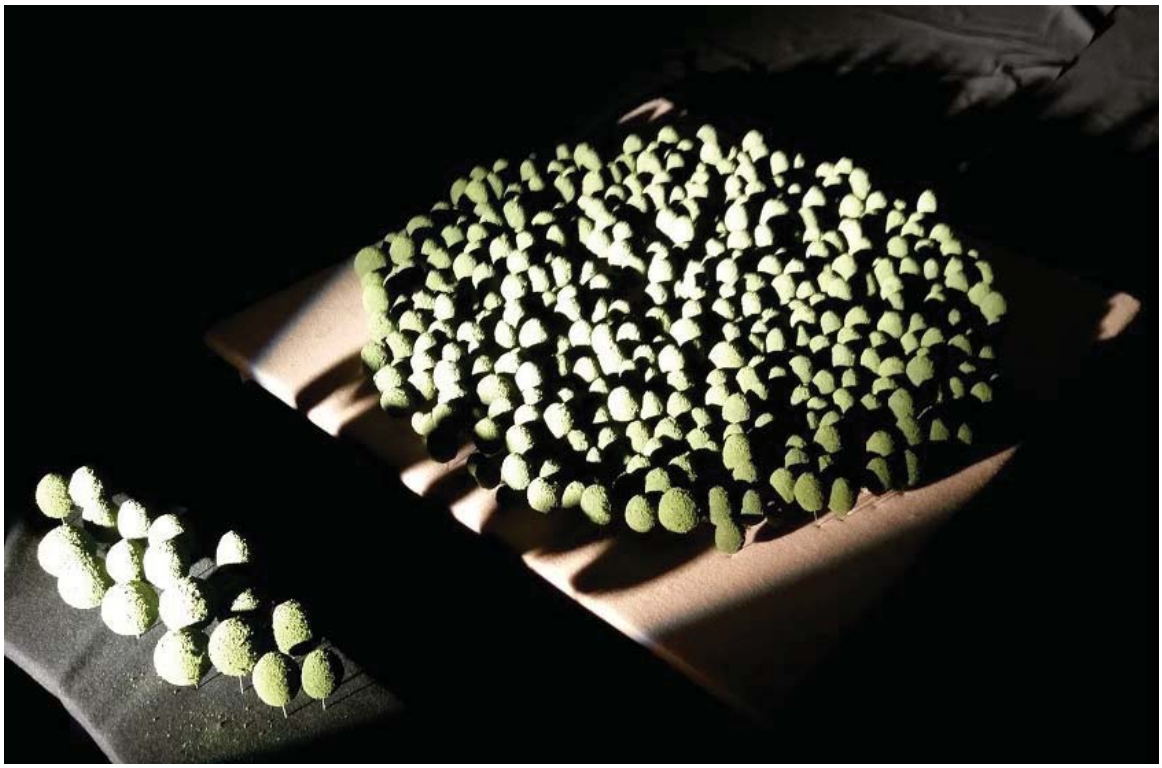

Figure 3.5: Fully constructed 60% crown closure physical model forest of spheroids-on-sticks viewed at an oblique angle.

3.5 Endmember Target Panels

Model validation exercises performed on actual forest canopies benefit from the inclusion of the effects of multiple scattering, canopy gaps, and canopy light transmittance in the measurement of shadowed component signatures, which are the primary driving factors behind the "darkness" of a canopy's shadow (Abuelgasim & Strahler, 1994; Sandmeier et al., 1998). However, realistically, these effects are present in varying degrees in the shadows cast by any individual tree, which inherently lends a degree of uncertainty to the quality of the component signatures used in the model validation process. The opaque nature of the model tree crowns utilized in this experiment minimize these effects, which has the desirable consequence of the trees casting shadows

which would be expected to have little variation in reflectance, both over the area of a single shadow and between the shadows cast by different trees. Therefore, an opaque shadowing agent was created in order to collect the shadow endmember component signatures. However, a certain degree of diffuse illumination is present in the shadows cast within the model forest, so the illumination source could not be blocked completely. Therefore, the shadowing agent was positioned in a manner where the area sensed by the FOV was completely shadowed from the primary illumination source, but the light was still allowed to cast some light onto the edges of the target.

In order to properly understand the reflectance properties of the canopy and background materials, as well as to reduce the uncertainty in the MFM inversion process, it was necessary to sample a full HCRF dataset using the ULGS-2 for both materials (Li et al., 1998). In order to facilitate this requirement, two endmember target panels were developed. The background endmember panel consisted of two layers of the background felt material, and the canopy endmember panel consisted of a flat panel painted with several layers of green latex paint, and covered with an amount of green flocking material comparable to that on the model trees. Much like the area of the forest distribution itself, the area covered by these endmember panel targets were required to be substantially larger than the maximum width of the FOV at its maximum size in order to avoid issues related to adjacency effects. In order to meet this requirement, square panels the same size as the simulated forest base were developed to be used as targets for endmember data collection. The sunlit and shadowed canopy endmember target panels can be seen in Figure 3.6.

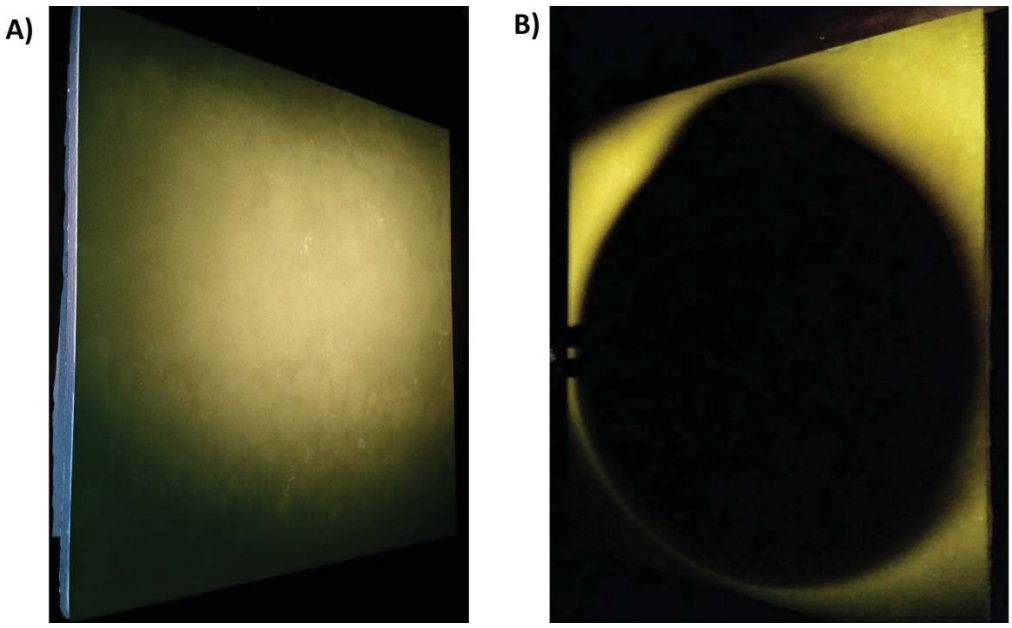

Figure 3.6: Canopy endmember target panel with unhindered illumination (A) and with shadow incorporated using a circular shadowing agent (B), illuminated from left. Note that 'bulges' in the shadow are an effect of light diffraction due to proximity of the goniometer arm to the shadowing agent.

3.6 Illumination System

An Altman Shakespeare™ ellipsoidal reflector spotlight fitted with a 750 W bulb was deemed to be a sufficient primary light source for this laboratory experiment under the following bases. First, the ellipsoidal reflector within the spotlight housing provides a degree of collimation of the light, which is a desirable trait in laboratory BRDF experiments (Sandmeier & Strahler, 2000). Second, this spotlight has the ability to allow the researcher to adjust the size and focus of the spotlight beam, which is an ideal characteristic in order to optimize the beam width to collect reflectance measurements which avoid adjacency effects caused by the sensor observing an area close to the edge of the illumination beam.

A light stability test was undertaken before measurements were collected. The spotlight was allowed to run for 30 minutes to thermally stabilize, and repeated measurements of a Spectralon™ panel were collected over the course of ten minutes

without adjusting the illumination or sensor positions. The measured spectra varied substantially, an effect determined to be caused by instability of the AC line power. Subsequently, the illumination source was powered using a stabilized power source consisting of a large lead-acid battery and a 3000 W MotoMaster™ Eliminator power inverter to mitigate the effects of illumination drift caused by electrical fluctuations.

3.7 Laboratory Stray Light Optimization

Due to highly reflective properties of the model forest materials as well as the instruments and objects within the lab itself, significant directionality in the hemispherical component of the illumination in the lab was identified. To reduce the directionality of this ambient hemispherical light a secondary, indirect, diffuse illumination source was also implemented by pointing a halogen light at a black wall directly in alignment with the SPP on the side of the plot opposite the primary light source. Additionally, temporarily deployable walls approximately 2.5 meters in height were constructed using black poster board material and black electrical tape in order to absorb as much stray light as possible in the laboratory area. As an added measure, black felt material was used to cover the floors and was placed in all locations which were directly illuminated by the spotlight beam outside of the model forest's plot area in order to diffuse and absorb stray light. The implementation of these measures can be seen in the laboratory photograph in Figure 2.3.In addition to the aforementioned measures, any sources of illumination such as LED lights on equipment in the lab or stray outdoor illumination leaking into the lab in the doorway were covered with black, lightproof material.

3.8 Spectrogoniometric System and HCRF Sampling

A number of instruments were utilized over the course of this laboratory data collection campaign. An overview of the instruments utilized in the process of HCRF sampling, along with a brief description of their application, is provided in Table 3.8.

Table 3.8: Instruments used in laboratory data collection.

Instrument	Application
ULGS-2 Goniometer	Sensor Positioning
Ocean Optics™ USB-4000 UW Spectrometer	Model spectral radiance measurements
Spectralon™ PTFE panel	Reflectance processing
Altman ellipsoidal reflector spotlight	Primary Direct Illumination source
Halogen light with frosted glass window	Secondary Diffuse Illumination source
Panasonic CF-30 Toughbook	Goniometer and Spectrometer Operation
Samsung Galaxy S5 16 megapixel camera	Laboratory and target photos

Due to the impossibility of directly measuring the BRDF, it instead must be approximated through the collection of sampled HCRF measurements at various angular locations distributed over the surface of a hemisphere (Barnsley et al., 1994). It is upon this basis that laboratory HCRF measurement campaigns are based. The angular resolution of the data points sampled by the ULGS-2 and its onboard UW USB-4000 spectrometer in this data collection campaign was selected upon the basis of the recommendations provided by Coburn and Nobel (2016), who suggested that an angular sampling resolution of 10° in the azimuth-zenith domains be utilized. With this angular sampling resolution, HCRF data was sampled every 10° in both the azimuth and zenith directions. The angles at which HCRF measurements were collected range from 0° - 60° in the zenith angle direction, and from 10° - 350° in the azimuth angle direction. The ULGS-2's arc cast a shadow upon the target at the azimuth angle corresponding with the SPP, therefore spectrodirectional measurements were only able to be sampled at 35 azimuth angles.

While the inability to sample HCRFs in the location of the SPP causes some limitations in data analysis, the required beam width for proper illumination of the simulated forest was such that it was deemed impossible for this data to be sampled with the available equipment. The exclusion of these six data points resulted in the sampling of HCRF data at 211 locations in the goniometric hemisphere: six VZA data points, each collected at 35 different VAAs, plus the measurement collected at nadir. A measurement was sampled at nadir each time the quarter arc changed its azimuth angle, and the subsequent 35 nadir measurements were averaged in order to derive a single representative nadir measurement for each dataset.

The use of a 10° angular sampling resolution was a primary consideration in selecting the 8° FOV foreoptic/barrel used with the USB-4000. The implementation of an FOV smaller than the angular sampling resolution is useful in avoiding oversampling effects between HCRF measurements, therefore a set if optics constraining the USB-4000's FOV to 8° was implemented.

3.8.1 Sensor Field-Of-View

In a goniometer system, the FOV area and location is determined not only by the constraints applied to the FOV via the use of constraining optics, but also by the geometry of the sensor in relation to the viewed target. When viewed at nadir, the FOV is circular. When a goniometer positions the sensor at an off-nadir look angle, the FOV becomes an ellipse which increases in size as the view angle moves further off-nadir. Figure 3.7 displays the geometric considerations taken into account with off-nadir RS when a sensor's FOV has been constrained to view a circular area with defined view angle.

One important distinction made in figure 3.7 is that of the center of the FOV, and the center of the FOV footprint. The center of the FOV refers to the location in the FOV

that corresponds to the focal point of the goniometer, which does not change location with a center-focused goniometer such as the ULGS-2 ; while the center of the FOV footprint refers to the geometric center point of the FOV as it is projected onto the target at the goniometer 's focal plane.

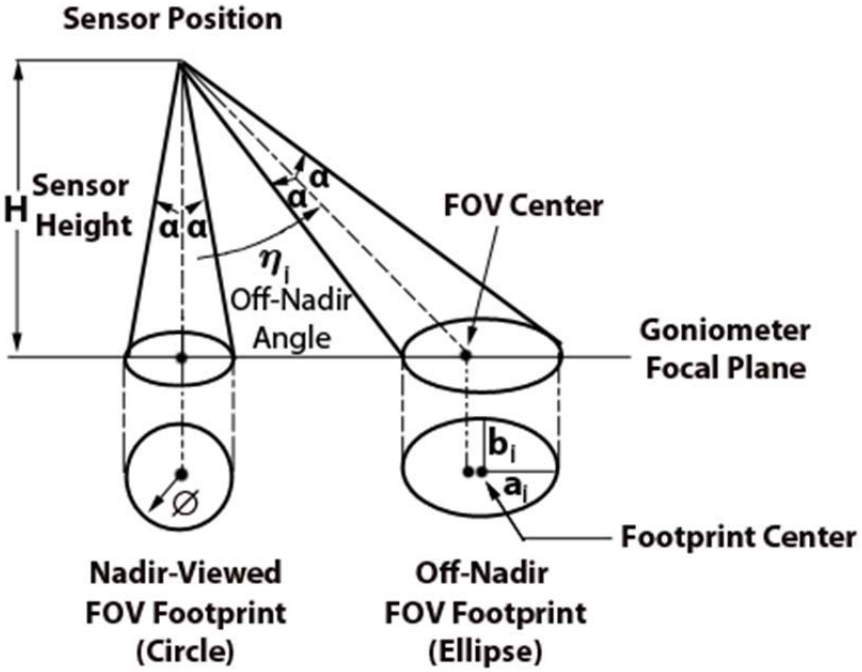

Figure 3.7: Sensor field-of-view geometry at nadir and off-nadir angles (Adapted from Deering, 1986).

When a sensor is positioned viewing a target at nadir, the radius of the FOV, $\varnothing$, is given by

$$\varnothing = H \frac{tan((2\alpha)\pi/180)}{2} \tag{3.1}$$

where H = the height of the sensor above the goniometer focal plane, and α is 1/2 of the FOV angle. The area of the FOV footprint A_i. can then be calculated by

$$A_i = \pi\varnothing^2. \tag{3.2}$$

At off-nadir viewing angles η_i where $\eta_i < \pi/2 - \boldsymbol{\alpha}$, the sensor FOV will be an ellipse whose major axis a_i is calculated as

$$a_i = \frac{H\ tan\ \alpha(1 + tan^2\eta_i)}{1 - (tan\ \alpha\ tan\ \eta_i)} \tag{3.3}$$

and whose minor axis b_i is calculated as

$$b_i = \frac{H\ tan\ \alpha}{cos\ \eta_i[1 - (tan\ \alpha\ tan\ {\eta_i}^2)^{1/2}}. \tag{3.4}$$

With the major and minor axes calculated, the area A_i of the elliptic sensor FOV footprint can be calculated as

$$A_i = \pi a_i b_i. \tag{3.5}$$

While these parameters can be calculated directly, it is a helpful practice to physically measure the size and location of the FOV in order to confirm the results of these calculations in the operational setup. Measurement of the size and shape of the FOV was accomplished by placing a flat, white surface target larger than the expected size of the FOVs at the two necessary locations, and the tangents of the FOV were located using rectangular black foam material with very low reflectance. The foam was slowly moved toward the expected FOV location, and when it entered the FOV, a lowering of reflectance was subsequently seen on the computer using SpectraSuite™ software. This process of locating tangents of the FOV was repeated using several pieces of foam until the size and shape of the FOV was able to be determined. Figure 3.8 shows the nadir footprint, with a representation of the size and shape of the measured 30° and 60° VZA FOV footprints as compared to that measured viewed at nadir.

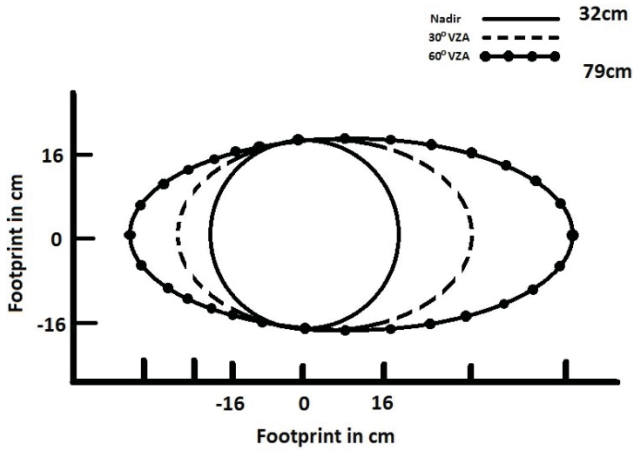

Figure 3.8: Measured sensor FOV at various VZA.

3.8.2 White Reference and Dark Current Measurement

The process of periodically collecting white reference (WR) measurements to monitor illumination variability is an important practice in field studies where Sun-sensor geometry and atmospheric conditions are in constant flux. However, the target proximity and stationary nature of the illumination source in laboratory-based experiments negate these issues. Therefore, provided the illumination source is sufficiently stable, a single white reference value can be used for all measurements in laboratory spectrodirectional RS data collection campaigns. As the illumination source was powered by a stable battery power source, a single nadir-looking Spectralon™ WR measurement was utilized for reflectance processing of all datasets.

In laboratory goniometer data collection campaigns, it is important that WR measurements be indicative of the irradiance incident at the goniometer system's focal point. Therefore, in the mission planning stages, it is important to ensure that the sensor FOV footprint at the focal point is small enough to fall within the bounds of the WR panel in order to avoid adjacency effects. As the selected optical configuration in conjunction with the ULGS-II resulted in an FOV larger than the available Spectralon™

panel, a method was devised in order to collect valid WR measurements which avoid these adjacency effects.

This method is a two-step process. First, the white reference panel is moved vertically upward from the focal point a sufficient distance to allow the sensor FOV to fall completely within the Spectralon™ panel area. While the distance from the sensor optics to the WR panel target can be used to calculate the FOV size to accomplish this, it's suggested that after the WR panel is placed, the FOV tangents be located by viewing spectra in real-time using SpectraSuite™ and observing where spectra changes based on moving dark material toward nadir from the edges of the WR panel. If dark material can be placed over all edges of the WR panel surface without causing a drop in spectra, the FOV can be considered to be fully within the WR panel boundaries.

Second, the illumination source must be moved to a location in relation to the raised WR panel location where the irradiance incident upon the panel is identical to that which would be incident upon it at the goniometer's focal point. The illumination source, located at the simulated winter solstice solar angle, was able to have its height linearly increased along with the Spectralon™ panel. This rendered the illumination-target geometry, and subsequently the irradiance incident on the panel, unchanged.

However, the illumination source at the simulated summer solstice solar angle was not able to linear height increase due to spatial constraints in the laboratory area. Therefore, in order to place the illumination source at a location which provides an equal amount of irradiance at the new location of the target as would be incident at the goniometer's focal point, a new illumination location where the light could physically be positioned while providing the panel with an amount of incident irradiance equal to that at

the focal point was selected through the use of a combination of the inverse square law and Lambert's cosine law.

The inverse square law describes how the amount of irradiance incident on a surface responds as distance between the illumination source and target change, and is represented by

$$I_{surface} = \frac{I_{beam}}{R^2} \ [sr^{-1}] \tag{3.6}$$

where $I_{surface}$ represents the amount of irradiance incident upon a point on the target surface, I_{beam} refers to the amount if irradiance provided by the laboratory light source with dispersion, and R represents the linear distance between the illumination source and a point on the target's surface (Mahajan, 2014). Lambert's cosine law describes how the irradiance incident upon a point on a surface varies as the angle of illumination increases from an angle perpendicular to surface normal, which is equal to the SZA. It is represented by

$$I_{surface} = I_{beam} \times \cos(\theta) \ [sr^{-1}] \tag{3.7}$$

which allows the proportion of the source's total irradiance which is incident at a location on the target surface to be calculated. where θ refers to the SZA. These two concepts are combined in the following equation

$$I_{Surface} = \frac{I_{beam} \times cos(\theta)}{R^2} [sr^{-1}] \tag{3.8}$$

which allows the proportion of the source's total irradiance incident at a location on the

target surface based on the illumination zenith angle and distance of the illumination source to the target to be calculated. This equation was utilized to determine an illumination location which had a sufficiently high angle value and low R value to provide the required irradiance level while also allowing the light source to be positioned within the confines of the lab area.

Dark correction refers to the process of removing sensor electronic noise from the signal by collecting a measurement when no light is reaching the sensor, and subsequently subtracting these dark current values from all other measurements before further processing. The USB-4000 computer processing software is capable of performing an electric dark correction wherein dark current is measured for a single blacked-out sensor component which is used to correct for dark current across every wavelength over the sensor. However, this is considered to only be a first-order correction as it does not take into account variation in dark current at separate wavelengths. In order to properly account for dark current, measurements were collected directly by placing a heavy piece of black plastic over the optics of the sensor, blocking all light from entering the spectrometer, and collecting a spectral measurement. The dark current measurements collected were subtracted from the measured radiance values on a wavelength-by-wavelength basis prior to reflectance measurements being derived.

3.9 Endmember Measurements

Measurement of a spectrally pure endmember is not possible in reality due to the highly variable nature of the spectral reflectance of any given surface type, but if care is taken, a spectral signature that is highly representative of the spectral properties of a sample can be acquired. Integrating spheres are often utilized to collect endmember data

due to the advantageous property of providing spectral without the influence of illumination-target-sensor geometry. However, in order to fully understand the reflectance properties of the materials used in designing a physical model, it is helpful to obtain a full BRDF for each endmember. This was accomplished by using the ULGS-2 to collect a full set of 211 HCRF samples for both the sunlit canopy and sunlit background endmembers. Shadowed endmember measurements required the implementation of a shadowing agent. A black disc of a sufficient size to partially, but not fully, occlude the spotlight were connected to tripod and placed between the illumination source and endmember panel. Partial occlusion of the light where the edges of the panel were illuminated was important in collecting the shadow endmember spectra; shadowed areas do have some incident irradiance due to light scattering, therefore fully blocking the illumination source would not provide a signal representative true shadow. The shadowing agent had to be located within the goniometric hemisphere, and as a consequence, shadow endmember data could only be collected at nadir. Because shadow spectra was only collected at nadir, the FOV remained constant in the center of the panel, and adjacency effects from the illuminated portion of the panel did not need to be considered.

3.10 Data Preprocessing

Healthy vegetation has unique spectral properties that enable it to be easily distinguished from other land cover types in the visual and near infrared sections of the electromagnetic spectrum (Gates et al., 1965). While the materials utilized in this study are non-vegetative, the cellulose-based flocking has reflectance characteristics similar to that of vegetation; therefore, the selected wavelengths at which the results are ones

normally utilized in diagnostic vegetative studies, providing a link to existing modelling validation results. The observed spectral signatures of the endmember materials as viewed from nadir are shown in Figure 3.9.

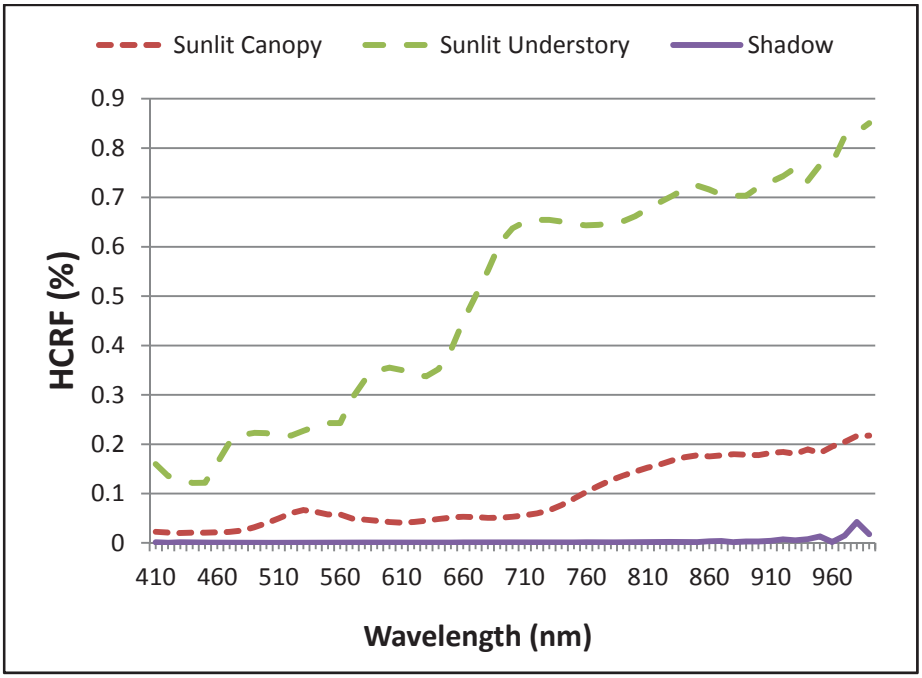

Figure 3.9: Spectral signatures of the three model forest components as viewed from nadir.

The 550 nm, 670 nm, and 800 nm wavelengths were selected for sampling, and are located at the locations in the EM spectrum where the green peak, red minima, and near-infrared vegetative diagnostic features exist, respectively (Gates et al., 1965). The spectral resolution of the data collected with the USB4000 was downsampled to 10 nm due to limitations with the sensor accuracy at very high spectral resolution. Reflectance processing was performed as in Equation 1.1, with a Spectralon™ white reference measurement used to derive reflectance values. An overview of software used in data processing is found in Table 3.9.

Table 3.9: Software utilized in data processing.

Software	Application
Goniometer Control Software	Control of goniometer arc and sled movement
ArcGIS 10.2.2	HCRF plot generation
Microsoft Excel 2010	Data processing
ENVI 5.0	Endmember abundance validation
Windows Powershell	Batch file type conversion
Bulk Rename Utility	Batch filename conversion
UFTCast Express	Data encoding
Poisson-Disc Modelling Software	Forest plot map generation
GOMS-MFM Modelling Software	Canopy reflectance modelling

3.11 HCRF Plot Development

In order to effectively visualize an approximation of the BRDF of the physical forest simulation based on the HCRF values sampled using the ULGS-2 in the lab, the data points collected using the USB4000's UW spectrometer were plotted in two-dimensional space and interpolation techniques were utilized to simulate the BRDF surface. This procedure was also applied to the BRF data points modelled using the GOMS software. The initial procedure in development of these BDRF plots is the conversion of the points from a spherical coordinate system to a two-dimensional Cartesian coordinate system. This conversion is accomplished in the X and Y domains using the following two equations, respectively:

$$x = r\ sin\theta\ cos\Phi \tag{3.9}$$

$$y = r\ sin\theta\ sin\Phi \tag{3.10}$$

where r is the ULGS-2's arc radius (2 m), θ is the VZA, and ϕ is the VAA. These Cartesian coordinates, along with the measured or modelled HCRF values, were visualized via surface interpolation in ArcGIS's ArcMap software (version 10.2.2). with the SPP oriented vertically. The plotted values were normalized as a percent difference

with respect to nadir, as described in equation (2.4), in order to allow for visual comparison in the patterns between the interpolated surfaces; similarly, they were also produced using reflectance values in order to investigate patterns within individual surfaces. The spline method of surface interpolation was selected due to its ability to create a surface which runs directly through the measured or modelled data points, reducing the likelihood that surfaced points will be underestimated or overestimated. The Natural Breaks variation of the Jenks Classification method was utilized in classification of the interpolated surface values due to its usefulness in generalizing data while also allowing retention of the significant surface characteristics (Jenks & Coulson, 1963). Figure 3.10 shows a schematic of a HCRF plot.

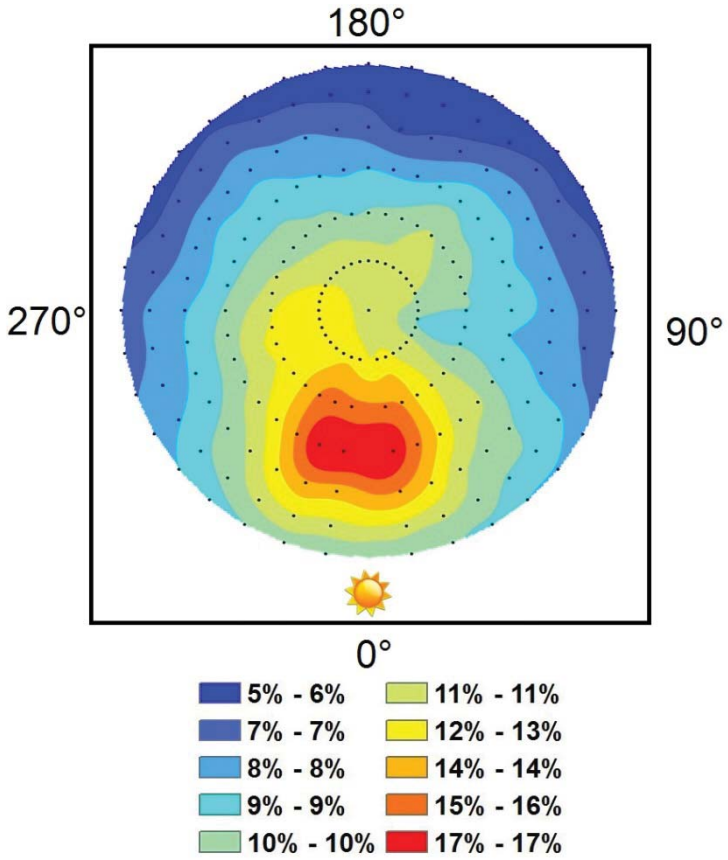

Figure 3.10 : Schematic of a HCRF plot in two-dimensional Cartesian space, with the SPP oriented vertically. Data is for a modelled forest with 60% crown closure dataset sampled at 10° angular sampling resolution using the ULGS-2. The unavailable data points in the backscatter direction of the SPP due to shadowing of the target by the goniometer arc are omitted. The direction of illumination is marked with a Sun icon.

3.12 Target Rotational Variance Assessment

A test was performed in order to identify if the major drivers causing the patterns of the derived HCRF plots of the simulated forests are rotationally variant. To accomplish this task, a full-hemisphere ULGS-2 dataset was collected for the 20% crown closure simulated forest panel, and immediately following this task, the panel was rotated 90° clockwise about nadir while all other laboratory conditions were maintained, and a second full-hemisphere dataset was collected with the ULGS-2. The plots were processed using the same procedure in order to allow direct comparison between the two.

3.13 Implementation of GOMS Forward-mode and MFM Inversion

Following the successful collection of the required spectra, GOMS modelling software was utilized in forward-mode in order to model reflectance values at the same 211 angles at which the physical model forest spectra was collected. The inputs used by the version of threesomes software used in this thesis to model reflectance in forward mode are illustrated in Table 3.10.

Table 3.10: GOMS Model Forward-Mode Inputs

Structural	Optical (Degrees)	Spectral (BRF)
Tree density (per m^2)	Viewing Azimuth	Sunlit Canopy
Horizontal Crown Radius (m)	Viewing Zenith	Sunlit Background
Vertical Crown Radius (m)	Illumination Azimuth	Shadow
Height to Crown Center (m)	Illumination Zenith	
Height of Stick (m)		

Multiple-Forward-Mode (MFM) model inversion is capable of deriving structural information from canopy reflectance models that cannot be feasibly inverted by traditional means due to their complexity (Peddle et al., 2003). The MFM technique, when applied to the GOMS model, allows the user to provide ranges for the structural, optical, and spectral inputs found in Table 3.10 rather than the exact values normally required for model inversion. The MFM technique then runs the GOMS model multiple times, performing one forward-mode model run for every possible combination of inputs within the input ranges, with the number of iterations run constrained by user-specified step sizes. MFM has proven itself useful for retrieving structural information about forest stands even in cases where no a priori information about the scene is provided, using a technique referred to as MFM Full Blind Mode (FBM) (Peddle et al., 2010). However, because a priori structural information for the simulated forest is known, a constrained set of structural variables were used in MFM processing.

The MFM software outputs a reflectance value for each iteration and stores it in an MFM Look Up Table (LUT), within which measured reflectance value can be searched for and returned to obtain spectral matches. When a single match is obtained, the structural data associated with that reflectance value match can be considered to be the inverted structural output provided by the MFM model inversion. However, issues related to equifinality in the LUT results in the form of multiple exact matches are also a possibility. In the case where multiple matches are encountered and a single, unique solution is required, distribution analyses and summary statistics are utilized in a spatial context (Johnson et al., 2000; Pilger et al., 2002; Peddle et al., 2003; Soenen et al., 2010). In the case where no matches are encountered in the MFM LUT, an algorithm utilizing spectral space proximity thresholding is invoked to generate a result based on the nearest matches.

The structural parameters used to produce the GOMS-MFM LUT are outlined in Table 3.11. The specified minimum and maximum structural values have sufficiently low and high values, respectively, to ensure that the structural ranges extend beyond those found for any given model tree in the physical model forest. The selected increment step sizes were selected to correspond roughly to the precision at which the structural parameters in the physical forest were able to be measured, while also taking into consideration the size of the MFM LUT. While in a true forest scene the structural parameters and increment step sizes would be much larger, these parameters were deemed to be appropriate for use with a model forest of this scale.

Table 3.11: GOMS-MFM modelling inputs

Parameter	Units	Min	Max	Step Size	Number of Steps
Horizontal crown radius	cm	0.1	5	0.7	8
Vertical crown radius	cm	0.1	5	0.7	8
Height to crown center	cm	1	10	0.6	16
Height distribution	cm	5.4	6	0.12	6
Density (λ)	trees /cm^2	0.01	0.08	0.005	15
				Total Steps	92,000

3.14 Measurement Uncertainty Quantification

The number of spectral matches identified during analysis of the MFM-LUT is, in part, dependent upon the number of significant digits implemented in the matching algorithm. In general, a measurement system with a high degree of precision (corresponding to a low degree of measurement uncertainty) allows researchers to define exact spectral matches with a larger number of significant digits than would be possible with a system with low measurement precision. Therefore, it is important to identify the degree of measurement uncertainty with which the spectrometer is capable of collecting spectral measurements in order to reduce the inherent problems related to equifinality as much as possible, while also avoiding the introduction of false precision in the results; a case which occurs when the number of significant digits reported are greater than those able to be measured.

In order to quantify the degree and distribution of measurement error in the USB4000 in the lab, multiple measurements were collected of an identical target under identical conditions over a short period of time, and statistical analysis was subsequently performed on the multiple measurements. Ten total datasets consisting of Spectralon panel measurements illuminated by a stable light source were collected at nadir over the

course of approximately ten minutes. Each measurement was calculated via the average value of ten sampled measurements.

3.15 AMBRALS Forward-Modelling of MODIS BRDF Product

The MODIS BRDF Parameters product's (MCD43A1) was acquired for the pixel corresponding to the BOREAS SSA OJP flux tower location using the APPEEARS tool provided by the NAAC ORDL. The three RTLSR kernel weighting coefficients (f_{iso} , f_{geo}, f_{vol}) provided by this product were used in combination with the AMBRALS modelling framework in order to undertake forward-mode reflectance modelling. A custom software package based on the AMBRALS modelling framework was developed in order to forward-model surface reflectance at the OJP flux tower site for June 21 at solar noon, with reflectance values being sampled at 10 degree angular resolution over the hemisphere in order to match the scan pattern sampled in-lab using the ULGS-2. In order to compare this output from the BRDF product for the same location on multiple years, data from 2001 (the first year available) as well as from 2014 and 2016. These datasets were selected due to the high level of quality (Level 0) indicated by the MODIS data quality indicators provided in the MCD43A1 product.

3.16 PARABOLA-2 *In Situ* BRDF

In order to evaluate the level of agreement between BRDFs derived from laboratory measurements of the simulated forest and field measurements of a true forest canopy, multiangle reflectance spectra acquired with the PARABOLA-2 goniometer *in situ* at the BOREAS SSA OJP flux tower site was obtained from NASA's Oak Ridge National Laboratory Distributed Active Archive Center (ORNL DAAC) (Deering & Eck, 1999). Deployed during the growing season of 1994, the PARABOLA-2 instrument was

mounted on a tram above the OJP forest canopy and sampled HCRF measurements at 15° intervals in the zenith direction and at 30° intervals in the azimuth direction. Cones on the PARABOLA-2 sensor heads confine the FOV to 15°. The dimensions and area of the PARABOLA-2 FOV footprint can be calculated using the methods outlined in section 3.6.1 of this thesis.

This study will focus on data collected via PARABOLA-2 channel 1, which samples reflectance at the 650 nm – 670 nm waveband. The available dataset nearest solar noon with the date closest to the summer solstice was selected, with the time and date of the data collection for the selected dataset being May 31 at 11:09 AM. Figure 3.9 shows the PARABOLA-2 instrument mounted on the tram above the OJP site forest canopy during this data collection campaign.

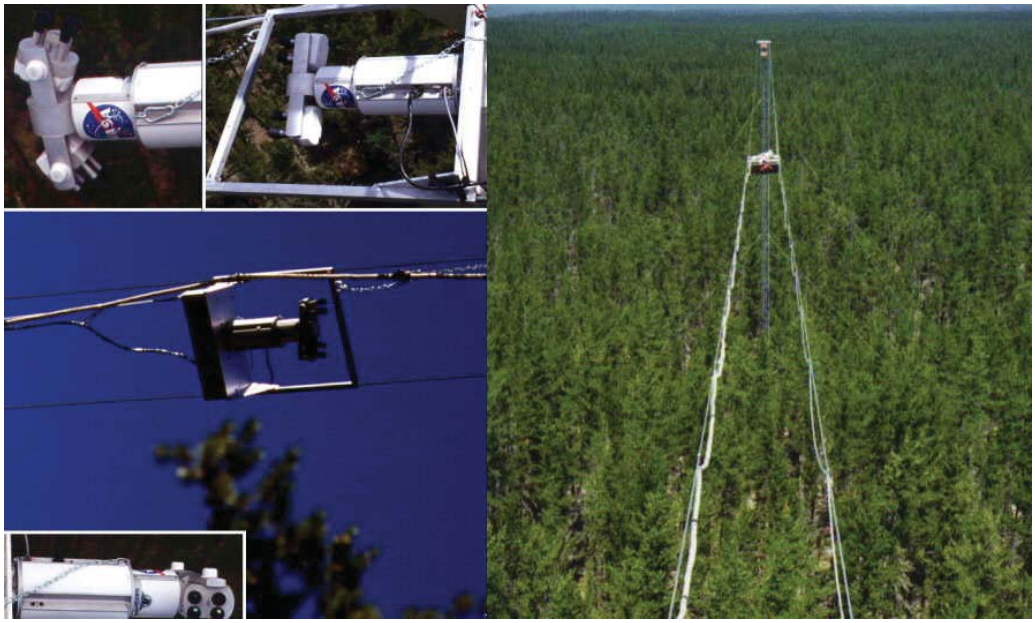

Figure 3.11: The PARABOLA-2 goniometer system mounted upon the tram above the canopy at the BOREAS SSA OJP site (NASA, 1994)

4 RESULTS

This chapter outlines the results obtained from the methods described in the previous section. Evaluation of GOMS' forward-mode simulation of target HCRF values, and its subsequent ability to allow for derivation of BRDF surfaces in the form of interpolated HCRF plots, was performed through statistical error analysis and visual interpretation. This procedure was performed on reflectance values and anisotropy factor values in order to evaluate both intra- and inter-plot variation patterns of the BRDFs. Similarly, HCRF values collected in a single plane near the location of the SPP were plotted and evaluated as a function of zenith viewing angle,

MFM model inversion upon spectra collected at the nadir position was performed for each forest dataset at both illumination angles and all three wavebands. Statistical analysis utilizing the absolute differences between measured forest structure and GOMS' structural outputs were implemented in order to evaluate the accuracy of the GOMS MFM inversion process.

4.1 Measurement Uncertainty

To determine the appropriate number of significant digits to be used in MFM spectral matching, as well as in reporting the measurements, the 550 nm, 670 nm, and 800 nm measurements were extracted from the data for each of the ten Spectralon™ datasets at a 10 nm resolution, and each distribution was plotted on a separate normal probability plot. Analysis of the ten measurements of the identically positioned and illuminated target with the USB4000 via normal probability plots showed the measurements for each sampled dataset to be normally distributed. Figures 4.1, 4.2, and 4.3 show these results for

the 550 nm, 670 nm, and 800 nm wavelengths, respectively; where the measurements are displayed as raw Digital Numbers (DNs).

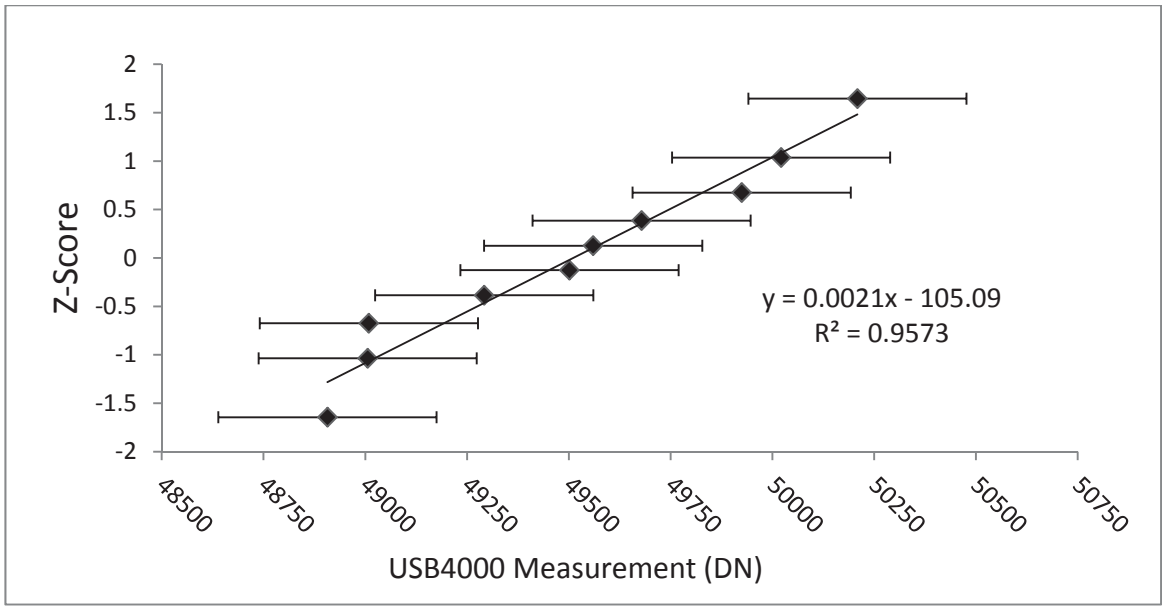

Figure 4.1: Ocean Optics USB4000 spectrometer measurement uncertainty test results at the 550 nm Waveband. Error bars correspond to a 95% confidence interval.

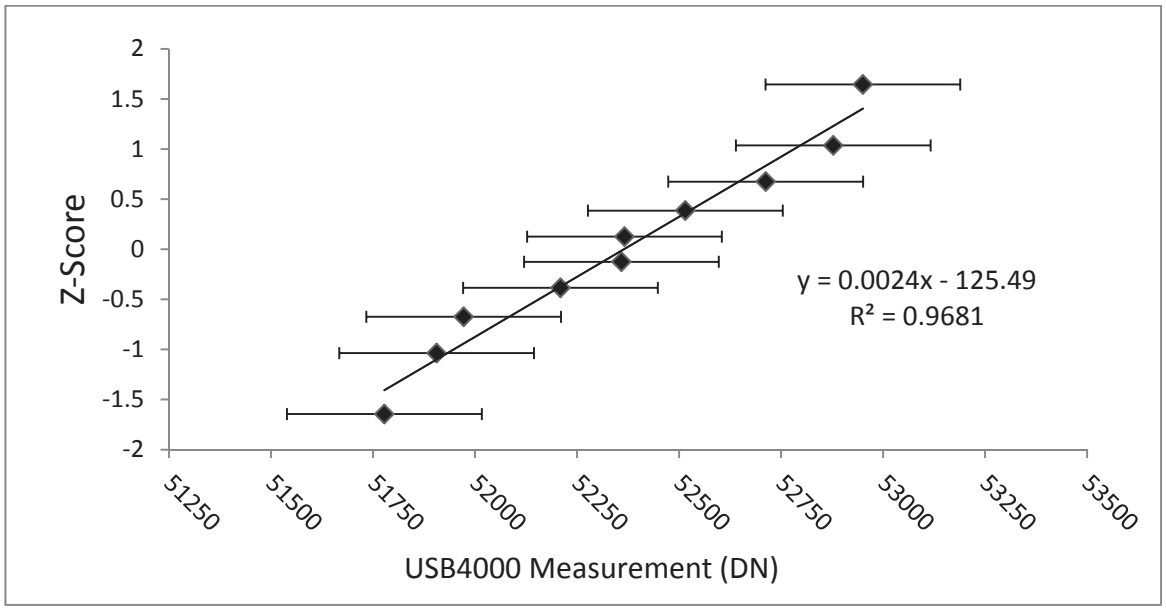

Figure 4.2: Ocean Optics USB4000 spectrometer measurement uncertainty test results at the 670 nm Waveband. Error bars correspond to a 95% confidence interval.

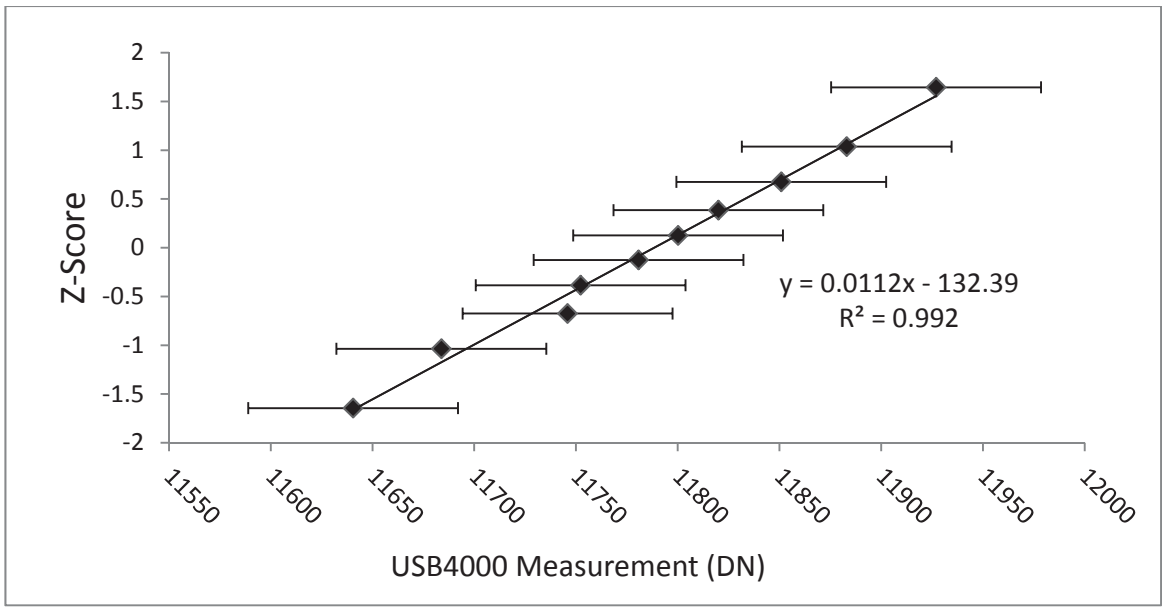

Figure 4.3: Ocean Optics USB4000 spectrometer test results at the 800 nm Waveband. Error bars correspond to a 95% confidence interval.

The measurement uncertainty for each dataset was calculated to a 95% confidence interval, and the absolute measurement uncertainty was found to vary for each measurement. However, conversion of each absolute measurement uncertainty value to relative uncertainty revealed that the relative uncertainty of each measurement stayed constant at a value of 0.02, or 2%.

Because the measurements collected are independent of one another and conform to the Gaussian distribution, propagation of the absolute uncertainty when dark current values are subtracted is calculated by first multiplying the measurement value by 0.02, and subsequently calculating the summation of the two input uncertainties in quadrature:

$$\delta q_a = \sqrt{(\delta x_a)^2 + (\delta y_a)^2} \tag{4.1}$$

where δq_a is the total propagated absolute measurement uncertainty, and δx_a and δy_a are the calculated absolute measurement uncertainties for the dark current and the dataset the dark current is being subtracted from, respectively. Similarly, the overall relative

measurement uncertainty for the division step in the calculation of reflectance is calculated using

$$\delta q_r = \sqrt{(\delta x_r)^2 + (\delta y_r)^2} \tag{4.2}$$

where δq_a is the total propagated relative measurement uncertainty, and δx_r and δy_r are the calculated relative measurement uncertainties for the target and the white reference panel, respectively. This overall relative uncertainty value is then multiplied by the obtained HCRF value, providing a final measurement uncertainty value in the same units as the measured HCRF.

A notable consequence of the measurements having a constant relative error is the fact that the total measurement uncertainty varies for each and every measurement, and the overall uncertainty in each HCRF measurement is highly dependent on the magnitude of each measured signal. With each individual HCRF dataset consisting of over 200 measurements, it was deemed impractical to apply uncertainty propagation techniques to every measurement to determine the number of significant digits to be used in MFM spectral matching. Therefore, error propagation calculations were performed on a sample of six different datasets, two for each waveband. It was found that each sampled HCRF measurement had an uncertainty between ±0.5% reflectance and ±2% reflectance at a 95% confidence interval. In order to avoid the introduction of false precision in outputs, which could have the effect of excluding MFM returns which are in fact spectral matches, it was therefore determined that HCRF measurements and GOMS-MFM results should be rounded to the nearest percent reflectance. Therefore, all measured and modelled reflectance values in this section have been rounded to the nearest percent.

4.2 Reflectance Properties of Endmember Panel Datasets

HCRF plots derived from spectrodirectional measurements of the sunlit endmember data showed extremely different bidirectional reflectance properties for the canopy flocking material and the background felt material. The background material was found to have had reflectance characteristics which were not as diffuse as expected; the HCRF plots interpolated for this material showed a high degree of forward scattering in interpolated HCRF plots. This forward-scattering is apparent in the HCRF plots derived for both illumination angles; the brightest portion of the interpolated HCRF plot surface for both plots is near the forward-scatter direction in the hemisphere near the same zenith angle as the illumination is located.

The interpolated HCRF plot surface for the sunlit canopy endmember displayed a clearly delineated hot spot at both the summer and winter illumination angles, as can be seen in Figure 4.4. This distinct hot spot is likely caused by microshadowing from the textured flocking, and subsequent shadow hiding effects when the sensor is near the location of illumination. However, a hot spot can also be seen in the surface BRDF in the forward-scatter direction the winter illumination angle was implemented, indicating strong forward scattering of canopy material's reflectance under certain illumination conditions.

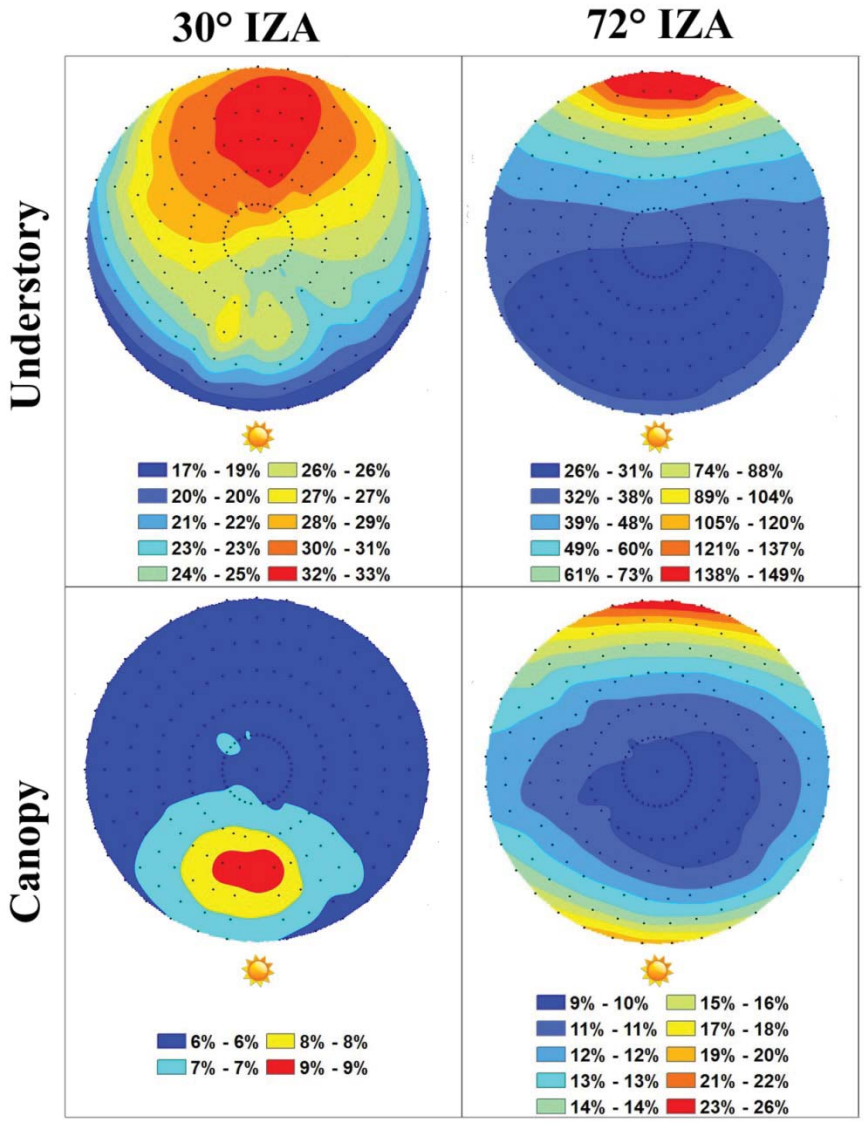

Figure 4.4: HCRF plots for the two different model component endmembers. Due to similarity between plots at each waveband, the 550 nm waveband is displayed. The direction of illumination in the SPP is indicated by an icon of the sun.

4.3 GOMS Forward-Mode

GOMS was implemented in forward mode in order to model the model forest's hemispherical-conical reflectance values based on the use of average measured values for canopy structure. RMSE was calculated for each corresponding pair of GOMS simulated and ULGS-2 measured values in order to identify whether significant differences exist between data pairs. The ability of the model to predict measured values was quantified

based on the RMSE for each dataset pair, and described via visual analysis of the interpolated plots. This was performed on both the reflectance values and the nadir-normalized values, allowing for the evaluation of not only the model's ability to simulate reflectance values, but its ability to model anisotropy itself.

4.3.1 GOMS Forward Mode: Normalized

Comparison of the patterns of anisotropy observed in HCRF plots is useful in understanding the reflectance patterns of a surface, but proper comparison between plots requires some specialization of data. In this section, the data found in the plots has been normalized in relation to nadir reflectance. This comparison to the reflectance values in relation to the reflectance at nadir allows for the anisotropy patterns of a plot to be evaluated, and the patterns can specifically be compared to those found in other plots. The following nadir-normalized values are represented by a single legend, found at the top of each figure. The plotted results for the datasets illuminated at the summer solar angle can be found in Figure 4.5, with the corresponding statistical results shown in Table 4.1. The plotted results for the datasets illuminated at the winter solar angle are found in Figure 4.6, with their corresponding statistical results shown in Table 4.2.

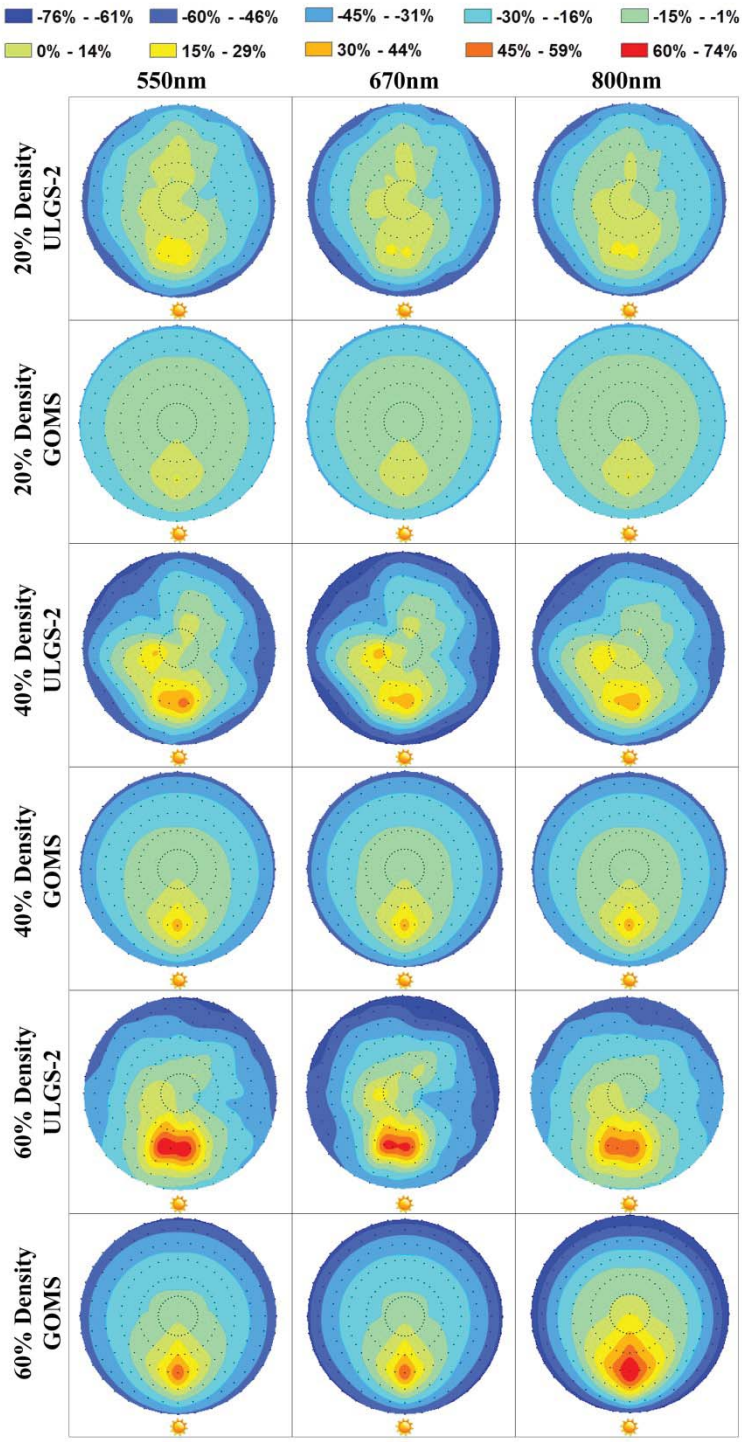

Figure 4.5: HCRF plots derived from nadir-normalized ULGS-2 and GOMS samples illuminated with an IZA of 30°.

Table 4.1: Statistical results for ULGS-2 and GOMS nadir-normalized datasets illuminated at a 30° IZA.

Dataset ID and Waveband	Standard Error	RMSE
20% Crown closure 550nm	0.08	0.005
20% Crown closure 670nm	0.07	0.005
20% Crown closure 800nm	0.06	0.004
40% Crown closure 550nm	0.09	0.006
40% Crown closure 670nm	0.11	0.007
40% Crown closure 800nm	0.08	0.006
60% Crown closure 550nm	0.11	0.007
60% Crown closure 670nm	0.10	0.007
60% Crown closure 800nm	0.09	0.006

Normalized values were plotted using an equal interval classification with the same range applied to all plots in order to allow for visual comparison between the varying forest densities and illumination conditions. Data collected at an illumination zenith angle of 30° clearly shows the expected location of the hotspot at a 30° viewing the zenith angle in the backscatter direction. The expected location of the dark area in the forward-scattering direction shows high levels of reflectance at low forest densities, as is to be expected based upon the observed HCRF plot of the background material. The plots show the expected symmetry about the principal plane and asymmetry about the orthogonal principal plane.

The RMSE value was derived for each measured and modelled dataset pair in order to determine which of the measured validation data sets was modelled most closely by the GOMS algorithm. The lowest RMSE results were acquired for the 20% crown closure forest cover dataset measured at the 800 nm waveband. However, all comparisons resulted in desirably low RMSE values.

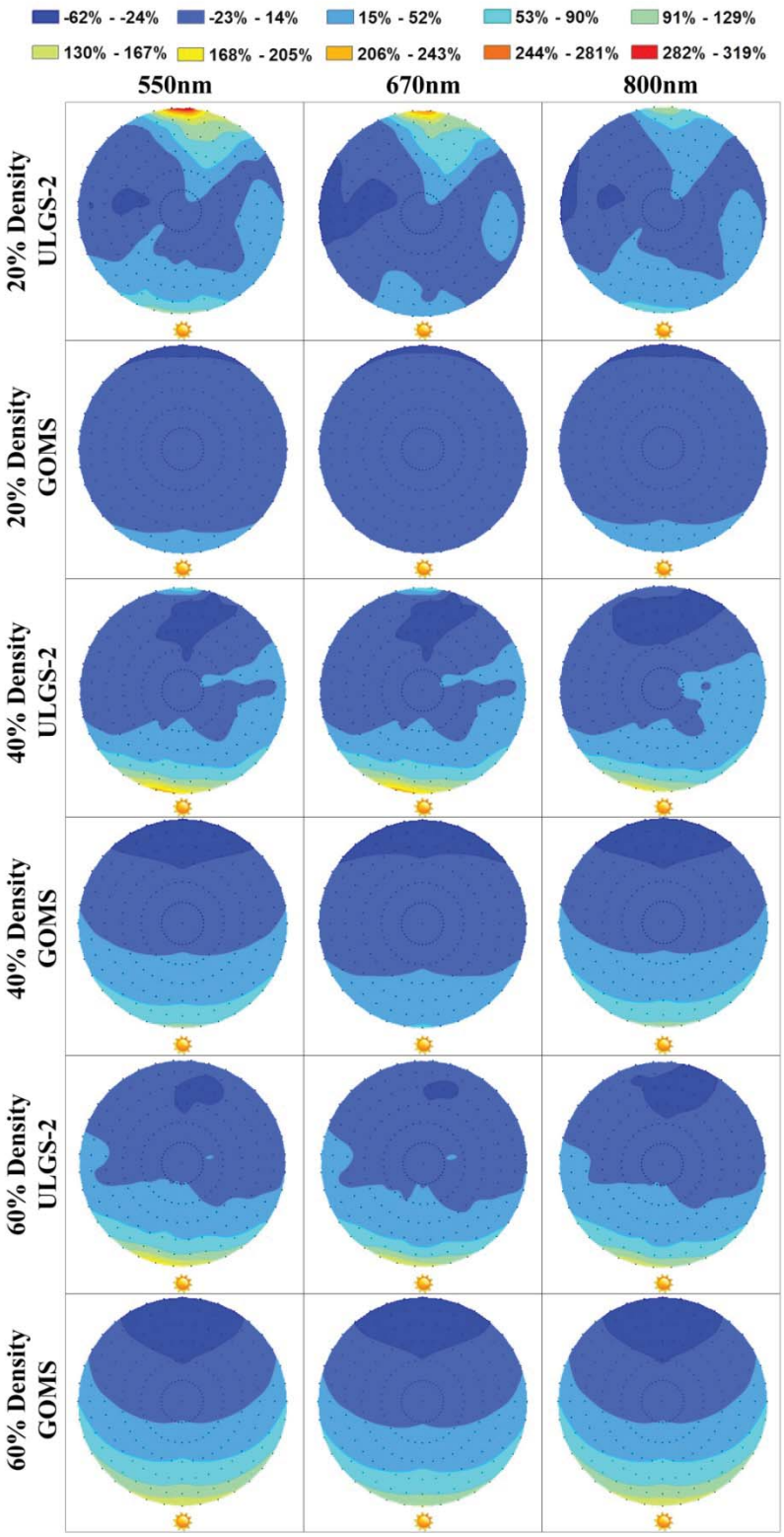

Figure 4.6: HCRF plots derived from nadir-normalized ULGS-2 and GOMS samples illuminated with an IZA of 77°.

Table 4.2: Statistical results for ULGS-2 and GOMS nadir-normalized datasets illuminated at a 77° IZA.

Dataset ID and Waveband	Standard Error	RMSE
20% Crown closure 550nm	0.44	0.03
20% Crown closure 670nm	0.34	0.02
20% Crown closure 800nm	0.25	0.02
40% Crown closure 550nm	0.23	0.02
40% Crown closure 670nm	0.25	0.02
40% Crown closure 800nm	0.16	0.01
60% Crown closure 550nm	0.14	0.01
60% Crown closure 670nm	0.13	0.01
60% Crown closure 800nm	0.09	0.01

Data collected at an illumination zenith angle of 77° displays the same forward-scattering characteristics of the background material at low forest densities. However, this effect is muted as forest crown closure increases, and the expected dark area in the forward-scatter direction caused by the backshadow effect can be seen in the 40% and 60% crown closure forest HCRF plots. A hot spot driven by shadow hiding can be seen in all of the measured HCRF plots, and the shape, size, and location of the GOMS modelled hot spots correspond well with them. In terms of the statistical analysis, the higher crown closure forests display the most desirable results. This is likely due to the disappearance of the unwanted forward-scattering effects of the background as the amount of sunlit background depletes with the increased number of trees in the plot.

4.3.2 GOMS Forward Mode: Reflectance

While normalizing the reflectance values and displaying each of them upon the same classification range is useful in inter-plot pattern comparison, it is also important to understand the variations in patterns on an intra-plot level. The following HCRF plots based on reflectance values utilize Jenks natural breaks classification applied to a spline interpolation of the sampled reflectance values. Ten classes were interpolated for each dataset with a sufficient range of data. However, in situations where the range of reflectance values is less than ten percent, the number of classifications has been reduced to be equal to the number of available reflectance values in order to retain the maximum amount of possible information about the plots. Each plot has an associated legend with values particular to that plot contained within. Figure 4.7, Figure 4.8, and Figure 4.9 illustrate the results corresponding to three different canopy coverage datasets corresponding to the summer illumination angle, and Figure 4.10, Figure 4.11, and Figure 4.12 illustrate the results corresponding to the winter illumination angle. Statistical results for the summer and winter output are shown in Table 4.3 and Table 4.4, respectively.

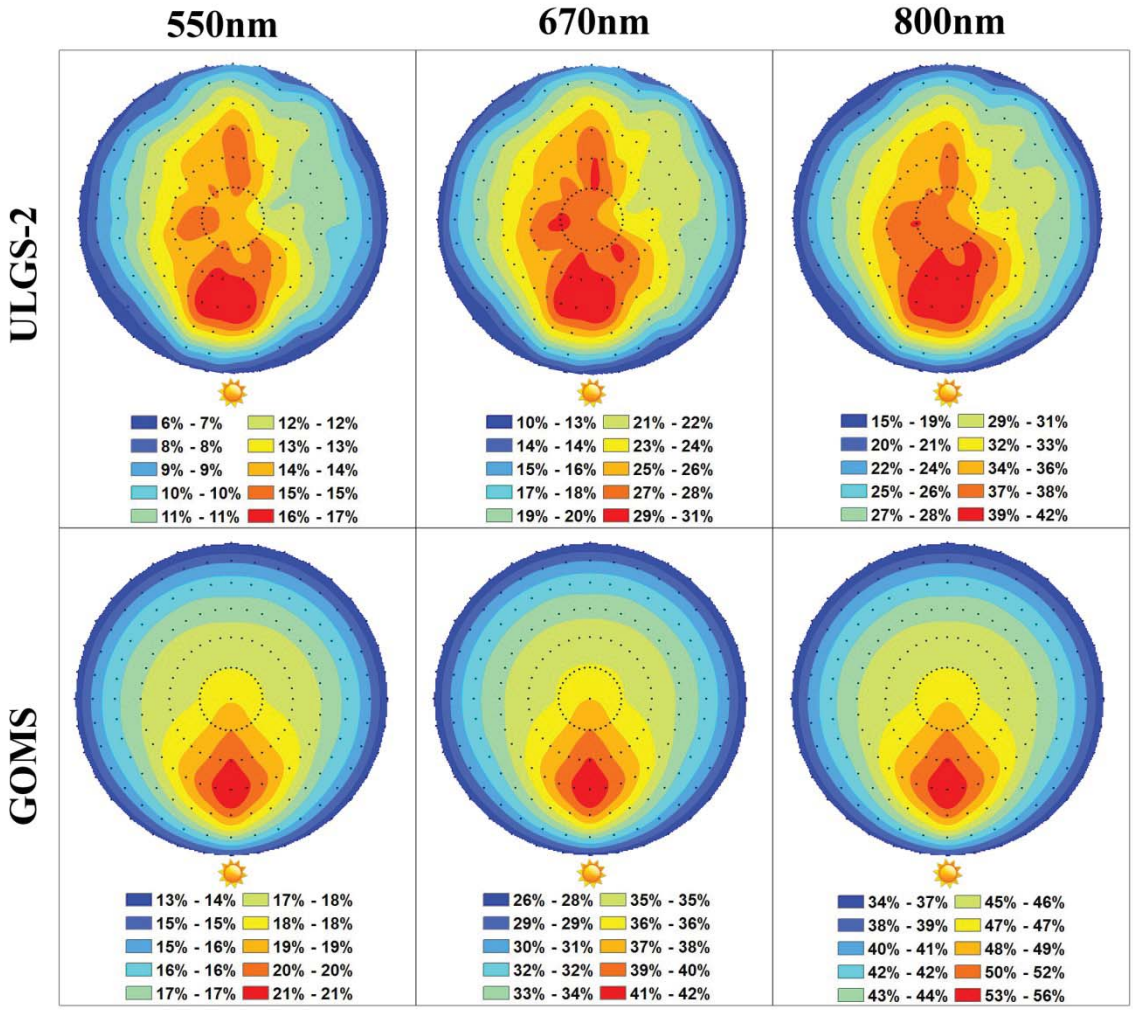

Figure 4.7: HCRF reflectance plots for the 20% crown closure simulated forest, derived from ULGS-2 and GOMS samples illuminated with an IZA of 30°.

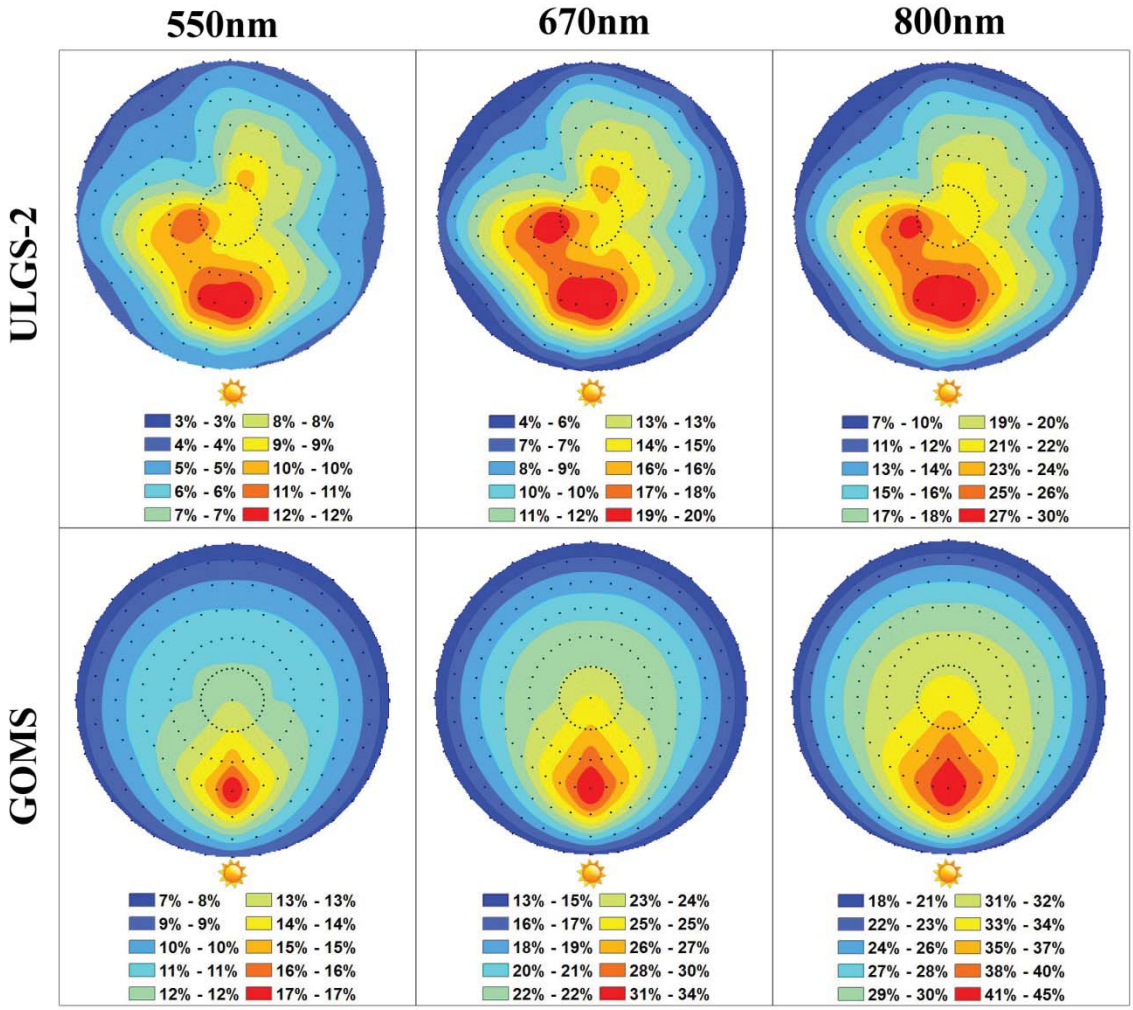

Figure 4.8: HCRF reflectance plots for the 40% crown closure simulated forest, derived from ULGS-2 and GOMS samples illuminated with an IZA of 30°.

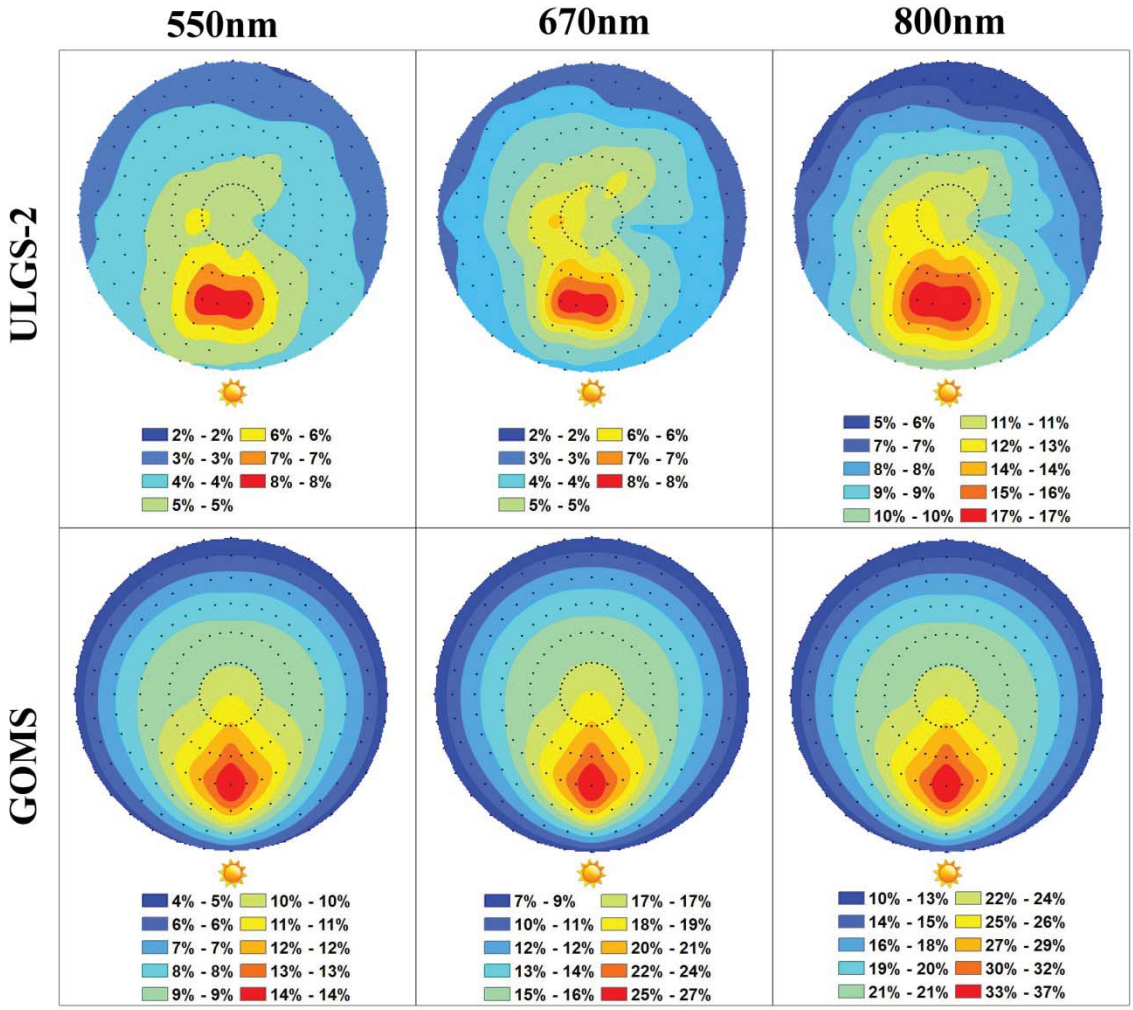

Figure 4.9: HCRF reflectance plots for the 60% crown closure simulated forest, derived from ULGS-2 and GOMS samples illuminated with an IZA of 30°.

Table 4.3: Statistical results for ULGS-2 and GOMS reflectance datasets illuminated at a 30° IZA.

Dataset ID and Waveband	Standard Error	RMSE
20% Crown closure 550nm	0.01	0.001
20% Crown closure 670nm	0.02	0.001
20% Crown closure 800nm	0.02	0.001
40% Crown closure 550nm	0.01	0.001
40% Crown closure 670nm	0.02	0.001
40% Crown closure 800nm	0.02	0.001
60% Crown closure 550nm	0.004	0.0003
60% Crown closure 670nm	0.006	0.0004
60% Crown closure 800nm	0.01	0.0007

In these datasets collected at the 30° IZA, the location of the hot spot can be easily seen, and tends to be reduced in size in both the azimuthal and Zenith domains as forest crown closure increases. Expected symmetry about the SPP can be seen to increase as the forest crown closure increases, corresponding to an increase in agreement between the patterns seen in the plot pairs. The location and size of the hot spot are well-delineated by GOMS, and the overall patterns in the GOMS plots correspond well with the measured HCRF plots. It can also be noted that, as forest crown closure increases, the overall reflectance values in the scene tend to decrease. Overall, the locations of the diagnostic features and the overall patterns of the plots tend to be quite similar, and experienced similar changes as forest crown closure increases. Regression analysis of the datasets resulted in the highest coefficient of determination and lowest RMSE value being obtained by the dataset collected at 60% forest cover crown closure at the 550 nm waveband. Similar to the nadir-normalized results, the reflectance values modelled by GOMS were generally overestimated.

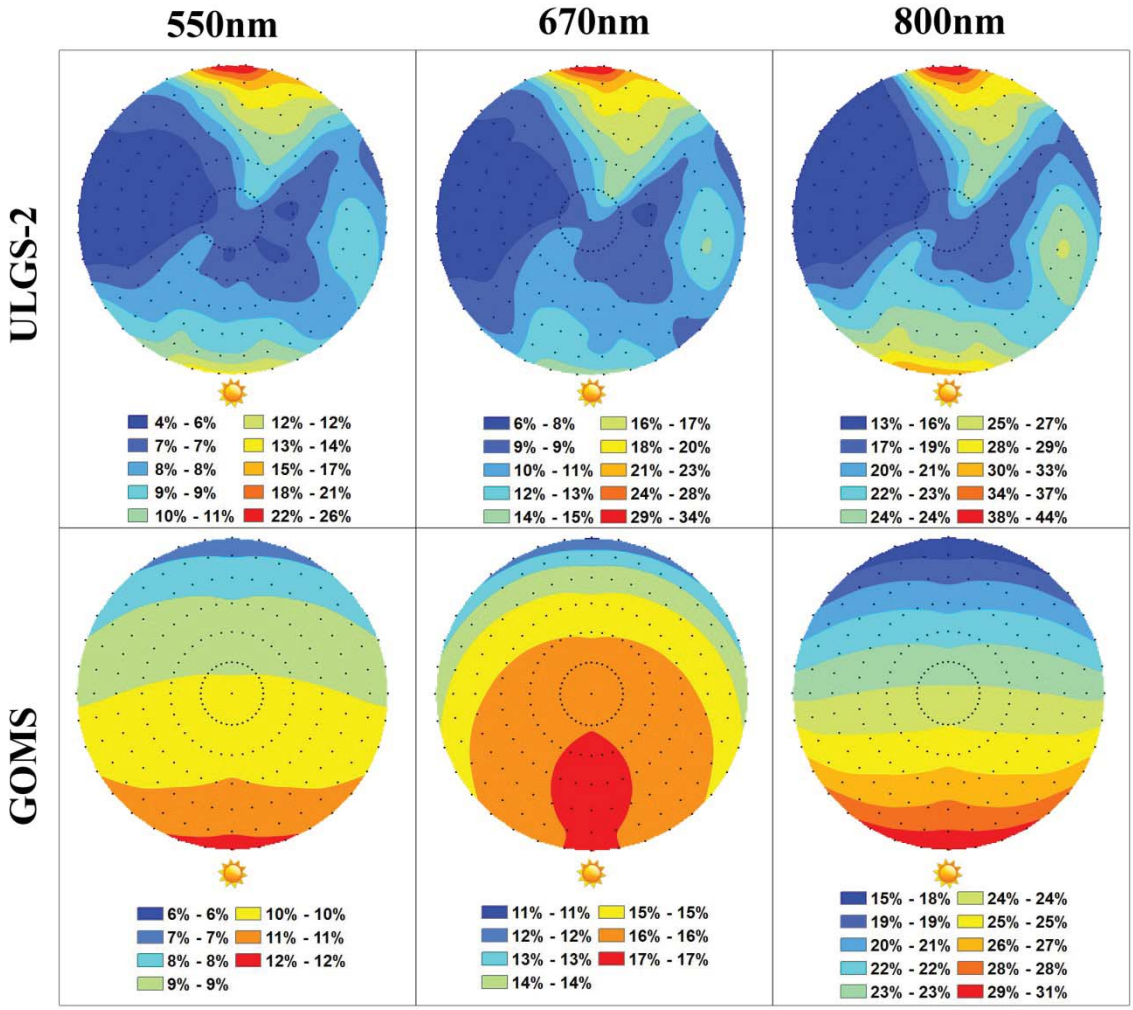

Figure 4.10: HCRF reflectance plots for the 20% crown closure simulated forest, derived from ULGS-2 and GOMS samples illuminated with an IZA of 77°.

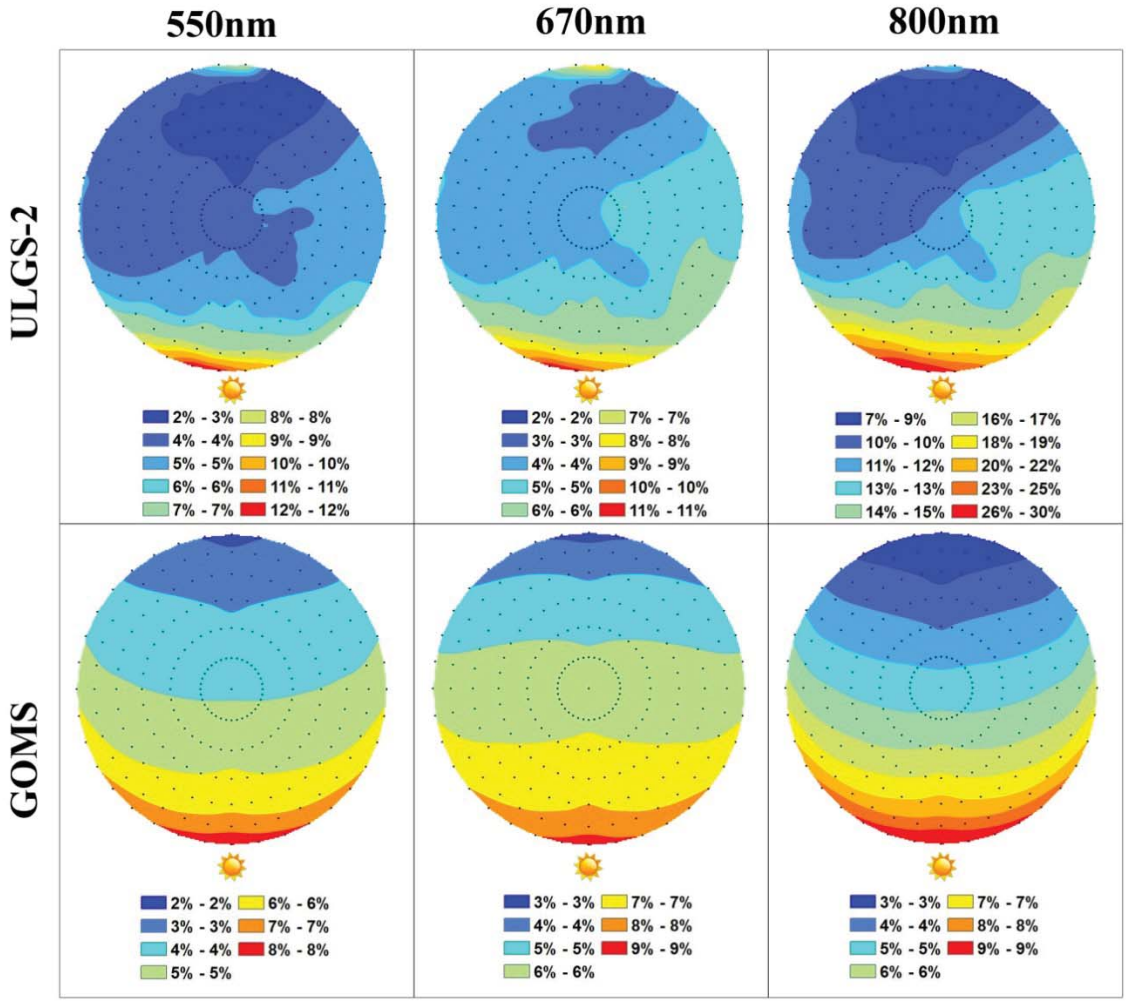

Figure 4.11: HCRF reflectance plots for the 40% crown closure simulated forest, derived from ULGS-2 and GOMS samples illuminated with an IZA of 77°.

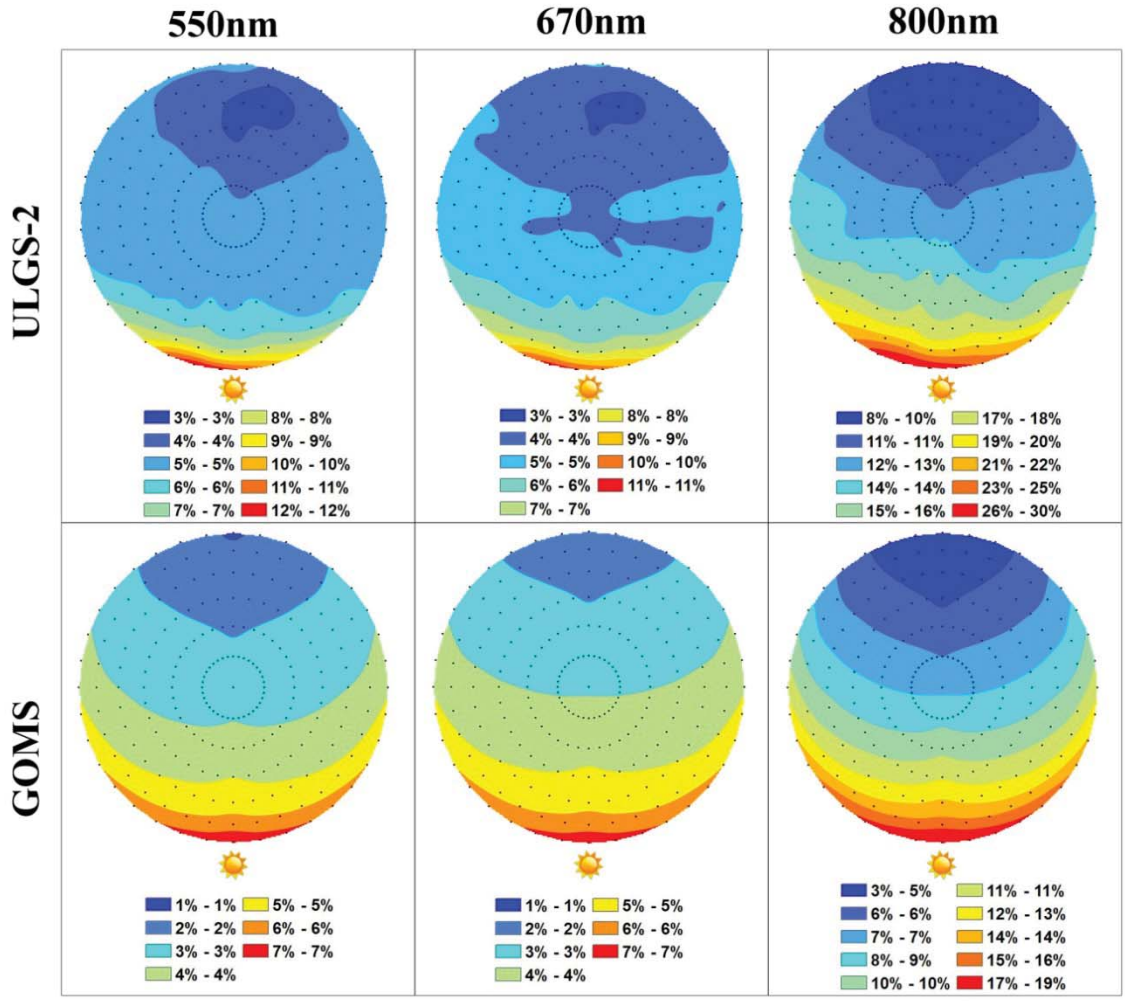

Figure 4.12: HCRF reflectance plots for the 60% crown closure simulated forest, derived from ULGS-2 and GOMS samples illuminated with an IZA of 77°.

Table 4.4: Statistical analysis of reflectance data for simulated forests illuminated at a 77° IZA.

Dataset ID and Waveband	Standard Error	RMSE
20% Crown closure 550nm	0.03	0.002
20% Crown closure 670nm	0.03	0.002
20% Crown closure 800nm	0.05	0.003
40% Crown closure 550nm	0.01	0.001
40% Crown closure 670nm	0.01	0.001
40% Crown closure 800nm	0.02	0.001
60% Crown closure 550nm	0.01	0.0004
60% Crown closure 670nm	0.01	0.0003
60% Crown closure 800nm	0.01	0.0007

The issues with spectral data collected at the 77° IZA observed in the normalized HCRs plots can be seen in an even more pronounced manner in the reflectance plots at the lowest forest crown closure. However, at 40% and 60% forest crown closure, the location of the hot spot and the dark spots are once again located in the approximate expected locations in the backscatter and forward scatter directions, respectively. Similarly to the plots collected at a 30° IZA, as crown closure increases, the overall reflectance values in the plots decrease, as is to be expected with a background material which has a higher reflectance than the material used to create the canopy. In contrast to the simulated summer datasets, the GOMS modelled reflectance values for these plots were overestimated. However, similar to the simulated summer datasets, the RMSE once again becomes more favorable as forest crown closure increases, highlighting the background's specular reflectance being the limiting factor in GOMS' ability to model the simulation.

4.4 Nadir MFM Inversion Forest Structure Validation

MFM inversion was run for each forest dataset at both illumination angles and all three wavebands, resulting in a total of 18 datasets being created for analysis. Each MFM-LUT dataset returned 92 000 results. The nadir reflectance value collected by the ULGS-2 for each simulated forest dataset was used to identify spectral matches in the MFM-LUT. Spectral proximity analysis was unnecessary due to spectral matches being attained for each MFM dataset.

Following the isolation of spectral matches from the MFM-LUT, histograms were developed for each structural variable in each LUT with the goal of performing distribution analysis upon the returned structural parameters. Distribution analyses

revealed sufficient normality in the LUT matches to allow for parametric statistics to be used to describe the structural data. Table 4.5 and Table 4.6 outline the results of the inverted structural values retrieved via spectral matching in the MFM-LUT for the summer and winter datasets, respectively.

Table 4.5: Comparative statistics for a-priori measured structural values and GOMS modelled structural values

	# of Match	Meas. td	Mod. td	Abs.Diff. td	Meas. r	Mod. r	Abs. Diff r	Meas. b	Mod. b	Abs. Diff. b	Meas. h	Mod. h	Abs. Diff. h	Meas. dh	Mod. dh	Abs. Diff. Dh
20% CC 550nm	2901	0.015	0.040	0.025	1.98	2.87	0.89	2.94	2.30	0.64	6.05	5.34	0.71	5.76	5.70	0.06
20% CC 670nm	878	0.015	0.035	0.020	1.98	2.34	0.36	2.94	3.02	0.08	6.05	4.94	1.11	5.76	5.70	0.06
20% CC 800nm	985	0.015	0.036	0.021	1.98	2.62	0.64	2.94	2.46	0.48	6.05	5.12	0.93	5.76	5.70	0.06
40% CC 550nm	3181	0.030	0.043	0.013	1.97	3.15	1.18	2.91	2.84	0.07	5.97	5.37	0.60	5.60	5.70	0.10
40% CC 670nm	1485	0.030	0.042	0.012	1.97	3.10	1.13	2.91	2.52	0.39	5.97	5.26	0.71	5.60	5.70	0.10
40% CC 800nm	1076	0.030	0.042	0.012	1.97	2.85	0.88	2.91	2.73	0.18	5.97	5.35	0.62	5.60	5.70	0.10
60% CC 550nm	5805	0.045	0.055	0.010	1.97	3.79	1.82	2.94	3.36	0.42	5.98	5.85	0.13	5.44	5.70	0.26
60% CC 670nm	3523	0.045	0.056	0.011	1.97	3.85	1.88	2.94	2.70	0.24	5.98	5.82	0.16	5.44	5.70	0.26
60% CC 800nm	2269	0.045	0.055	0.010	1.97	3.81	1.84	2.94	3.12	0.18	5.98	5.73	0.25	5.44	5.70	0.26

Table 4.6: Comparative statistics for a-priori measured structural values and GOMS modelled structural values

	# of Match	Meas. td	Mod. td	Abs.Diff. td	Meas. r	Mod. r	Abs. Diff.r	Meas. b	Mod. b	Abs. Diff. b	Meas. h	Mod. h	Abs. Diff. h	Meas. dh	Mod. dh	Abs. Diff. Dh
20% CC 550nm	4027	0.015	0.053	0.038	1.98	3.65	1.67	2.94	3.47	0.53	6.05	5.82	0.23	5.76	5.70	0.06
20% CC 670nm	2527	0.015	0.055	0.040	1.98	3.70	1.72	2.94	2.75	0.19	6.05	5.76	0.29	5.76	5.70	0.06
20% CC 800nm	1451	0.015	0.052	0.037	1.98	3.61	1.63	2.94	3.21	0.27	6.05	5.35	0.70	5.76	5.70	0.06
40% CC 550nm	5006	0.030	0.063	0.033	1.97	3.97	2.00	2.91	4.30	1.39	5.97	6.12	0.15	5.60	5.70	0.10
40% CC 670nm	3746	0.030	0.064	0.034	1.97	4.19	2.22	2.91	4.26	1.35	5.97	6.17	0.20	5.60	5.70	0.10
40% CC 800nm	1952	0.030	0.063	0.033	1.97	3.91	1.94	2.91	4.26	1.35	5.97	6.15	0.18	5.60	5.70	0.10
60% CC 550nm	5006	0.045	0.063	0.018	1.97	3.97	2.00	2.94	4.30	1.36	5.98	6.12	0.14	5.44	5.70	0.26
60% CC 670nm	3746	0.045	0.064	0.019	1.97	4.19	2.22	2.94	4.26	1.32	5.98	6.17	0.19	5.44	5.70	0.26
60% CC 800nm	1952	0.045	0.063	0.018	1.97	3.91	1.94	2.94	4.26	1.32	5.98	6.15	0.17	5.44	5.70	0.26

The performance of GOMS-MFM canopy structure inversion techniques varied widely depending on the dataset. GOMS-MFM was able to obtain exact spectral matches for each dataset, so spectral proximity matching was not required. The 550 nm waveband was able to obtain the largest number of matches for each dataset, and overall, the number of obtained spectral matches increased with forest density. The td statistic, highlighting the forest density, was modelled most accurately at high forest crown closures. In both illumination cases, structure for the horizontal crown radius was modelled most accurately in the lowest crown closure forest datasets, with sub-centimetre accuracy obtained in the case of the for both the r and b parameters in the summer illumination case.

In both illumination cases, GOMS-MFM's ability to model the height distribution of the forest decreased as forest crown closure increased. Interestingly, the height to crown center statistic was modelled most accurately at high forest densities for the simulated summer IZA, whereas it was modelled most accurately at low forest densities for the simulated winter IZA. However, many matches were obtained at sub-centimeter accuracy. To provide context of these results in terms of MFM structure retrieval of a true forest canopy, with the scale factor of 1:152 being applied, this result would be analogous to estimating canopy structure of a real tree to an accuracy greater than 1.5 m; a favorable result. .

4.5 Forest Target Rotational Variance

When the 20% crown closure simulated forest is rotated 90° clockwise, subtle variations in the BRDF were visible. While the hot spot extends further into the forward-scatter direction in the HCRF corresponding to the scene where the forest was rotated, a

circular hot spot in the expected location in the SPP is consistently seen in both scenes. The magnitude of the sampled reflectance values did not change with the rotation of the simulated forest. HCRF plots corresponding to the forest as it was normally oriented, and after rotating the plot 90° can be seen in Figure 4.13.

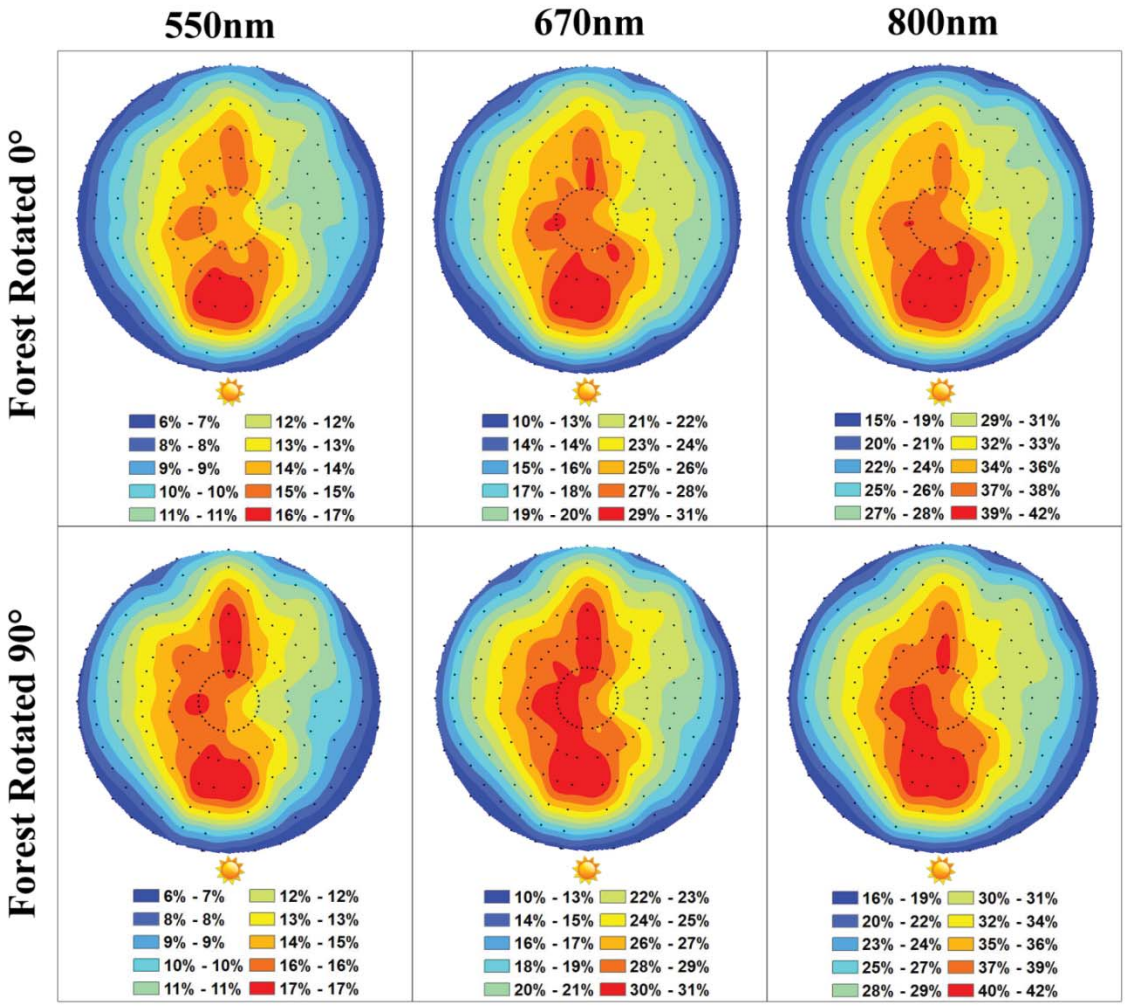

Figure 4.13: HCRF plots derived from 20% crown closure simulated forest showing forest plot rotational variance. Shown on bottom are HCRF plots for the forest after it's been rotated 90°.

4.6 AMBRALS Forward-Modelled MODIS BRDF Product

The MODIS BRDF product is capable of modelling canopy BRDF by taking into account multiangle measurements of a single target and using the measurements to determine which combination of kernel model weighting values best describe the

observed reflectance anisotropy. The APPEARs software provided by the ORNL DAAC was used to obtain the three required kernel weighting parameters for the BOREAS SSA OJP flux tower location in order to be utilized with the custom software developed based upon the AMBRALS modelling framework. The software was used to model reflectance based upon varying Sun-sensor geometry over the entire hemisphere at a 10 degree angular resolution. Subsequently, HCRF plot surfaces were interpolated from these datasets. This procedure was performed for three different years: 2001, 2014, and 2016. Because the kernel parameters correspond to measurements over a 16 day period, the date specified in the MODIS metadata corresponds to the date at the center of the 16-day measurement span. These 2001 and 2016 datasets correspond to the date of June 26, while the 2014 dataset corresponds to June 25. The SZA for both dates at solar noon is 30.59°. The HCRF plots derived from these datasets shown in Figure 4.14.

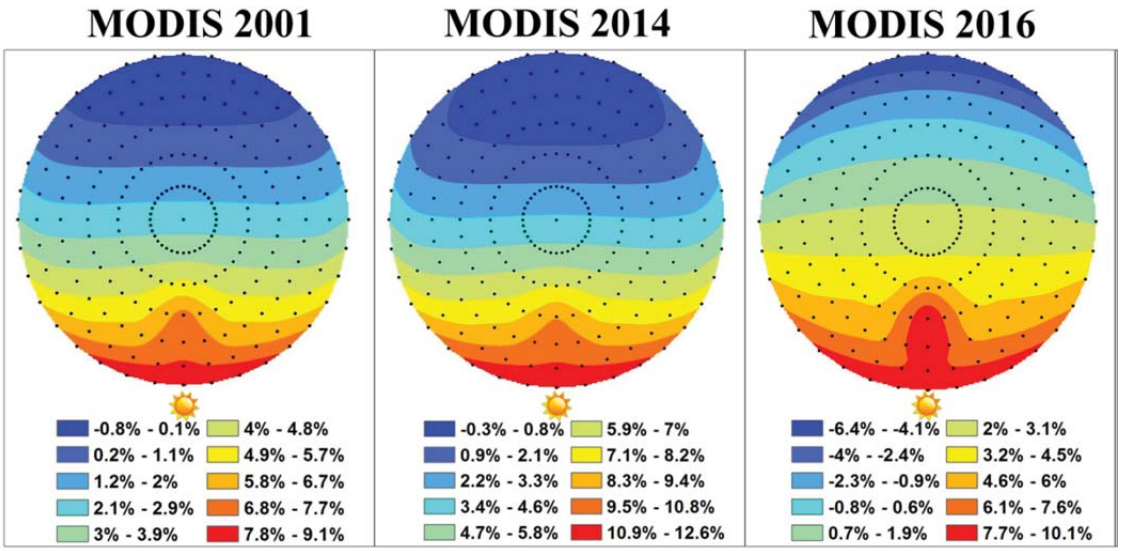

Figure 4.14: HCRF plot surfaces derived from modelled reflectance values attained through the AMBRALS modelling framework and the MODIS BRDF Parameters product

The varying weighting coefficients gathered for the three different years resulted in three distinct surfaces with varying reflectance patterns and values acquired for each dataset. Notably, while the solar zenith location was specified to be 30.47° in order to

evaluate agreement between modelled BRDF results derived from MODIS and those derived from the other methods used in this study, a distinct hotspot centered at the 30° zenith location in the SPP is not seen in the 2001 and 2014 datasets, whereas it is in the 2016 dataset. Negative reflectance values in the forward-scatter direction point to a potential flaw in the RTLSR model's implementation with the AMBRALS framework.

4.7 BOREAS SSA OJP PARABOLA-2 Field Data HCRF Plot

PARABOLA-2 field data collected above the forest canopy at the BOREAS SSA OJP flux tower site was processed into a form which allowed the points to be plotted in Cartesian space and allowed for a HCRF plot surface to subsequently be derived from it. The SZA on May 31 at the time of data collection at the BOREAS SSA OJP is 33.24°, with a solar azimuth angle of 159.77° Results can be seen in figure 4.15.

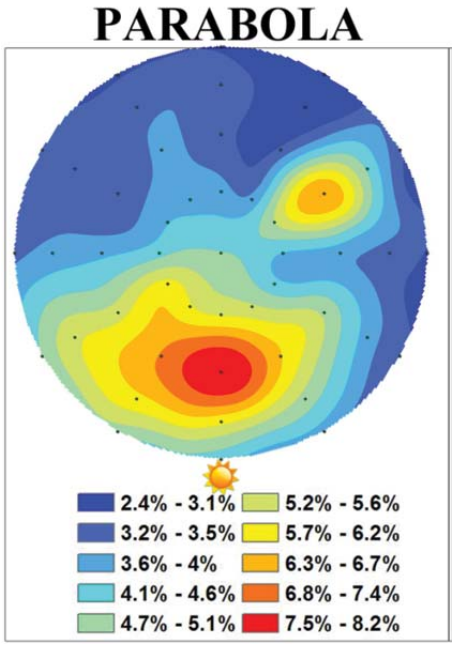

Figure 4.15: HCRF plot derived from PARABOLA-2 data collected *in situ* via a tram located above the forest canopy at the BOREAS SSA OJP flux tower location.

Patterns in the HCRF plot generally follow expected behavior, with a hot spot located near the location of the Sun in the hemisphere near the 30° zenith angle location

in the SPP. One point in the forward-scatter direction has a reflectance value higher than would be expected, however. It is possible that observed departures from expected BRDF patterns are related to spectra being contaminated by the flux tower which the PARABOLA-2's tram is adjacent to. The magnitude of the measured HCRF values align well with the magnitude observed in the GOMS forward-modelling outputs.

4.8 GOMS Sunlit and Shadowed Abundances

A primary product of the GOMS modelling software is the fractional contribution of each of the components being modelled to the overall signal. In the case of the three-component model utilized in this version of the GOMS software, fractional abundances of the sunlit canopy, sunlit background, and shadow components expected to be observed by a sensor based on its viewing angle, the relative angle of illumination, and the structural details of the forest are calculated. In order to validate these abundances at nadir, a circular area representing the area sensed by the FOV was superimposed over digital photographs of the forest taken at nadir for the 20%, 40%, and 60% crown closure forests, and the images were subsequently cropped to exclude the area outside the FOV. These images were then classified into three categories representing the types of components in the three-component GOMS model through the use of a maximum likelihood supervised classification.

The number of pixels determined to belong to each class were subsequently divided by the total number of pixels viewed by the FOV, yielding fractional abundances of each of the components. These abundances were then compared to the fractional abundances of each component calculated by the GOMS modelling software. In order to compare all of the results to one another, normalized difference ND was calculated as

$$ND = \frac{(ML - G)}{ML} \cdot 100 \tag{4.3}$$

where ML is the maximum likelihood fraction value, and G is the fractional abundance value modelled by GOMS. The calculated abundances varied slightly by waveband; therefore the mean value for the three sampled wavebands was used to calculate GOMS' fractional abundance value for each dataset. An example of the result obtained from the maximum likelihood classification can be seen in Figure 4.16. The results obtained from this test for the sunlit canopy, sunlit background, and shadow components are found in Table 4.7, 4.8, and 4.9, respectively.

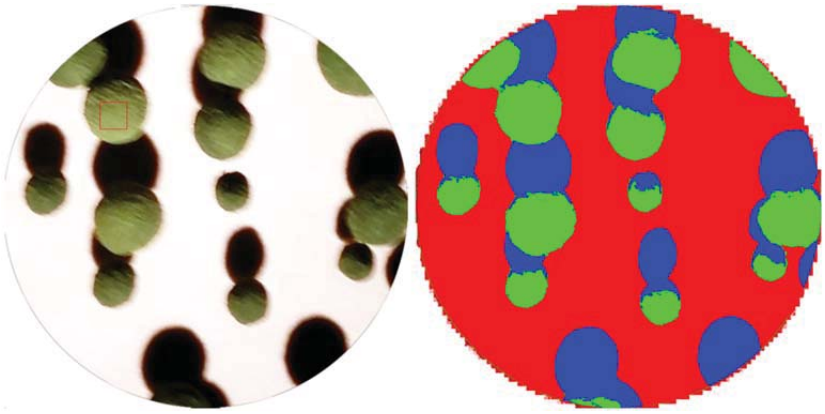

Figure 4.16: Example of maximum likelihood classification applied to plot photo. Shown is the 20% forest cover crown closure simulated forest, cropped to the area observed by the spectrometer at the nadir position. Areas of sunlit canopy (Cf), sunlit background (Bf), and shadow (Sf) are represented by green, red, and blue, respectively.

Table 4.7: Sunlit canopy fraction (Cf) maximum likelihood validation and GOMS modelled abundances

	Max. Likelihood Cf	GOMS Cf	Absolute Difference	Normalized Difference (%)
20% CC Summer	0.1574	0.1432	0.0142	9.00
40% CC Summer	0.3497	0.2553	0.0944	26.99
60% CC Summer	0.5266	0.3472	0.1794	34.07
20% CC Winter	0.1152	0.0673	0.0479	41.62
40% CC Winter	0.2431	0.1012	0.1420	58.39
60% CC Winter	0.3231	0.1265	0.1966	60.86

Table 4.8: Sunlit background fraction (Bf) maximum likelihood validation and GOMS modelled abundances.

	Max. Likelihood Bf	GOMS Bf	Absolute Difference	Normalized Difference (%)
20% CC Summer	0.6483	0.6683	0.0200	-3.09
40% CC Summer	0.3635	0.4516	0.0881	-24.24
60% CC Summer	0.1637	0.3027	0.1390	-84.89
20% CC Winter	0.3134	0.2432	0.0702	22.41
40% CC Winter	0.1071	0.0616	0.0455	42.49
60% CC Winter	0.0615	0.0147	0.0468	76.04

Table 4.9: Shadow fraction (Sf) maximum likelihood validation and GOMS modelled abundances.

	Max. Likelihood Sf	GOMS Sf	Absolute Difference	Normalized Difference (%)
20% CC Summer	0.1943	0.1884	0.0059	3.02
40% CC Summer	0.2868	0.2931	0.0063	-2.19
60% CC Summer	0.3097	0.3502	0.0405	-13.06
20% CC Winter	0.5715	0.6896	0.1181	-20.66
40% CC Winter	0.6498	0.8373	0.1875	-28.85
60% CC Winter	0.6154	0.8588	0.2434	-39.55

The GOMS modelled fractional abundances had consistently higher levels of agreement with reference values obtained through maximum likelihood classification of nadir imagery for the datasets collected at a 30° IZA. In all but one case, the highest levels of agreement correspond to the simulated forests with the lowest canopy coverage. Overall, GOMS' ability to model fractional component abundances decreased as the forest coverage increased, as well as with an increase in IZA; a reasonable result considering the increased incidence and complexity of mutual shadowing at higher forest densities and larger IZAs..

5 DISCUSSION AND CONCLUSIONS

Any computational model which provides data used in high-level decision making should be thoroughly tested and validated. This project was undertaken primarily to assess the feasibility and utility of a laboratory-based forest simulation developed expressly to mimic, and correspondingly better understand the real-life implications of, the assumptions and conditions existing within the Li and Strahler (1992) GOMS model; a tool which has potential to provide important information which is used to determine environmental policy at the federal level. The explorative nature of the development of this project has dictated the necessity to keep the issues explored purposefully broad, as narrowing the scope to focus on any one particular subject would be sufficiently complex enough to warrant its own study. However, the internally consistent nature of this experimental setup can easily allow for any single variable to be isolated and studied future experiments in this or any similar physical computational forest simulation, which would be an ideal practice in future model validation and development.

5.1 Application of the Overlap Function Outside the Principal Plane

The modelled BRF values, as well as the patterns seen in the modelled BRF plots, at all angles outside the SPP in this implementation of the GOMS model are entirely dependent upon the geometric-optically calculated BRF values in the SPP due to their derivation via a diminutive linear response function based upon a given point's proximity to the SPP (Li & Strahler, 1992). Through analysis of the differences in the results derived from GOMS and spectrodirectional measurements, it is clear that the patterns in the measured BRF plot outside the SPP do not strictly follow a linear response pattern. Further, discrepancies between GOMS BRF and spectrogoniometer-derived HCRF values

along the SPP propagate further inconsistencies in GOMS' modelled BRFs outside the SPP. These findings suggest that the approach of using a linear response function to model reflectance values is one which is detrimental to the quality and accuracy of the modelled BRDF as a whole. For this reason, coupled with the increasing availability of data provided by multi-angular RS technologies such as goniometers and high-altitude multi-angular platforms capable of reliably collecting spectrodirectional data at specific locations, the benefits of using GOMS to calculate exact mutual shadowing overlap solutions at angular locations outside the SPP and PC becomes evident. An approximation of the overlap function was derived by Barker-Schaaff et al. (1994), in which an area correction factor is employed in order to approximate the overlap at viewing angles outside the SPP and PC without overestimating the overlap area. This approximation, while not as robust as an exact solution, would likely provide a significant improvement in modelled results outside the SPP over the current implementation.

5.2 Poisson-Disk Forest Distribution

The ideal characteristics of the FPD algorithm for forest distribution development were crucial to the success of this model validation project. FPD was able to generate a distribution where the random nature of a Poisson distribution holds, while the avoidance of issues such as crown overlap was achieved. Further, the ability of the FPD algorithm to provide a degree of spacing between tree stems may be even more highly representative of a true forest distribution than a classical Poisson distribution, due to its inherent ability to simulate the effects of inhibiting factors existing among adjacent trees, such as competition, which tend to provide a natural degree of spacing between forest stems (Franklin et al., 1985).

5.3 Target Rotational Variance

A lack of overall change in the major patterns in the HCRF plot following the rotation of the forest target by 90° indicates that the major drivers of the BRDF shape, specifically the shadow-hiding driven hot spot at the location of illumination, are not rotationally variant. However, subtle changes seen between the plots such as the extension of the hot spot indicate that the derived HCRF plots are, to a degree, affected by the locations of the individual trees in the forest distribution. Therefore, while there is a slight degree of rotational variance to the plots, this is driven solely by randomly occurring gaps forest distribution which align with the major axis of the sensor FOV at off-nadir VZAs. Given that these gaps tend to become filled with trees at higher forest densities, rotational variance subsequently will tend to decrease as forest crown closure increases. Because the higher forest densities have reduced odds of having one of these forest gaps, it follows the odds of overall disagreement between pairs of ULGS-2 and GOMS datasets is reduced as well. Implications of this are discussed in greater detail later in the chapter.

5.4 *A Priori* Information Requirements for Simulated Forest HCRF Plot Interpretation

Varying degrees of deviation from expected BRDF patterns were identified in all ULGS-2 datasets. Overall, these asymmetries were most highly prevalent at low forest coverage densities. In order to account for these deviations and properly interpret the BRDF surfaces derived from the ULGS-2 measurements, two major a-priori informational requirements were identified. The first is particularly useful to account for unexpected reflectance patterns along the orthogonal principal plane (OPP), and the second to account for unexpected reflectance patterns along the SPP.

5.4.1 Sunlit Component Material BRDF

The first requirement for proper interpretation of a simulated forest BRDF is an understanding of the individual BRDF of each sunlit component material at a given waveband. This includes both the anisotropic reflectance characteristics of the component material, as well as the magnitude of its sampled HCRF values. In this study, this requirement was achieved through spectrodirectional HCRF sampling of endmember panels with the ULGS-2 goniometer system. Through this practice, the reflectance characteristics of each of the two component materials could be isolated and investigated individually, enabling in particular the degree of forward-scattering or back-scattering characteristics demonstrated by each endmember material.

Unexpected patterns seen about the SPP at lower forest densities in the BRDF surfaces derived from ULGS-2 HCRF sampling primarily manifested in the form of a hotspot found centered along the SPP in the forward-scatter direction. Observed forward-scattering characteristics of the background material, combined with the disappearance of this phenomenon as forest crown closure increased, indicates that the cause would be the viewed sunlit background component; the abundance of which decreases with increases in forest crown closure. Investigation of the sunlit background material's BRDF showed forward-scattering properties that were largely specular in appearance, providing further evidence that the BRDF of the sunlit background is the cause of the unexpected asymmetry. Subtraction of the interpolated sunlit background BRDF surface from the low-crown closure forest BRDF surface was found to be able to reveal the expected BRDF patterns for an open forest when the material's forward-scattering influence was removed. This is illustrated in Figure 5.1:

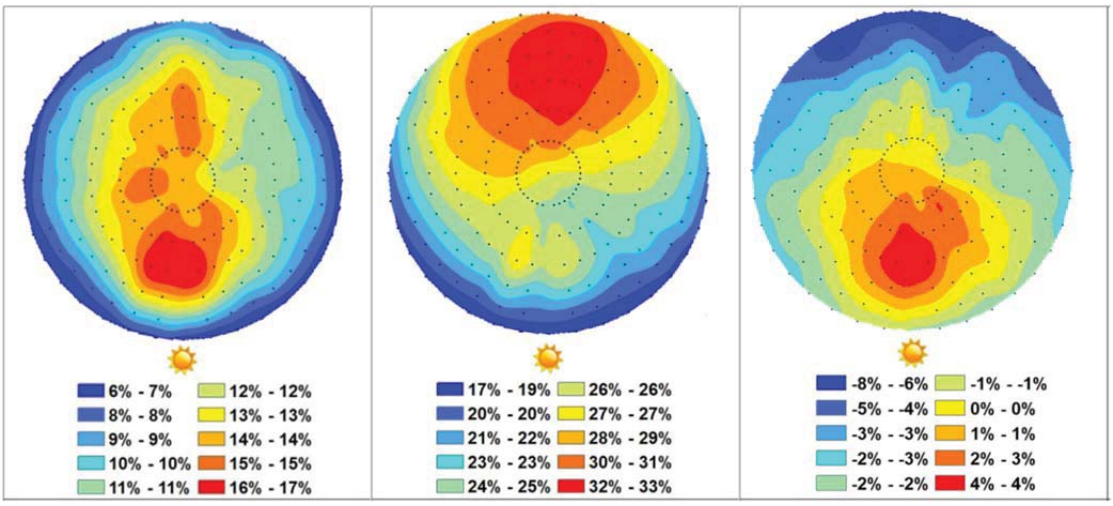

Figure 5.1: Efficacy of surface subtraction to reveal underlying reflectance patterns. Left panel shows HCRF plot for 20% crown closure forest at summer illumination location, with distinct forward-scattering patterns. Center panel shows HCRF plot of sunlit background component material, illustrating its forward-scattering properties. Right panel shows resultant HCRF plot after raster subtraction; unwanted forward-scattering is eliminated white the hot spot is retained.

Prior to performing HCRF plot surface subtraction, the background endmember surface values were divided by two in order to bring them to a magnitude similar to that of the forest dataset. The process of subtraction of the sunlit background HCRF plot surface from the individual forest HCRF plots was successful in revealing underlying plot patterns expected from these canopy surfaces. This practice of surface subtraction may be an important step to consider in potentially identifying underlying patterns in a HCRF plot surface that may be hidden by materials with non-ideal scattering characteristics used in the simulated forest.

Differences in magnitude in terms of sampled between the GOMS and ULGS-2 HCRF results were observed in a small number of low-crown closure forest datasets. The near-specular scattering characteristics of the background material resulted in sampled HCRF values of an unusually high magnitude; over 100% in the forward-scatter direction. This correspondence between differences in magnitude between ULGS-2 and

GOMS' reflectance values and viewed sunlit background leads to the disappearance of these differences in magnitude in sampled values with increase in forest crown closure. The net effect of these findings is a higher level of agreement between BRDF surfaces derived from ULGS-2 and GOMS at higher forest densities.

5.4.2 Distribution and Viewed Component Abundances

The second major a-priori informational requirement is an understanding of the viewed proportions of each forest component at every sampled viewing location in the goniometric hemisphere. This was accomplished through measurement of the FOV size at varying view angles and application of this understanding of FOV size and location to accomplish interpretation of what is falling within the FOV using digital photographs of the forest plot taken at corresponding viewing angles. Because the Poisson distribution arranges the individual trees randomly, any change in the forest distribution will change the viewed component abundances at any given viewing location.

When the 20% crown closure simulated forest was rotated 90° clockwise, subtle variations in the BRDF were visible, largely in the form of asymmetry about the SPP. Visual inspection of the simulated forest at viewing locations where the sampled reflectance values were higher than those at the corresponding location on the other side of the SPP showed that higher proportions of sunlit background were consistently aligned with the direction of the sensor FOV's major axis at these locations. It follows that, while subtle variation variations of reflectance anisotropy seen in the BRDF surfaces derived from the rotational variance test are visible, the overall magnitude and major patterns seen in the plots are caused solely by the change in individual tree locations in the forest

distribution, which in turn effect the amount of sunlit background available to be viewed by the sensor.

In a preliminary test devised to provide additional evidence toward the theory that the unexpected asymmetry about the SPP is directly caused by viewed sunlit background proportion, a randomly distributed forest plot was generated using the FPD algorithm with a linear gap in the forest distribution which would align with the sensor FOV's major axis at off-nadir VZAs. Subsequent derivation of a BRDF surface from the sampled points showed a bright spot in the BRDF which corresponds to the location where this linear forest gap was expected to align with the FOV's major axis. Following this finding, three individual trees were transported from one location in the background, where they were having little effect on the amount of viewed sunlit background, to locations where they would fill the forest gap as viewed by the ULGS-2 sensor from the location of the bright spot in the interpolated BRDF surface. The bright spot, as expected, disappeared; this effect can be seen in Figure 5.2:

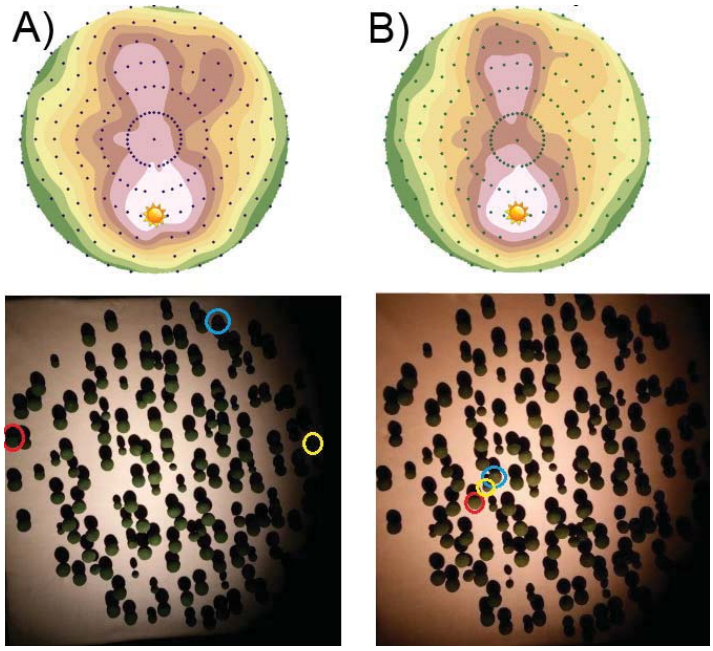

Figure 5.2: The computer-generated distribution at 40% crown closure (A) and an adjusted version (B) with three trees (circled in blue, red, and yellow, respectively) moved from the edge of the distribution to the location of a linear open area coinciding with the major axis of the FOV. As can be seen in the HCRF plots, this irregularity can be explained through the identification of the FOV size and location at a given viewing angle.

5.5 Assessment of GOMS, ULGS-2, PARABOLA-2, and MODIS BRDF Surfaces

The primary focus of this thesis, assessment of GOMS' ability to model open forest canopy characteristics by laboratory simulation, was supplemented with *in situ* data collected at the BOREAS SSA OJP site with the PARABOLA-2 goniometer system and data obtained via the MODIS BRDF product. This provides us with a preliminary glance at agreement between four different types of BRDF datasets for a single open forest location; two within a downscaled laboratory simulation, and two related to data collected or derived from measurements of the actual OJP flux tower location, as seen n Figure 5.3.

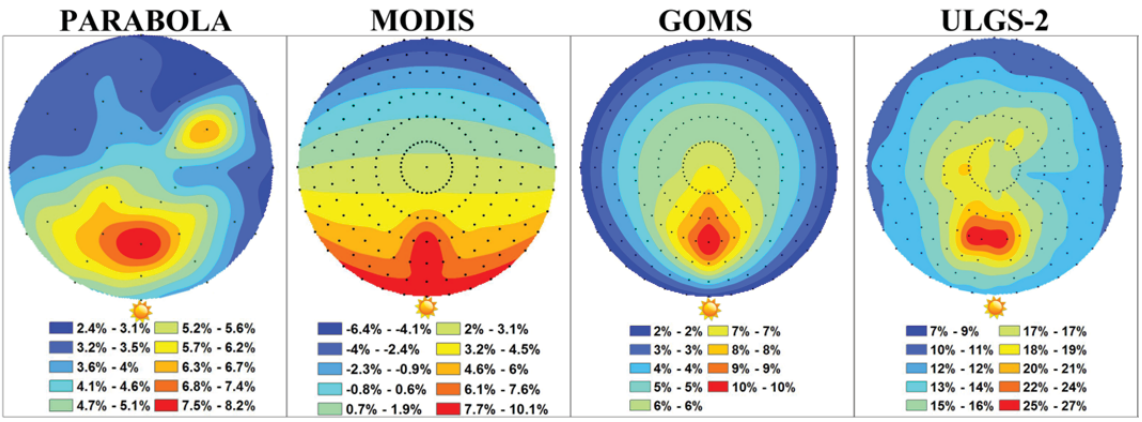

Figure 5.3: Comparison of four derived BRDF surfaces

The GOMS, ULGS-2, and PARABOLA-2 BRDF surfaces show high levels of agreement in their reflectance anisotropy characteristics. In contrast, the results obtained from the MODIS BRDF product and the AMBRALS modelling framework was unsuccessful in properly delineating the hot spot. This discrepancy from the other datasets indicates further study of the RTLSR model itself, as well as its implementation in the AMBRALS model framework. Disagreement between the patterns seen PARABOLA-2 dataset and the other datasets may be explained by the discrepancy between the date and time of the data collection of the PARABOLA-2 data and the date and time corresponding to the laboratory, GOMS, and MODIS datasets; which are nearly a month apart.

The magnitude and range of the GOMS modelled reflectance values are very similar to those within the PARABOLA-2 dataset. This high level of agreement in reflectance values between *in situ* PARABOLA-2 and GOMS data provides indication that it is indeed the ULGS-2's sampled reflectance values that are unrealistic in terms of a true open forest, and not the output of the GOMS Model itself. This result provides further indication that robust model validation is possible using the techniques outlined in this thesis, provided that the materials used have suitable bidirectional reflectance

characteristics. The negative values obtained using MODIS' BRDF parameters product with the AMBRALS modelling framework are an indication of problems with either the RTLSR model or the AMBRALS framework itself, a result warranting further study.

5.6 On the Use Of a Three Component Model

The necessity of using a Four Component model is entirely dependent upon comparison of the spectra of the two different shadow endmember components. In the case of this experiment, while the spectra of the two different sunlit endmembers varied greatly under fully illuminated conditions, the spectra of the shadow endmembers showed a negligible difference when converted to reflectance. Therefore, based on the materials used in the construction of this model forest and the illumination conditions utilized in this experiment, it was deemed reasonable to use a three component version of the GOMS model. However, this may not be the case in all laboratory situations, and can vary based on the spectral properties of the construction materials as well as the intensity and spectral characteristics of the illumination source. Therefore, the ability to use a three component model must be studied on a case-by-case basis.

5.7 Mitigation of Error Sources

Identified sources of error are various. As discussed earlier in this thesis, some limitations related to laboratory conditions contributed as sources of error. These limitations are primarily related to variable brightness across the target area. This type of error is difficult to mitigate, but one possible solution would involve using a more powerful illumination source positioned much further from the target, reducing the effect of the inverse square law upon brightness at points on sides of the plot both closer and further from the illumination source. Other error sources are related to departures from

assumptions in the GOMS model in the physical forest simulation due to impracticality in perfectly following all assumptions. In the physical forest simulation, the trees have stems which cast shadows. The absence of stems, and subsequently shadows cast by them, in GOMS is an assumption which unavoidably must be violated in this type of simulation. The relatively rough texture of the flocking material has been seen to cause microshadowing effects, which would not occur upon a surface with Lambertian characteristics, as the trees in the GOMS model are assumed to have. Further laboratory testing of other inexpensive materials which may be suitable for the purpose of designing the type of physical forest simulation described in this thesis could yield the identification of a more suitable material for this purpose. The same logic can be applied to the background material as well. It may be possible to implement parameters into the model software such as stems and their shadows, the implementation of which in itself could be validated using spectrodirectional measurements of a physical forest simulation; this feedback loop of adjusting both the physical simulation and the computational model would be a useful practice in optimizing both tools.

5.8 3D Printing in Geometric-Optical CRM Studies

It is important to note that the model trees created for this project were shaped by hand. While this allowed for the model trees to be developed to the specifications required for this thesis without the use of specialized equipment, the tolerances for the structural parameters of each individual tree are quite low due to imperfections in the trees introduced during the sculpting phase, such as flat sections or divots which prevent the trees from being perfectly shaped spheroids, as is specified in the GOMS model.

While in the past it would have been extremely expensive and impractical to acquire hardware capable of mass-producing model trees with structural tolerance levels sufficiently high to perform robust validation studies using the laboratory techniques outlined in this thesis, the recent commercialization of additive manufacturing machines (also known as 3D printers) have paved the way for these highly robust validation studies to be performed. Not only can model trees now be mass-produced with shapes and dimensions that are nearly perfect and accurate to a much higher level of precision than would be possible to do by hand, but large assemblages of identically sized model trees can now also be developed, allowing for testing of the implications of the different GOMS model cases described in chapter 2 of this thesis. These practically identical assemblages of trees can be created with slightly varying structural characteristics, allowing for robust validation of the effects of subtle variations in individual trees in a canopy to be performed.

Beyond the aforementioned advantages of 3D printing in geometric-optical spectrodirectional studies, it is potentially possible to scan a real-world scene with currently available LIDAR systems, model that scene in a computer, scale it down, and subsequently print the entire scene within a 3D printer. This potentially allows for transportability of real-world scenes into a laboratory environment where they can be rigorously studied in controlled conditions. Fusion of these technologies and transportability of a scene from the real-world to the laboratory could potentially allow for future end-to-end validation of geometric-optical canopy reflectance models.

5.9 Recommendations for Future Research

Recommendations for future work based on the work completed to date are as follows:

- Expansion of the number of angular locations at which exact mutual shadowing overlap calculations are performed through geometric-optical means is expanded to match the angular resolution sampled with spectrodirectional measurements. This is suggested in favor of the current implementation of a linear response function in BRF calculations outside the SPP in GOMS.
- The potential of this physical forest simulation to be utilized as a visualization tool in the context of education about geometric-optical models is a concept worth evaluating.
- Collection of data using a simulated model forest of a smaller scale would allow for use of an illumination source with a narrower beam width, which could potentially allow for data collection throughout the entire hemisphere, including the 10° of azimuthal data in the SPP which was impossible to collect due to the relatively wide illumination source used in this study, and the occlusionary effects upon the target due to shadow diffraction as the goniometer arc entered the beam. This 10° of missing data could provide important information regarding data collected near the hot spot which is currently unavailable due to shadowing of the target by the goniometer's arch. One possibility for obtaining these crucial missing sample locations outside of the exact hot spot location would be to use an arc-free goniometer design, such as a sensor mounted on an unmanned aerial vehicle (UAV).

- Data collection for the physical forest simulation in natural, outdoor light conditions is suggested, as it would provide another direct linkage between this laboratory study and the current literature in which the GOMS model has been applied to imagery collected by aerial and satellite platforms in natural outdoor light conditions; facilitating model validation studies.
- Implementation of a physical forest model background which simulates the conditions of the Boreal forest in winter (i.e. simulating a snow-covered background) would be useful to investigate its effect on GOMS results for data collected by airborne and satellite spectrodirectional platforms in conditions where snow cover is present on the ground. Similarly, a background could be implemented to study the effects of a controlled background burn upon GOMS results by implementing actual burned vegetation; the resultant expected similarity between shadow and sunlit background spectra in this situation may have unknown consequences on model results.
- Simulation of high-relief terrain through implementation a physical forest model featuring variable background slope and aspect parameters in order to investigate their effect upon GOMS modelled results is recommended, provided that care is taken to simulate the process wherein trees grow perpendicular to the Earth's geoid.
- Comparison of these results to those obtained from the implementation of a four-component model could be useful in understanding the implications of using the simplified three-component model.

- Utilize data processing automation tools developed in this thesis in support of development of processing pipeline which can be used for big data analytics.
- Implement, and subsequently validate, mitigating factors to reduce differences between GOMS' computational model and the physical forest simulation.
- Use 3D printing technology to allow for assemblages of model trees to be developed with much higher tolerances than would be possible by hand.
- Use 3D printing further to create entire assemblages of identically shaped trees, each assemblage with a slightly different structural parameter value, to allow for robust validation of the GOMS canopy reflectance model
- Utilize a combination of LIDAR and 3D printing technology to work toward perfecting transportability of an outdoor forest scene into the laboratory, where an outdoor Landsat pixel-scale scene can be physically scaled down and placed under a goniometer to work toward an eventual end-to-end validation technique for GOMS.
- Apply the methods from this study on more complex CRMs, such as those which implement radiative transfer. This may potentially be accomplished using 3D printing, but it's possible other technologies may perform better for this practical purpose.

5.10 Conclusions

A laboratory-based spectrodirectional validation study of the GOMS CRM was undertaken using a specialized forest simulation. The ultimate goal in the development of this laboratory simulation experiment is to develop an environment wherein the variables and mechanisms involved in the derivation of GOMS simulated results can be isolated

and investigated. This type of simulation is capable of evaluating how well a theoretical model such as GOMS is able to simulate real-life conditions, a fundamental step in validation of a physically-based computational model. While the mechanisms driving the results obtained from this experiment are not the exact same mechanisms driving results found in a real open tree canopy, highly valuable information can be obtained by understanding these mechanisms, as well as and the differences between the simulated canopy and a real tree canopy. A method of direct comparison between geometric-optical modelled BDRF surface and measured HCRF surface over an entire hemisphere has been described, and has been shown to be a demonstrably useful practice in CRM validation studies.

CRMs require robust validation to ensure high quality data product production, and the RS goniometer systems used in a controlled laboratory environment can facilitate this requirement. The ability of this spectrodirectional RS laboratory experiment to facilitate the understanding of the factors driving the anisotropic reflectance characteristics of canopy surfaces, as well as to study the implications of CRM assumptions, has been demonstrated in this study. With the increasing prevalence and availability of goniometer systems, as well as 3D printers capable of developing physical forest models with high-precision, the methods utilized in this study have the potential to be applied to more complex CRMs. With their ability to remove bidirectional effects from nadir imagery and derive vegetative canopy structural parameters, spectrodirectional RS and CRMs have the potential to revolutionize the field of RS by providing the information required for superior, more consistent data products.

REFERENCES

Abuelgasim, A. A., & Strahler, A. H. (1994). Modeling bidirectional radiance measurements collected by the advanced Solid-State Array Spectroradiometer (ASAS) over oregon transect conifer forests. *Remote Sensing of Environment, 47*(2), 261-275. doi:10.1016/0034-4257(94)90160-0

Adams, J. B., Smith, M. O., & Gillespie, A. R. (1993). Imaging spectroscopy: interpretation based on spectral mixture analysis. *Imaging spectroscopy: interpretation based on spectral mixture analysis, 7*.

Agapiou, A., Hadjimitsis, D. G., & Alexakis, D. D. (2012). Evaluation of Broadband and Narrowband Vegetation Indices for the Identification of Archaeological Crop Marks. *Remote Sensing, 4*(12), 3892-3919. doi:10.3390/rs4123892

Asner, G. P. (1998). Biophysical and Biochemical Sources of Variability in Canopy Reflectance. *Remote Sensing of Environment, 64*(3), 234-253. doi:10.1016/s0034-4257(98)00014-5

Asner, G. P., Braswell, B. H., & Schimel, D. S. (1998). Ecological Research Needs From Multiangle Remote Sensing Data. *Remote Sensing of Environment, 63*(2).

Baldridge, A., Hook, S., Grove, C., & Rivera, G. (2009). The ASTER spectral library version 2.0. *Remote Sensing of Environment, 113*(4), 711-715.

Barnsley, M. J., Strahler, A. H., Morris, K. P., & Muller, J. P. (1994). Sampling the surface bidirectional reflectance distribution function (BRDF): 1. Evaluation of current and future satellite sensors. *Remote Sensing Reviews, 8*(4).

Birdsey, R. A. (1992). Carbon storage and accumulation in United States forest ecosystems.

Bridson, R. (2007). Fast Poisson disk sampling in arbitrary dimensions. *Fast Poisson disk sampling in arbitrary dimensions*.

Brown, S. (2002). Measuring Carbon in Forests: Current Status and Future Challenges. *Environmental Pollution, 116*(3). doi:10.1016/S0269-7491(01)00212-3

Bruegge, C. J., Helmlinger, M. C., Conel, J. E., Gaitley, B. J., & Abdou, W. A. (2000). PARABOLA III: A sphere-scanning radiometer for field determination of surface anisotropic reflectance functions. *Remote Sensing Reviews, 19*(1-4), 75-94.

Buchhorn, M., Petereit, R., & Heim, B. (2013). A Manual Transportable Instrument Platform for Ground-Based Spectro-Directional Observations (ManTIS) and the Resultant Hyperspectral Field Goniometer System. *Sensors, 13*(12). doi:10.3390/s131216105

Christensen, J. H., Hewitson, B., Busuioc, A., Chen, A., Gao, X., Held, R., . . . Laprise, R. (2007). Regional climate projections. *Climate Change, 2007: The Physical Science Basis. Contribution of Working group I to the Fourth Assessment Report of the Intergovernmental Panel on Climate Change, University Press, Cambridge, Chapter 11*, 847-940.

Coburn, C. A., Gaalen, E., Peddle, D. R., & Flanagan, L. B. (2010). Anisotropic reflectance effects on spectral indices for estimating ecophysiological parameters using a portable goniometer system. *Canadian Journal of Remote Sensing, 36*(sup2). doi:10.5589/m10-066

Coburn, C. A., & Noble, S. D. (2009). ULGS II: A High-Performance Field and Laboratory Spectrogoniometer for Measuring Hyperspectral Bidirectional Reflectance Characteristics. *ULGS II: A High-Performance Field and Laboratory Spectrogoniometer for Measuring Hyperspectral Bidirectional Reflectance Characteristics*. doi:10.1109/TGRS.2015.2499245

Coburn, C. A., & Noble, S. D. (2016). ULGS II: A High-Performance Field and Laboratory Spectrogoniometer for Measuring Hyperspectral Bidirectional Reflectance Characteristics. *IEEE Transactions on Geoscience and Remote Sensing, 54*(4), 2304-2313.

Coburn, C. A., & Peddle, D. R. (2006). A low-cost field and laboratory goniometer system for estimating hyperspectral bidirectional reflectance. *A low-cost field and laboratory goniometer system for estimating hyperspectral bidirectional reflectance*. doi:10.5589/m06-021

Cracknell, A. P. (1998). Review article Synergy in remote sensing-what's in a pixel? *Review article Synergy in remote sensing-what's in a pixel?* doi:10.1080/014311698214848

Deering, D. W., & Eck, T. F. (1999). *BOREAS RSS-01 PARABOLA SSA Surface Reflectance and Transmittance Data*. Retrieved from: https://doi.org/10.3334/ORNLDAAC/286

Deering, D. W., & Leone, P. (1986). A sphere-scanning radiometer for rapid directional measurements of sky and ground radiance. *Remote Sensing of Environment, 19*(1), 1-24. doi:10.1016/0034-4257(86)90038-6

Dennison, P. E., & Roberts, D. A. (2003). Endmember selection for multiple endmember spectral mixture analysis using endmember average RMSE. *Remote Sensing of Environment, 87*(2-3), 123-135. doi:10.1016/s0034-4257(03)00135-4

Desai, A. (2008). Graphics Primitives. *PHI Learning Pvt. Ltd*.

Elachi, C., & Van Zyl, J. J. (2006). Fundamental Properties of Electromagnetic Waves. *John Wiley & Sons*.

Fisher, P. (1997). The pixel: A snare and a delusion. *International Journal of Remote Sensing, 18*(3), 679-685. doi:10.1080/014311697219015

Fournier, R. A., Luther, J. E., Guindon, L., Lambert, C. M., Piercey, D., Hall, R. J., & Wulder, M. A. (2003). Mapping aboveground tree biomass at the stand level from inventory information: test cases in Newfoundland and Quebec. *Canadian Journal of Forest Research, 33*(10), 1846-1863. doi:10.1139/x03-099

Franklin, J., Michaelsen, J., & Strahler, A. H. (1985). Spatial analysis of density dependent pattern in coniferous forest stands. *Spatial analysis of density dependent pattern in coniferous forest stands*. doi:10.1007/bf00033451

Franklin, S. E., & Wulder, M. A. (2002). Remote sensing methods in medium spatial resolution satellite data land cover classification of large areas. *Remote sensing methods in medium spatial resolution satellite data land cover classification of large areas*. doi:10.1191/0309133302pp332ra

Fu, Z., Wang, J., Song, J. L., Zhou, H. M., Pang, Y., & Chen, B. S. (2011). Estimation of forest canopy leaf area index using MODIS, MISR, and LiDAR observations. *Journal of Applied Remote Sensing, 5*(1), 53530. doi:10.1117/1.3594171

Gao, X., Huete, A. R., Ni, W., & Miura, T. (2000). Optical–Biophysical Relationships of Vegetation Spectra without Background Contamination. *Remote Sensing of Environment, 74*(3), 609-620. doi:10.1016/s0034-4257(00)00150-4

Gates, D. M., Keegan, H. J., Schlester, J. C., & Weidner, V. R. (1965). Spectral properties of plants. *Applied Optics, 4*(1).

Gibbs, D. P., Betty, C. L., Fung, A. K., Blanchard, A. J., Irons, J. R., & Balsam, W. L. (1993). Automated measurement of polarized bidirectional reflectance. *Remote Sensing of Environment, 43*(1), 97-114. doi:10.1016/0034-4257(93)90067-8

Goel, N. S. (1988). A perspective on vegetation canopy reflectance models. *A perspective on vegetation canopy reflectance models*.

Goward, S. N., Huemmrich, K. F., & Waring, R. H. (1994). Visible-near infrared spectral reflectance of landscape components in western Oregon. *Remote Sensing of Environment, 47*(2), 190-203. doi:10.1016/0034-4257(94)90155-4

Green, R. O., Conel, J. E., Carrere, V., Bruegge, C. J., Margolis, J. S., Rast, M., & Hoover, G. (1991). Determination of the in-flight spectral and radiometric characteristics of the Airborne Visible/Infrared Imaging Spectrometer (AVIRIS). *Imaging Spectrosocopy: Fundamentals and Prospective Applications*, 103-123.

Griggs, D. J., & Noguer, M. (2002). Climate change 2001: the scientific basis. Contribution of working group I to the third assessment report of the intergovernmental panel on climate change. *Weather, 57*(8), 267-269.

Grum, F., & Becherer, R. J. (1979). Optical radiation measurements. Volume 1 - Radiometry. *Academic Press, Inc*.

Hall, F. G. (1999). Introduction to special section: BOREAS in 1999: Experiment and science overview. *Journal of Geophysical Research: Atmospheres, 104*(D22), 27627-27639.

Hall, F. G., Knapp, D. E., & Huemmrich, K. F. (1997). Physically based classification and satellite mapping of biophysical characteristics in the southern boreal forest. *Journal of Geophysical Research: Atmospheres (1984–2012), 102*(D24), 29567-29580. doi:10.1029/97jd02578

Hapke, B., DiMucci, D., Nelson, R., & Smythe, W. (1996). The cause of the hot spot in vegetation canopies and soils: Shadow-hiding versus coherent backscatter. *The cause of the hot spot in vegetation canopies and soils: Shadow-hiding versus coherent backscatter*.

Hosgood, B., Piironen, J., & Andreoli, G. (2000). Goniometers. *Goniometers*. doi:10.1002/047134608x.w3910

Huete, A., Miura, T., Yoshioka, H., Ratana, P., & Broich, M. (2014). Indices of vegetation activity. *Springer Berlin Heidelberg*.

IPCC. (2015). *Climate change 2014: mitigation of climate change* (Vol. 3): Cambridge University Press.

Jenks, G. F., & Coulson, M. R. (1963). *Class intervals for statistical maps*: C. Bertelsmann.

Jensen, J. R. (2007). Multispectral Remote Sensing Systems. *Pearson Education*.

Jensen, J. R. (2009). *Remote sensing of the environment: An earth resource perspective 2/e*: Pearson Education India.

Johnson, R. L., Peddle, D. R., & Hall, R. J. (2000). A modeled-based sub-pixel scale mountain terrain normalization algorithm for improved LAI estimation from airborne casi imagery. *Proceedings of the 22nd Canadian Symposium on Remote Sensing, Victoria, BC*.

Kavzoglu, T. (2004). Simulating Landsat ETM+ imagery using DAIS 7915 hyperspectral scanner data. *International Journal of Remote Sensing, 25*(22), 5049-5067. doi:10.1080/01431160410001720199

Keshava, N., & Mustard, J. F. (2002). Spectral Unmixing. *Signal Processing Magazine, 19(1)*.

Kimes, D. S. (1983). Dynamics of directional reflectance factor distributions for vegetation canopies. *Dynamics of directional reflectance factor distributions for vegetation canopies*.

Koechler, C., Hosgood, B., & Andreoli, G. (1994). The European optical goniometric facility: Technical description and first experiments on spectral unmixing. *The European optical goniometric facility: Technical description and first experiments on spectral unmixing*. doi:10.1109/igarss.1994.399742

Kumar, L., Schmidt, K., Dury, S., & Skidmore, A. (2001). Imaging Spectrometry and Vegetation Science. *Springer Netherlands*.

Kuusk, A. (1991). The Hot Spot Effect in Plant Canopy Reflectance. *Springer Berlin Heidelberg*.

Lacaze, R., Chen, J. M., Roujean, J. L., & Leblanc, S. G. (2002). Retrieval of vegetation clumping index using hot spot signatures measured by POLDER instrument. *Remote Sensing of Environment, 79*(1).

Li, C., Song, J., & Wang, J. (2015). Modifying Geometric-Optical Bidirectional Reflectance Model for Direct Inversion of Forest Canopy Leaf Area Index. *Remote Sensing, 7*(9), 11083-11104. doi:10.3390/rs70911083

Li, X., & Strahler, A. (1985). Geometric-Optical Modeling of a Conifer Forest Canopy. *IEEE Transactions on Geoscience and Remote Sensing, GE-23*(5), 705-721. doi:10.1109/tgrs.1985.289389

Li, X., & Strahler, A. (1986). Geometric-Optical Bidirectional Reflectance Modeling of a Conifer Forest Canopy. *IEEE Transactions on Geoscience and Remote Sensing, GE-24*(6), 906-919. doi:10.1109/tgrs.1986.289706

Li, X., & Strahler, A. (1992). Geometric-optical bidirectional reflectance modeling of the discrete crown vegetation canopy: effect of crown shape and mutual shadowing. *IEEE Transactions on Geoscience and Remote Sensing, 30*(2). doi:10.1109/36.134078

Li, X., Wang, J., Hu, B., & Strahler, A. H. (1998). On utilization of a-priori knowledge in inversion of remote sensing models. *Science in China Series D: Earth &*. doi:10.1007/BF02878739

Liang, S., Strahler, A. H., Barnsley, M. J., Borel, C. C., Gerstl, S. A. W., Diner, D. J., . . . Walthall, C. L. (2000). Multiangle remote sensing: Past, present and future. *Remote Sensing Reviews, 18*(2-4), 83-102. doi:10.1080/02757250009532386

Ma, H., Song, J., Wang, J., Xiao, Z., & Fu, Z. (2014). Improvement of spatially continuous forest LAI retrieval by integration of discrete airborne LiDAR and remote sensing multi-angle optical data. *Agricultural and Forest Meteorology, 189-190*, 60-70. doi:10.1016/j.agrformet.2014.01.009

Mack, P. E. (1990). *Viewing the Earth: The social construction of the Landsat satellite system*: MIT Press.

Mahajan, V. N. (2014). Radiometry of Point Object Imaging. *SPIE Press*.

Mars, R. (2016). 99% Invisible. *America's Last Top Model*. Retrieved from 99% Invisible website: http://99percentinvisible.org/episode/americas-last-top-model

Martonchik, J. V., Diner, D. J., Pinty, B., Verstraete, M. M., Myneni, R. B., Knyazikhin, Y., & Gordon, H. R. (1998). Determination of land and ocean reflective, radiative, and biophysical properties using multiangle imaging. *IEEE Transactions on Geoscience and Remote Sensing, 36*(4), 1266-1281. doi:10.1109/36.701077

Maselli, F. (2004). Monitoring forest conditions in a protected Mediterranean coastal area by the analysis of multiyear NDVI data. *Remote Sensing of Environment, 89*(4), 423-433. doi:10.1016/j.rse.2003.10.020

McCullough, D., Werner, R., & Neumann, D. (1998). Fire and Insects in Northern and Boreal Forest Ecosystems of North America 1. *Annual Review of Entomology, 43*(1). doi:10.1146/annurev.ento.43.1.107

Miller, J. R., Wu, J., Boyer, M. G., Belanger, M., & Hare, E. W. (1991). Seasonal patterns in leaf reflectance red-edge characteristics. *International Journal of Remote Sensing, 12*(7).

Mkhabela, Bullock, P., Raj, S., Wang, S., & Yang, Y. (2011). Crop yield forecasting on the Canadian Prairies using MODIS NDVI data. *Agricultural and Forest Meteorology, 151*(3), 385-393. doi:10.1016/j.agrformet.2010.11.012

Morison, M., Cloutis, E., & Mann, P. (2014). Spectral unmixing of multiple lichen species and underlying substrate. *International Journal of Remote Sensing, 35*(2). doi:10.1080/01431161.2013.871085

Myneni, R. B., Ross, J., & Asrar, G. (1989). A review on the theory of photon transport in leaf canopies. *Agricultural and Forest Meteorology, 45*(1).

Myneni, R. B., & Williams, D. L. (1994). On the relationship between FAPAR and NDVI. *Remote Sensing of Environment, 49*(3), 200-211. doi:10.1016/0034-4257(94)90016-7

Nicodemus, F. E. (1965). Directional Reflectance and Emissivity of an Opaque Surface. *Applied Optics, 4*(7).

Nicodemus, F. E., Richmond, J. C., Hsia, J. J., & Ginsberg, I. W. (1977). Geometrical considerations and nomenclature for reflectance. *Geometrical considerations and nomenclature for reflectance*.

Palmer, J. M., & Grant, B. G. (2010). The Art of Radiometry. *SPIE Press*.

Patenaude, G., Milne, R., & Dawson, T. P. (2005). Synthesis of remote sensing approaches for forest carbon estimation: reporting to the Kyoto Protocol. *Environmental Science & Policy, 8*(2), 161-178.

Peddle, D., Boon, S., Glover, A., & Hall, F. (2010). Forest structure without ground data: Adaptive Full-Blind Multiple Forward-Mode reflectance model inversion in a mountain pine beetle damaged forest. *International Journal of Remote Sensing, 31*(8). doi:10.1080/01431160903401361

Peddle, D., Franklin, S., Johnson, R., Lavigne, M., & Wulder, M. (2003). Structural change detection in a disturbed conifer forest using a geometric optical reflectance model in multiple-forward mode. *IEEE Transactions on Geoscience and Remote Sensing, 41*(1). doi:10.1109/TGRS.2002.807756

Peddle, D., Johnson, R., Cihlar, J., & Latifovic, R. (2004). Large area forest classification and biophysical parameter estimation using the 5-Scale canopy reflectance model in Multiple-Forward-Mode. *Remote Sensing of Environment, 89*(2). doi:10.1016/j.rse.2002.08.001

Peddle, D., White, H., Soffer, R., Miller, J., & LeDrew, E. (2001a). Reflectance processing of remote sensing spectroradiometer data. *Computers & Geosciences, 27*(2). doi:10.1016/S0098-3004(00)00096-0

Peddle, D. R., Brunke, S. P., & Hall, F. G. (2001b). Comparison of Spectral Mixture Analysis and Ten Vegetation Indices for Estimating Boreal Forest Biophysical information from Airborne Data: Remote Sensing and Spatial Data Integration: Measuring, Monitoring, and Modelling. *Canadian Journal of Remote Sensing, 27*(6).

Peddle, D. R., Hall, F. G., & LeDrew, E. F. (1999). Spectral Mixture Analysis and Geometric-Optical Reflectance Modeling of Boreal Forest Biophysical Structure. *Remote Sensing of Environment, 67*(3), 288-297. doi:10.1016/s0034-4257(98)00090-x

Peddle, D. R., & Smith, A. M. (2005). Spectral mixture analysis of agricultural crops: Endmember validation and biophysical estimation in potato plots. *International Journal of Remote Sensing, 26*(22), 4959-4979. doi:10.1080/01431160500213979

Pilger, N., Peddle, D. R., & Luther, J. E. (2002). Estimation of forest cover type and structure from Landsat TM imagery using a canopy reflectance model for biomass mapping in Western Newfoundland. *Geoscience and Remote Sensing Symposium, 2002. IGARSS'02. 2002 IEEE International, 3*. doi:10.1109/IGARSS.2002.1026103

Prasad, S., Bruce, L. M., & Chanussot, J. (2011). Optical Remote Sensing: Advances in Signal Processing and Exploitation Techniques. *Optical Remote Sensing: Advances in Signal Processing and Exploitation Techniques*.

Pu, R., & Gong, P. (2011). Hyperspectral Remote Sensing of Vegetation Parameters. *Taylor & Francis Group.*

Purkis, S. J., & Klemas, V. V. (2011). *Remote sensing and global environmental change*: John Wiley & Sons.

Research, B. (2016). Remote Sensing Industry Expanding Commercial Opportunities [Press release]. Retrieved from http://www.bccresearch.com/pressroom/ias/remote-sensing-industry-expanding-commercial-opportunities

Roberts, D. A., Smith, M. O., Sabol, D. E., Adams, J. B., & Ustin, S. (1992). Mapping the spectral variability in photosynthetic and non-photosynthetic vegetation, soils and shade using AVIRIS. *Annual JPL Airborne Geoscience Workshop, 3*.

Roberts, D. A., Ustin, S. L., Ogunjemiyo, S., Greenberg, J., Dobrowski, S. Z., Chen, J., & Hinckley, T. M. (2004). Spectral and Structural Measures of Northwest Forest Vegetation at Leaf to Landscape Scales. *Ecosystems, 7*(5). doi:10.1007/s10021-004-0144-5

Robinson, B., & Biehl, L. (1979). *Calibration procedures for measurement of reflectance factor in remote sensing field research.* Paper presented at the 23rd Annual Technical Symposium.

Roujean, J. L., Leroy, M., & Deschamps, P. Y. (1992). A bidirectional reflectance model of the Earth's surface for the correction of remote sensing data. *Journal of Geophysical Research: Atmospheres, 97*(D18), 20455-20468.

Rouse, J. W. J., Haas, R., Schell, J., & Deering, D. (1974). Monitoring vegetation systems in the Great Plains with ERTS. *NASA special publication, 351*, 309.

Roy, D. P., Wulder, M., Loveland, T., Woodcock, C., Allen, R., Anderson, M., . . . Kennedy, R. (2014). Landsat-8: Science and product vision for terrestrial global change research. *Remote Sensing of Environment, 145*, 154-172.

Running, S. W., & Nemani, R. R. (1988). Relating seasonal patterns of the AVHRR vegetation index to simulated photosynthesis and transpiration of forests in different climates. *Relating seasonal patterns of the AVHRR vegetation index to simulated photosynthesis and transpiration of forests in different climates*.

Sandmeier, S., & Deering, D. W. (1999). Structure Analysis and Classification of Boreal Forests Using Airborne Hyperspectral BRDF Data from ASAS. *Remote Sensing of Environment, 69*(3), 281-295. doi:10.1016/s0034-4257(99)00032-2

Sandmeier, S., & Itten, K. (1999). A field goniometer system (FIGOS) for acquisition of hyperspectral BRDF data. *IEEE Transactions on Geoscience and Remote Sensing, 37*(2). doi:10.1109/36.752216

Sandmeier, S., Müller, C., Hosgood, B., & Andreoli, G. (1998). Physical Mechanisms in Hyperspectral BRDF Data of Grass and Watercress. *Remote Sensing of Environment, 66*(2), 222-233. doi:10.1016/s0034-4257(98)00060-1

Sandmeier, S. R. (2000). Acquisition of bidirectional reflectance factor data with field goniometers. *Remote Sensing of Environment, 73*(3), 257-269.

Sandmeier, S. R., & Strahler, A. H. (2000). BRDF laboratory measurements. *Remote Sensing Reviews, 18*(2-4), 481-502. doi:10.1080/02757250009532398

Schaaf, C., & Strahlerl, A. (1994). Validation of bidirectional and hemispherical reflectances from a geometric-optical model using ASAS imagery and pyranometer measurements of a spruce forest. *Remote Sensing of Environment, 49*(2). doi:10.1016/0034-4257(94)90050-7

Schaaf, C. B., Li, X., & Strahler, A. H. (1994). Topographic effects on bidirectional and hemispherical reflectances calculated with a geometric-optical canopy model. *IEEE Transactions on Geoscience and Remote Sensing, 32*(6), 1186-1193. doi:10.1109/36.338367

Schaaf, C. B., & Strahler, A. H. (1993). Modeling the bidirectional reflectance and spectral albedo of a conifer forest. *Modeling the bidirectional reflectance and spectral albedo of a conifer forest*.

Schaepman-Strub, G., Schaepman, M. E., Painter, T. H., Dangel, S., & Martonchik, J. V. (2006). Reflectance quantities in optical remote sensing definitions and case studies. *Remote Sensing of Environment, 103*(1). doi:10.1016/j.rse.2006.03.002

Schaepman, M. E. (2007). Spectrodirectional remote sensing: From pixels to processes. *International Journal of Applied Earth Observation and Geoinformation, 9*(2), 204-223. doi:10.1016/j.jag.2006.09.003

Schott, J. R., & Schott, J. (2009). Fundamentals of Polarimetric Remote Sensing. *spie*. doi:10.1117/3.817304.ch5

Sellers, P., Hall, F., Ranson, K. J., Margolis, H., Kelly, B., Baldocchi, D., . . . Goodison, B. (1995). The boreal ecosystem-atmosphere study (BOREAS): an overview and early results from the 1994 field year. *Bulletin of the American Meteorological Society, 76*(9), 1549-1577.

Soenen, S., Peddle, D., Hall, R., Coburn, C., & Hall, F. (2010). Estimating aboveground forest biomass from canopy reflectance model inversion in mountainous terrain. *Remote Sensing of Environment, 114*(7). doi:10.1016/j.rse.2009.12.012

Soffer, R. (1995). Bidirectional Reflectance Factors of an Open Tree Canopy by Laboratory Simulation. *York University*.

Strahler, A. H. (1997). Vegetation Canopy Reflectance Modeling Recent Developments and Remote Sensing Perspectives. *Remote Sensing Reviews, 15*(1-4).

Strahler, A. H., & Jupp, D. L. B. (1990). Modeling bidirectional reflectance of forests and woodlands using boolean models and geometric optics. *Remote Sensing of Environment, 34*(3), 153-166. doi:10.1016/0034-4257(90)90065-t

Strahler, A. H., Muller, J., Lucht, W., Schaaf, C., Tsang, T., Gao, F., . . . Barnsley, M. J. (1999). MODIS BRDF/albedo product: algorithm theoretical basis document version 5.0. *MODIS documentation, 23*(4), 42-47.

Sugianto, R. M., & Laffan, S. (2004). Overview of CHRIS PROBA mission - Multi-Angle Hypserspectral Remote Sensing and Its Application to Agriculture. *New Development and Applications for Imagery Conference, TS 22.2.*

Suits, G. H. (1973). The Calculation of the Directional Reflectance of a Vegetative Canopy. *Remote Sensing of Environment, 2.*

Suits, G. H. (1983). The Nature of Electromagnetic Radiation. *The Nature of Electromagnetic Radiation, 1*.

Tan, B., Woodcock, C., Hu, J., Zhang, P., Ozdogan, M., Huang, D., . . . Myneni, R. (2006). The impact of gridding artifacts on the local spatial properties of MODIS data: Implications for validation, compositing, and band-to-band registration across resolutions. *Remote Sensing of Environment, 105*(2), 98-114.

Thenkabail, P. S., Hanjra, M. A., Dheeravath, V., & Gumma, M. (2010). A holistic view of global croplands and their water use for ensuring global food security in the 21st century through advanced remote sensing and non-remote sensing approaches. *Remote Sensing, 2*(1), 211-261.

Torrey, V. (1948). The World's Biggest Working Model. *Popular Science*, 115 - 120.

Tucker, C., & Sellers, P. (1986). Satellite remote sensing of primary production. *International Journal of Remote Sensing, 7*(11). doi:10.1080/01431168608948944

UNFCCC. (2004). Implementation plan for the Global Observing System for Climate in support of the UNFCCC. *United Nations.*

Vane, G., & Goetz, A. (1993). Terrestrial imaging spectrometry: Current status, future trends. *Remote Sensing of Environment, 44*(2-3), 117-126. doi:10.1016/0034-4257(93)90011-l

Walton, A. (2013). Provincial-Level projection of the current mountain pine beetle outbreak: update of the infestation projection based on the Provincial Aerial Overview Surveys of Forest Health conducted from 1999 through 2012 and the BCMPB model (Year 10). *Ministry of Forests, Lands and Natural Resource Operations*.

Wang, Q., Adiku, S., Tenhunen, J., & Granier, A. (2005). On the relationship of NDVI with leaf area index in a deciduous forest site. *Remote Sensing of Environment, 94*(2), 244-255. doi:10.1016/j.rse.2004.10.006

Wanner, W., Strahler, A. H., Hu, B., Lewis, P., Muller, J. P., Li, X., . . . Barnsley, M. J. (1997). Global retrieval of bidirectional reflectance and albedo over land from EOS MODIS and MISR data: Theory and algorithm. *Journal of Geophysical Research: Atmospheres (1984–2012), 102*(D14), 17143-17161. doi:10.1029/96jd03295

Woodcock, C. E., & Strahler, A. H. (1987). The factor of scale in remote sensing. *Remote Sensing of Environment, 21*(3), 311-332. doi:10.1016/0034-4257(87)90015-0